Technische Universiteit Delft

Study of Hydrogen Sorption/Desorption Effect on Austenitic Iron-Based Alloys

Surface interaction studied by cyclic voltammetry on 304L stainless steel and Invar

Katherine S. Encalada Flores

TU Delft

Study of Hydrogen Sorption/Desorption Effect on Austenitic Iron-Based Alloys

Surface interaction studied by cyclic voltammetry on 304L stainless steel and Invar

by

Katherine S. Encalada Flores

to obtain the degree of Master of Science
at the Delft University of Technology,
to be defended publicly on October 28th, 2019 at 2:00 PM.

Student number: 4563840
Project duration: November 19, 2019 – October 28, 2019
Thesis committee: Dr. A. J. Böttger, TU Delft, supervisor
Dr. V. Popovich, TU Delft
Dr. R. Kortlever, TU Delft

TU Delft

Acknowledgement

I would like to thank my supervisor Dr. Amarante Böttger, for her constant support and incredible scientific guidance during this thesis project. Additionally, to Dr. Yaiza González for having provided really good insights concerning the electrochemical methods.

Special recognition to Dhr. Ruud Hendrikx at the Department of Materials Science and Engineering of the Delft University of Technology for the X-ray analysis and its availability to help.

I would like to thank MEng. Agnieszka Kooijman at the Corrosion Technology and Electrochemistry Laboratory of the Delft University of Technology for her support and collaboration to conduct the electrochemical experiments.

Next, I would like to thank my loved partner, Joel, who has to give me extraordinary emotional support, and has unconditionally been there for me to cheer me up with just the right words in difficult moments.

I would like to thank my family: Manuel, Mariana and Santiago, for their unconditional love and support since the beginning of this process. To my mom who infallibly has sent me a text message, full of love and support, every morning since I moved into the Netherlands. To my father who had always believed even when I doubted myself and to my brother who has always been there for helping me despite the distance.

I also want to thank my schoolmates and friends: Katja, Sandra and Irving for having made the journey at grad school experience full of good moments. Especially to Katja, for having been more than my study partner, a true friend.

I want to thank my Mexican-Ecuadorian group of friends: Celia, Alessandra, Daniel, Arturo, Jorge, and Gina for having made me feel closer to home. Especially to Celia and Alessandra for the good talk, food, and complicity.

This project would have been impossible without the collaboration agreement between Gaztransport & Technigaz (GTT) company and the Delft University of Technology.

Finally, I would like to thanks to the Government of Ecuador (institutionally represented by SENESCYT) for having granted me a full scholarship to cover my studies at the Delft University of Technology.

Katherine S. Encalada Flores
Delft, October 2019

Abstract

The so-called “hydrogen economy” became one of the scientific targets among the different renewable energies alternatives, as a result of the efforts to transition from fossil fuels to environmentally-friendly energy sources. In this context, various options to transport and store hydrogen are being explored. Gaztransport & Technigaz (GTT) company, intending to be part of this challenge, is exploring the possibility to transport liquid hydrogen (LH2) in pre-existent ship’s containers initially designed for liquid natural gas (LNG) transportation. This project is about the study of the surface effect of the interaction between hydrogen with iron-based alloys in the case of 304L stainless steel (uncoated and coated with TiO_2) and Invar alloy.

The methodology consisted of electrochemical induced hydrogen evolution on an iron-based austenitic metal cathode taking advantage of the intermediate adsorbates (atomic hydrogen) generated during the reaction to study the electrochemical adsorption efficiency. Characterisation of the materials, by techniques like XRF, XRD, optical microscopy, and SEM, is conducted before and after hydrogen exposure so that it was possible to evaluate the effect of hydrogen ingress.

The results showed that the chemistry of the surfaces is irreversible changed after the electrochemical induced hydrogen sorption/desorption process due to the formation of oxides. The amounts of hydrogen desorbed were quantified after different H_2 loading times. In all cases, the amount of hydrogen desorbed showed a maximum after which the hydrogen desorbed decreased significantly. The maximum for uncoated 304L stainless steel was after 24 h, 90 min for the coated 304L, and 2 h for Invar. The welds are the most vulnerable sections to hydrogen ingress in both cases. XRD results before hydrogen exposure revealed that 304L consists of an austenitic matrix with around 5% of ferrite. An increment of the austenitic volume fraction of 2.2% was observed after the H2 sorption/desorption process. Invar is a purely austenitic phase, and no changes in the phase composition were observed after the H_2 sorption/desorption process.

Contents

List of Reactions

List of Figures

List of Tables

1

Introduction

The environment deterioration and climate change, resulting from the dependency of fossil fuels as a primary source of energy, has placed the energy industry into the spotlight. As a result, a transition towards more sustainable energy is required. In this context, hydrogen has been targeted as an energy carrier able to contribute to the reduction of CO_2 emissions during energy production [3]. Hydrogen catches attention due to its high energy density per unit of mass 120(MJ/kg) which is higher than some other green energy options like solar or wind energy [52].

Because hydrogen cannot be found in nature, it has to be extracted from other primary sources. Consequently, several ways of storage and transport are being studied and subjected to improvement. A classification of the different types of hydrogen storage is shown in figure 1.1 by Klebanoff (2013) [2].

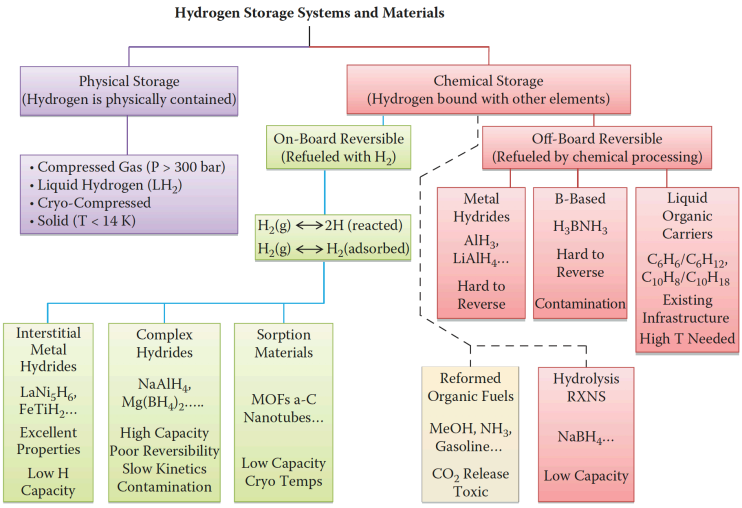

Figure 1.1: Overview of hydrogen storage systems and materials [2]

The last few years have led to necessary scientific research correlated with the chemical methods for hydrogen storage. They are mainly focused on metal hydrides and liquid organic carriers due to the high gravimetric storage capacity they offer, around 70 gH_2/L as lowest [52]. In addition, metal hydrides allow longer discharge time and offer safety due to the moderate temperature and pressure conditions of solid transportation[30].

In spite of the significant advantages of the chemical storage options, there are several applications in which physical storage is preferred. For example, liquid hydrogen storage is preferred on aerospace applications where a most instantaneous release of energy is required or in hydrogen vehicles where the storage weight must be minimised [7, 42]. Among the physical ways of hydrogen storage, the liquid

form is the one offering the higher gravimetric storage capacity, as shown in figure 1.2. However, the hydrogen energy density per unit of volume is rather low in comparison with other fuels [41].

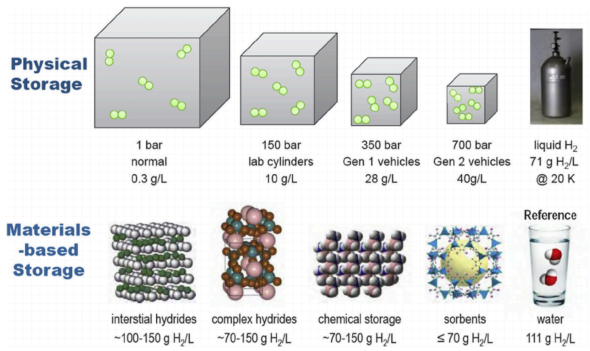

Figure 1.2: Gravimetric storage capacity of different hydrogen storage systems [52]

Physical storage/transportation of liquid hydrogen suggests taking a close look at the materials of which the containers are made of, the thermodynamic conditions of storage, the surface interactions happening inside the tanks, the insulation systems, etc. Among all of these aspects, from the Materials Science perspective, it results interesting to understand the interaction occurring between the substance inside the tank (liquid or gas hydrogen) and the material that is containing it. So that it is possible to identify possible mechanical, structural or chemical effects resulting from this surface interaction.

Such specific demands on the container explain why only a few materials are suitable to perform as liquid hydrogen vessels. Specifically referring to metals, aluminium alloys, iron-nickel alloys, and austenitic steels has been reported to be the ones that perform the best in hydrogen environtment [7, 46]. Nonetheless, the performance of these metals can be compromised as a result of a hydrogen-induced phase transformation, a change on the corrosion behaviour, or a deterioration of mechanical properties like in the case of hydrogen embrittlement. Consequently, the study of the effect of the hydrogen-metal interaction over the material's properties and behaviour is essential in hydrogen storage and transport applications.

1.0.1. Objective and Research Questions

The present project aims to study the surface effect of the interaction between hydrogen with iron-based alloys for the application of cargo transport of liquid hydrogen (LH2) in pre-existent ship's containers initially designed for liquid natural gas (LNG) transportation. This goal can be achieved by answering the following research questions:

1. How is it attainable to experimentally simulate the interaction hydrogen-metal happening inside a cargo ship at laboratory scale by electrochemical methods?

2. Is it possible to measure and quantify adsorbed hydrogen on an iron-based metal alloy surface through electrochemical methods?

3. What effects caused by the hydrogen sorption/desorption process can be observed over the microstructure and surface state in the particular case of 304L stainless steel and Invar alloy?

The previously stated questions are going to be answered by establishing the experimental settings of the electrochemical techniques used to generate the conditions for a hydrogen-metal interaction to occur. Later, a quantification procedure to evaluate the amount of hydrogen up-taken will be conducted. Finally, through analytical techniques (XRD and microscopy), the microstructural and the surface effect over the metals subjected to study will be analysed.

1.0.2. Outline of the document

Chapter 2
Basic considerations about hydrogen and its storage, an overview in austenitic steels, interaction of hydrogen with a metallic surface and the electrochemical pathway for studying hydrogen adsorption/desorption are reviewed.

Chapter 3
Description of the experimental and analytical methods involved in both the hydrogen generation and the evaluation of hydrogen effect on a metal surface.

Chapter 4
The experimental results obtained from the electrochemical experiments as well as the results from the characterisation techniques are shown and discussed.

Chapter 5
The conclusions and answers to the research questions are presented.

Chapter 6
Future perspectives for the present study are presented, as well as potential complementary experimental analyses that can be conducted, are described in this chapter.

2

Literature Review

This chapter provides an overview of the surface interaction between hydrogen and a metal. It starts with the basics of hydrogen and liquid hydrogen storage and transport. Then, it presents an overview of the materials of interest in this work, resulting from the most promising technologies from GTT. Then, the interaction between hydrogen and metal surfaces is explained. Next, the effect of hydrogen on iron-based alloys is explored. Finally, the electrochemical pathway for studying hydrogen interaction at a laboratory scale is discussed.

2.1. Basics of Hydrogen

Hydrogen at room temperature and atmospheric pressure is found in a gas form consisting of diatomic molecules covalently bonded. Whereas liquid hydrogen (LH2) requires very low temperatures, around -253°C (20 K), to exist at atmospheric pressure.

Generally speaking, the hydrogen atom consists of one proton with one electron orbiting around it. From particle physics, it is known that, as a fundamental property, each electron has its own spin. During covalent bonding, the electrons involved can be lined up either in the same spin direction or the opposite. This variability leads to the origin of two isomers, ortho-hydrogen when their spins are aligned in the same direction and para-hydrogen when aligned in the opposite direction [9].

The amount of energy available in the system determines the ratio of the two isomers. It has been reported that at (-193°C) the isomers' ratio is fifty-fifty. However, when raising the temperature up to room temperature, the so-called "normal hydrogen gas" stabilises at a 3:1 ortho:para hydrogen ratio. A higher temperature implies higher thermal energy for the molecules to reach a higher energy state, in this case, the orthohydrogen form. Thermodynamically speaking, the para-to-ortho hydrogen conversion is an endothermic process whereas the ortho-to-para is exothermic [34]. The enthalpy of conversion from normal to equilibrium hydrogen at -253°C is approximately 532 kJ/kg which is almost comparable with the enthalpy of vaporisation, 447 kJ/kg, at the same temperature [68].

2.1.1. Liquid Hydrogen Storage and Transport

When working with liquefied hydrogen some technical aspects like for example, the isomers composition of the LH2, the materials used to be in contact with hydrogen, the boil-off effect, etc. become very important aspects to take into account.

At cryogenic temperature, the LH2 becomes very vulnerable to boil-off [22]. The boil-off phenomenon is substantially dependant on the ortho:para hydrogen ratio in the way that, the amount of energy released due to this exothermic conversion is more than enough to vaporise the liquid in some extend, as explained in section 2.1. This is the reason why hydrogen is catalytically converted into parahydrogen during the liquefaction process [68]. Additionally, the insulation system of the tanks

must be very robust to minimise heat leakage from the surroundings.

Regarding the containers for LH2, one needs to be aware that not all the materials exhibit good performance at cryogenic temperatures. The hydrogen molecule is a very small molecule that can easily diffuse into the material that is in contact with causing changes in its microstructure as later explained in section 2.4.2. As a consequence, only a few materials are suitable to perform as LH2 containers. Aluminium alloys, iron-nickel alloys, and austenitic steels have been reported as the metallic materials that best perform in such conditions [7, 46]. Titanium alloys are also under study whereas fibre-reinforced plastic (FRP) is used when lightweight solutions are required [22].

2.2. Cargo Ships' Technologies of Gaztransport & Technigaz Company

Gaztransport & Technigaz is a leader company in offering shipping and storage solutions in cryogenic conditions of LNG (liquefied natural gas). As a pioneer company, GTT is continuously researching and developing new LNG containment technologies. Following the same spirit and looking forward to meeting the future requirements of both the industry and society, GTT is working on expanding its solutions for liquid hydrogen. It is at this point in which the present project takes form. Hydrogen transportation and storage is a crucial step towards the "hydrogen economy" for which GTT is willing to provide cargo shipping solutions.

Previous studies [28, 46, 47], have provided extensive information about the mechanical effects of cryogenic hydrogen storage on GTT ship's inner hull material. Therefore, this project aims to contribute to complete the panorama by providing some understanding of the interaction taking place between hydrogen and the metal surface. All of these insights together in combination with the corresponding studies in insulation systems, mechanical behaviour, etc. contribute to the future transitioning into the hydrogen economy.

As reviewed in section 2.1.1, austenitic steels, and iron-nickel alloys have been target as good candidates for LH2 storage. Currently, two of GTT 's technologies appear to be suitable for LH2 applications. Mark III technologies whose primary membrane is made of corrugated stainless steel 304L, 1.2 mm thick and NO96 technologies whose primary and secondary membranes are made of Invar®, a (36%) nickel-(64%) iron alloy, 0.7 mm thick [64]. Figures 2.1 and 2.2 show the inside of the GTT Mark III and NO96 tanks, correspondingly.

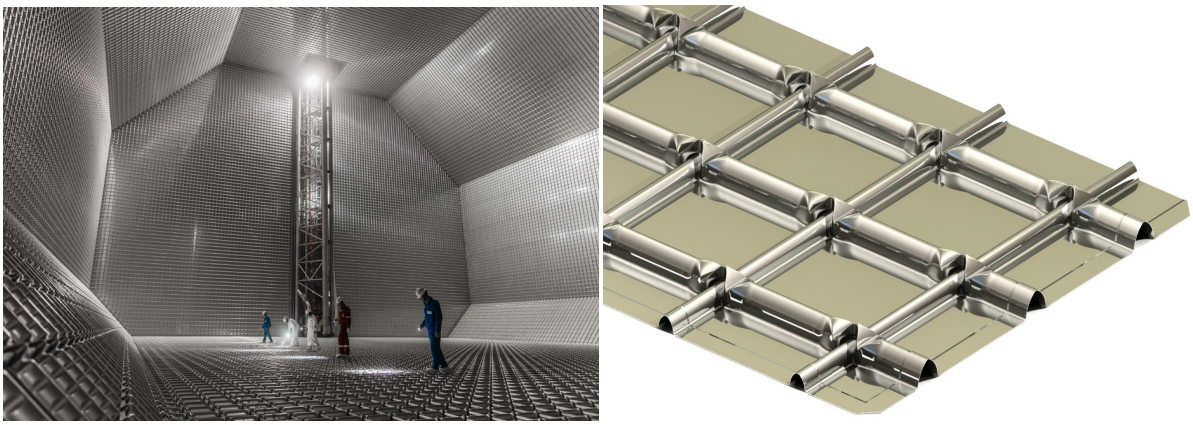

(a) Inner hull **(b)** 304L stainless steel corrugated membrane

Figure 2.1: The inside looking of the GTT Mark III tank [64]

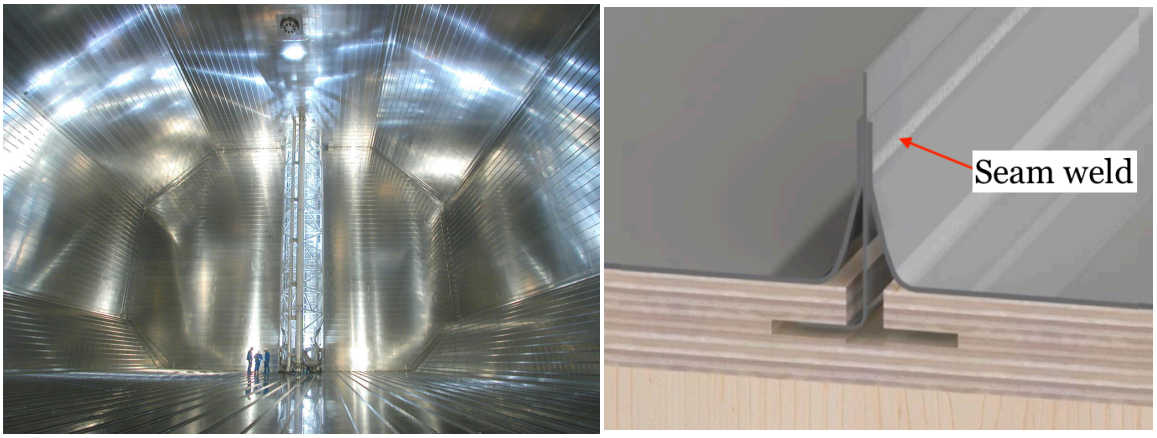

(a) Inner hull **(b)** Invar® flat wall area

Figure 2.2: The inside looking of the NO96 tank [64]

2.2.1. 304L stainless steel

The 304 steel series corresponds to a non-magnetic metastable[1] austenitic stainless steel, containing as main alloying elements Ni (between 8% to 12% wt.) and Cr which have been targeted as austenitic phase stabilisers [56]. The austenitic phase (γ-Fe) presents a face-centered cubic crystal structure.

The denomination of 304L refers to is an extra-low carbon version of the 304 steel (maximum carbon content of 0.03% wt.). Due to its low content of carbon the carbide precipitation (sensitisation) happening at an abrupt increase of temperature, like during welding, is significantly reduced. Consequently, the 304L type is widely used as material for vessels and pipes due to its high corrosion resistance and outstanding performance during welding and machining [37].

Even though 304 stainless steel contains a significant amount of chromium (minimum 18% wt.) which gives the steel excellent chemical protection against harsh environments. Some coatings like for example TiO_2, SiO_2, and Al_2O_3 are commonly used to increase protection against aggressive environments. Explicitly, titanium dioxide has been reported to possess a good passivation layer which is very desirable for corrosion protection. Also, TiO_2 can improve the tribological properties of the coated material [45].

2.2.2. Invar®

Invar alloy is a 36% Ni 64% iron alloy characterised for having a very low coefficient of thermal expansion in a wide range of temperature which make it suitable for cryogenic applications. Invar exhibits a single stable ferromagnetic austenitic phase (γ-Fe,Ni). Figure 2.3 shows a schematic of Invar FCC crystal structure.

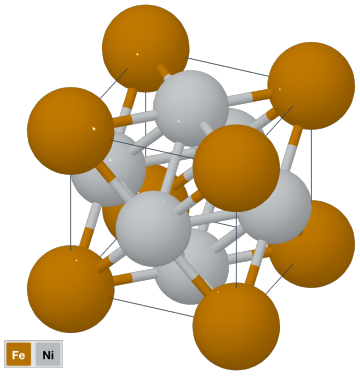

Figure 2.3: Crystal structure of $FeNi_3$ corresponding to Invar [26, 69]

2.3. Interaction of hydrogen with metallic surfaces

Hydrogen can get in contact with metallic surfaces either as gas, liquid, or ion form (in aqueous solution), depending on the specific exposing environment. The relevance of this interaction is related to

[1] In relation to $\gamma \rightarrow \alpha$' phase transformation

the possible degradation of the material's properties (mechanical or chemical) that it can cause.

If there is enough energy present, the interaction between hydrogen gas and a metal surface, occurs as follows [50]:

1. Transport of H_2 molecules to the metal surface
2. Molecular adsorption through Van der Waals forces (physisorption)
3. Dissociation of H_2 molecules into atoms and chemical bonding[2] with the metal (chemisorption) on active sites[3]
4. Surface-bulk transfer: adsorbed atomic hydrogen located at the surface penetrates becoming dissolved atomic hydrogen (absorption)
5. Diffusion into the bulk

The dissociative chemisorption (step 3) will only happen if the H_2 molecule has enough energy to overcome the energetic barrier of dissociation. Otherwise, the hydrogen molecule can either stay adsorbed in its molecular form or be scattered back [72], as shown in figure 2.4. At low temperatures, the occurrence of dissociative chemisorption is less. Besides the energetic barriers, the reactivity of the metal surface plays a significant role, and it can be measured by the sticking coefficient [1].

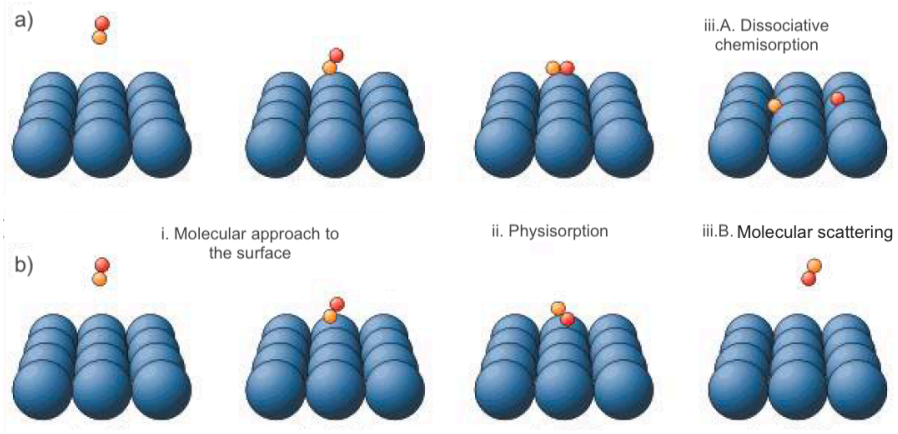

Figure 2.4: Schematic diagram of a) dissociative chemisorption process, and b) scattering process of a diatomic molecule on a metal surface, adapted from [32].

On the other hand, when hydrogen comes from an electrolyte or solution as the source, the previously described steps 1 and 2 do not exist as such; instead, two situations can occur:

(a) Chemical dissociation H_2 dissolved in solution

(b) Electrochemical dissociation from solvated (hydrated) protons or water molecules (splitting)

Figure 2.5a schematically represents the different possible species of hydrogen. For example, as a molecule in gas or liquid states, or in any other dissociated form like hydride or ion when coming from solution.

Once the hydrogen is in its atomic form, it bonds with the metal surface (schematic representation of chemisorption on figure 2.5b), and steps 4 and 5 follow as before. The efficiency of chemisorption is dictated by the catalyst activity of the surface and the character of the oxide layer present [21].

[2]The H-M bond is essentially covalent in character [1]
[3]H_2 dissociative adsorption is nonactivated on most transition metals[50]

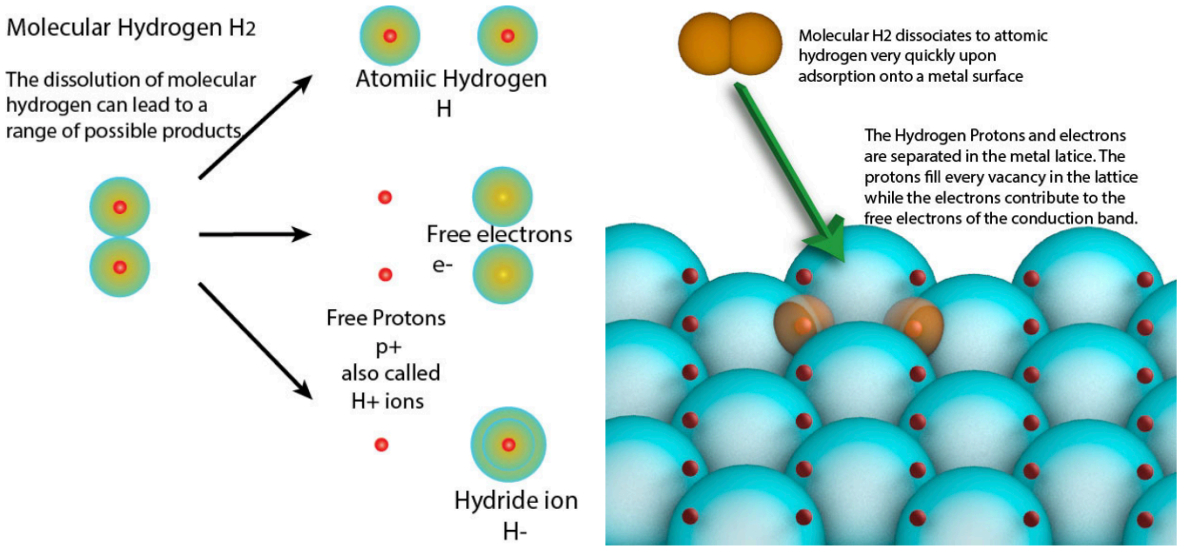

(a) Hydrogen chemical species **(b)** Chemisorption

Figure 2.5: Schematic diagram of hydrogen dissociative adsorption on a metal surface [29]

Figure 2.6 shows a schematic representation of the potential energy vs. distance (from the surface to the metal bulk) during the different sorption steps. The schematic presents to possibilities of bonding during adsorption (physisorption or chemisorption), later the sub-surface layer occurs and at last, the diffusion through the bulk. It is essential to point out that this model does not take into account any oxide layer on the metal. In the case of austenitic steels, the passivation layer constitutes another step in the absorption process. If the oxide layer is present, it affects the solubility of hydrogen in the passivated metal in terms of how fast the hydrogen gets in the metal. However, it does not change the diffusion through the metal lattice itself [21].

2.3.1. Adsorption/Desorption

It is the case for many metals that when they are exposed to $H_{2(g)}$ the hydrogen molecules experience physisorption, dissociation and later chemisorption if there are catalytic sites available. The representation of such a process is shown in equation 2.1. The efficiency of this process is closely related to the availability of the metal surface active sites as well as the presence of an oxide layer on top of the metal [21]. Hydrogen adsorption, at low pressure, occurs preferably at highly coordinated sites, hollows, or bridge sites in a metal [50].

$$H_{2(g)} \rightarrow H_{(ads)} + H_{(ads)} \tag{2.1}$$

The rates of adsorption and desorption are not necessarily the same. This situation occurs because the metal surface is modified (adsorbate-induced reconstructions) by the sorption of dissociative hydrogen atoms. Therefore, for desorption to occur, a local rearrangement of the surface is needed to release the hydrogen atoms previously taken up which slows downs the process [1].

The adsorption process can also be influenced by the presence of a second adsorbate, like oxygen, that can lower the sticking coefficient, which often happens in polycrystalline and stepped surfaces [1].

2.3.2. Diffusivity and Solubility

Diffusion consists of the process of atomic hydrogen moving trough interstitial sites of a crystal structure following a minimum energy path after having overcome the initial energy barrier (or activation energy for diffusion) to move from one layer to the subsequent sublayer [12].

In the case of corrosion-resistance alloys, a passivation layer (consisting of an oxide layer) adds another step in the diffusion path implying that passive layer can act as a slow-down agent in hydrogen

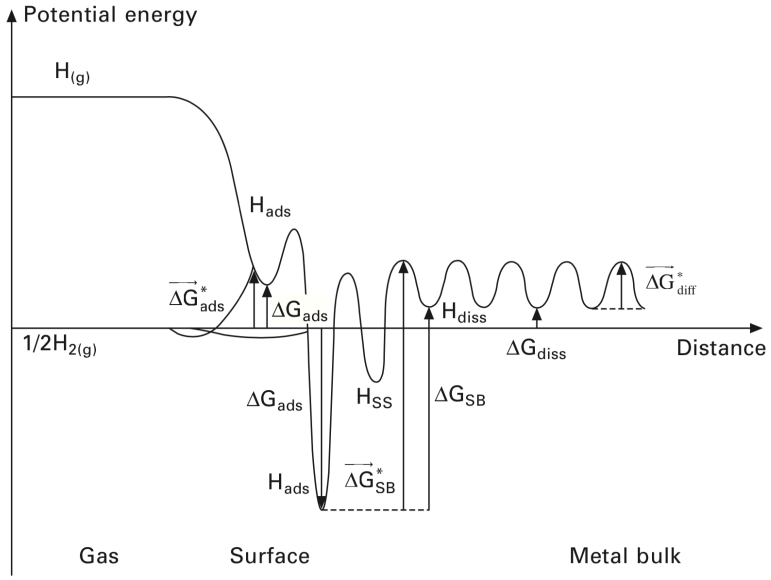

Figure 2.6: Schematic diagram of the potential energy vs. distance curves for the various H states at the gas-metal interface. Two adsorption states (H_{ads}): weakly bonded sites (physisorbed) and strongly bonded sites (chemisorbed), the sub-surface state (H_{ss}) and the bulk dissolved (absorbed) state (H_{diss}), [21]

.

uptake [21].

Concerning the lattice steel structure, the atomic hydrogen allocates in a specific type of interstitial depending on the crystallographic phase. In the case of ferrite (BCC) and martensite (BCT), tetrahedral interstitials have been reported as more favourable interstitial sites than octahedral ones. Nonetheless, the temperature has an influence over the interstitial occupancy. At low temperatures, tetrahedral interstitials are always preferred, but as the temperature rises the occupancy of octahedral sites increases due to entropic factors [21, 43]. Whereas octahedral sites are preferred over tetragonal in the austenitic phase (FCC).

The diffusion migration path of H atoms in BCC crystal structures is direct, meaning from one tetrahedral site to another. However, for the FCC crystal structure, the closed-packed atoms rows prevent hydrogen from taking direct jumps resulting in motion with intermediate jumps. Therefore, to jump from one octahedral site to another, the H atoms have to do an intermediate jump in a tetrahedral site in between. Also, the nearest-neighbour distances between tetrahedral sites are smaller in BCC than in FCC, which implies lower activation energy for diffusion in BCC structures. In addition, the sublayer also plays a tremendous role in the diffusion process because sometimes the nearest subsurface sites distances are shorter than the nearest neighbour distances in the bulk [50].

Now, it is easy to understand that the hydrogen diffusion coefficient is closely related to the crystal structure. At atmospheric temperature, this coefficient's magnitude is 4 to 5 times higher in body centered cubic (BCC) structures than in the face-centered cubic (FCC) for most pure metals. For example, the hydrogen lattice diffusivity in a BCC structure is in the order of 10^{-3} $cm^2 \cdot s^{-1}$ whereas for a FCC structure is about 10^{-12} $cm^2 \cdot s^{-1}$ [55]. Additionally, the temperature plays a detrimental role in dictating that the hydrogen diffusion rate increases as the temperature does. The reason is that high temperature implies more energy for the hydrogen atoms to be released from deep traps and diffuse [39].

On the other hand, solubility is related to the hydrogen concentration in the crystal structure at a specific temperature. When referring to solid iron the solubility is higher in the austenitic phase than in ferrite, bainite or martensite phases [21]. Nonetheless, generally speaking, the hydrogen solubility is very low in steel (only in the order of ppm at normal conditions) [6].

Since the lattice structure is not perfect, the study becomes more complicated due to a large number of possibilities for trapping that the microstructure of a material can have (figure 2.7). In the specific case of steel, the average hydrogen content is of the order of 10^{-1} to 100 ppm (mass) [31].

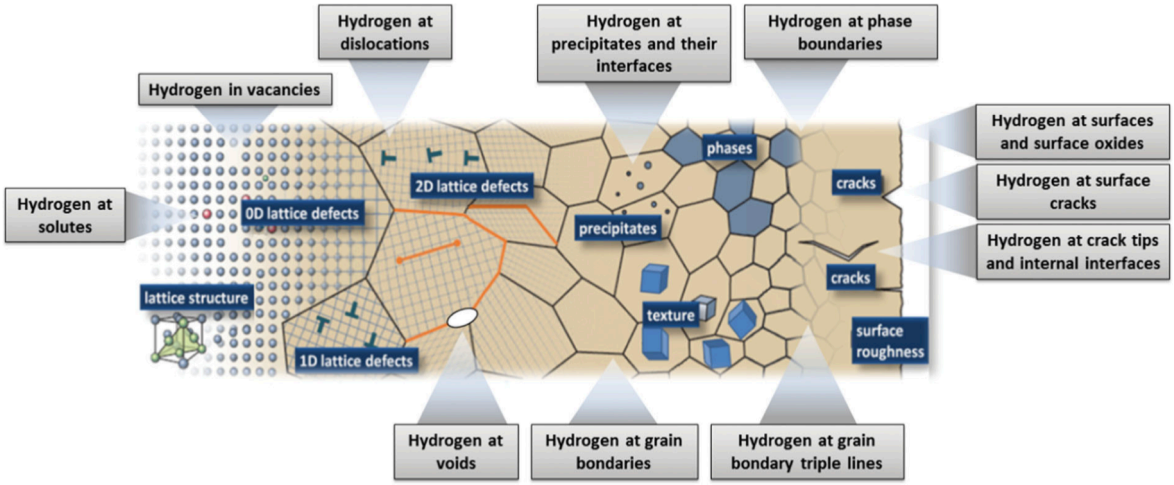

Figure 2.7: Schematic of possible hydrogen traps in the micro-structural architecture of a metal [31]

.

2.4. Effect of hydrogen on iron-based austenitic alloys

Hydrogen can have an effect over the austenitic iron phase in different aspects such as mechanical properties, microstructure or corrosion behaviour.

2.4.1. Hydrogen embrittlement (HE)

Hydrogen absorption into metal has been pointed out as a precursor for material embrittlement constituting one of the most detrimental mechanical effects of hydrogen-metal interaction [24]. However, for absorption to occur, early stages need to happen, adsorption, and subsequently, bulk diffusion. These initial stages present their energy barriers, as previously explained in figure 2.6. If the energy barriers are overcome, hydrogen will be moving in-between interstitial sites of the metal structure through the minimum energy path. In addition, a certain value of hydrogen content needs to be reached to lead to embrittlement depending on the chemical composition of each steel [77].

Two HE mechanisms are most commonly to occur in austenitic steels, hydrogen-enhanced local plasticity (HELP) and adsorption-induced decohesion mechanism (AIDE) [37]. HELP mechanism proposes that hydrogen facilitates the movement of dislocations by decreasing the repulsive forces between them. The enhancement of plasticity is the result of the reduction of the critical stress for dislocation movement. On the other hand, AIDE proposes that the hydrogen-assisted cracking results from the adsorption of hydrogen at the crack tip that weakens the interatomic bonds at different atomic distances resulting in the emission of dislocations from the crack tip. After the nucleation, the dislocations can move from the crack tip, if stress is applied, generating the growth of the crack [6].

Prestrain-induced martensite as a pathway for HE

It is well known that pre-strain on metastable austenitic steels can induce a phase transformation from austenite (γ-Fe) to martensite (α'-Fe) in a vast range of temperatures [70]. This transformation consists of a crystallographic evolution from FCC as a parenting phase to a BCC as a resulting phase which most likely occurs at twins, shear bands or via ε-martensite [13]. Being the last one associated with staking faults acting as martensitic nucleations cites in the parenting phase [74].

Induced strain over the material is very well expected to happen during the shaping process of a metal piece, as it is the case of the shaping of corrugated sections of Mark III technology in GTT ships [28]. Sidhoum et al. propose that the martensitic transformation is more favourable to happen in tension than in compression [59].

Induced martensite is relevant from the point of view that hydrogen diffusion is faster through martensite than through austenite phase [77], meaning that the diffusion coefficient for α'-Fe (martensite) is higher than in γ-Fe (austenite) [37]. Consequently, even a small amount of strain-induced martensite in the surroundings of a crack tip becomes a highway for hydrogen diffusion leading to embrittlement.

Nevertheless, it is also possible that hydrogen embrittlement occurs without any martensitic transformation of the austenitic phase [43, 55]. For example, as a result of the increment of dislocations which facilitates the hydrogen entry into the material but they have a lower impact over hydrogen embrittlement than the martensitic phase [70].

2.4.2. Hydrogen induced phase transformation on iron-based austenitic alloys subjected to cathodic charging

Electrochemical hydrogen generation on an austenitic iron-based alloy catalyst (cathode) can induce two types of phase transformations, the first one is an induced martensitic transformation, and the second one is an iron-hydride formation [6].

Hydrogen induced martensitic formation

Rozenak [53] mentions that there is evidence of an induced martensite transformation (α'-martensite and ε-martensite) on austenitic steels (study made on ASI 321, 347, 304, 316 and 310) as a result of high fugacity[4] hydrogen formed during cathodic polarisation in electrochemical experiments. High fugacity hydrogen, in combination with the limited diffusion coefficient in the austenitic phase, results in an inhomogeneous hydrogen distribution over the material. The important hydrogen concentration gradient induces internal stresses. The internal stresses can lead to two phenomena, the formation of cracks as a mechanism of stress relaxation, or a martensite stress-induced phase transformation [53].

An older study, from Yang et al. [74], also mentions that the hydrogen-induced martensite formation phenomenon on 304 stainless steel is determined by critical hydrogen charging time and current. Enough hydrogen concentration and stress need to be built up at the surface to reach the driving force required $\gamma \rightarrow \varepsilon$-martensite formation. The authors report that no martensite is formed when the charging current density is lower than 0.2 mA·cm^{-2}.

Hydrogen induced iron-hydride formation

The hydride formation is another possible effect induced by hydrogen that consists of the lattice expansion of the austenitic phase. The iron-hydride phase ($\gamma_{Hydride}$) also has an FCC crystal structure which makes it not so easy to distinguish from the austenite matrix (γ-Fe) [6, 54].

Nishino et al.[75] studied the iron-hydride phase by XRD, reporting a broadening of the {111} and {200} reflection planes accompanied by a shifting of the 2θ angle to smaller values. Additionally, the increment of the lattice parameter (between 0.2 to 1.2%) is reported. The authors also present a correlation of the occurrence of the iron-hydride with the Ni content.

2.4.3. Corrosion effect

Another effect of hydrogen-metal interaction complies with the corrosion effect over some metals. For example, on stainless steels, it has been shown that hydrogen sorption has a negative effect on the corrosion behaviour because it can reduce the stability of their characteristic protective passive film. Even though the mechanism associated is not clear yet, it has been experimentally demonstrated that hydrogen promotes the breakdown of the passive layer on type 304 stainless steel and prevents the re-passivation process. These conditions cause the shortening of the periods for pitting corrosion [73].

[4] Comparable with a high pressure gas phase of 4x10^9 Pa

2.5. Electrochemical pathway for studying hydrogen sorption

The study of hydrogen interaction with materials during LH2 transport and storage needs to take into account not only its liquid [5] state but most detrimentally its gas phase. On the one hand, even in small quantities, it is expected that some amount of the liquid hydrogen evaporates; therefore, two phases (liquid and gas) are most likely to be present in the vessels during transportation. On the other hand, during emptying and unloading the tanks the temperature will get closer to ambient temperature resulting in even more hydrogen gas present inside the tank.

Jerkiewicz et al. made a comparison between hydrogen electro-adsorption from an electrolyte and hydrogen adsorption from a gas phase showing that despite the electrical double layer (in the case of the electrolyte) the strength of the M-H bond is not affected [27]. In addition, Enomoto et al. made the same comparative study on 316L and 304 stainless steel concluding that it is possible to predict the absorption of hydrogen under high-pressure atmosphere at elevated temperatures from the hydrogen electroadsorption method (cathodic charging) if the surface concentration of hydrogen or the effective hydrogen fugacity at the specimen surface is known. The authors also mentioned that the observations of the mechanical degradation of the tensile properties are similar under both testing conditions [18]. On the contrary, Hoelzel et al. report that cathodic hydrogen charging lead to higher local stresses due to strong gradients in the hydrogen concentration than high-pressure hydrogenation [25]. Nonetheless, the literature comparing gas environment with aqueous solutions for studying hydrogen adsorption is still very limited.

In this framework, the electrochemical pathway becomes a powerful tool to induce a hydrogen-metal interaction on a laboratory scale and evaluate the response of the metal under study. Although the electrochemically induced hydrogen interaction is not exactly the same as in reality, where dissociative chemisorption is less likely to occur due to low working temperature and atmospheric pressure, the experiment still allows getting a good understanding of the nature of hydrogen-metal interaction. This study is fundamental from the perspective of engineering design in which the worst-case scenario must be evaluated in this specific case, the occurrence of dissociative chemisorption.

2.5.1. Hydrogen Evolution Reaction

One easy and cheap way to produce hydrogen is by water electrolysis. This process consists of breaking down water into hydrogen and oxygen by passing an electric current through it [14]. The correspondent net reaction (reaction 1) emerges from the cathodic hydrogen evolution (reaction 2) and the anodic oxygen evolution (reaction 3) half-cell reactions in alkaline medium [33]. The standard cell voltage for the net reaction, independently from the pH, is 1.23 V which is equivalent to ΔG of 237.2 kJ/mol at 25°C [14].

$$2\,H_2O_{(l)} \rightleftharpoons 2\,H_{2(g)} + O_{2(g)} \quad \{1\}$$

$$2\,H_2O_{(l)} + 2\,e^- \rightleftharpoons 2\,OH^- + H_{2(g)} \quad \{2\}$$

$$H_2O_{(l)} - 2\,e^- \rightleftharpoons \frac{1}{2}\,O_{2(g)} + 2\,H^+ \quad \{3\}$$

Usually, catalysts are used to accelerate the kinetics of the HER when the goal is to produce hydrogen gas, as for example platinum group metals (PGM), Ni-based catalysts, CoP, WC, TiO_2 and $CoSe_2$ [23, 63]. In this context, a lot of efforts have been made to fully understand how the catalyst electrode influences the kinetics of the HER. However, the present study does not intend to study the influence of the electrode material (cathode) on HER but vice-versa, meaning, how hydrogen sorption[6] impacts over the material at the microstructural scale. The alkaline medium has been reported to provide more stability for the catalyst (no corrosion or dissolution of the electrode) therefore it is preferred at industrial scale [40, 63]. Whereas, the acidic based medium is known for the vaporisation of the acidic electrolyte

[5] Liquid hydrogen in contact with a metal surface might undergo physisorption; however, this type of adsorption involves only relative weak forces and it is reversible by raising the temperature (desorption)

[6] Sorption is the most general term to refer to the uptake of a substance into another and involves both processes adsorption and absorption

which corrodes the electrolytic cell (affecting the stability of the electrodes) and contaminates the produced hydrogen gas [40]. The HER conducted on alkaline media has slow kinetics[7], 2-3 times slower than in acidic environment, which has led to propose innovative catalysts like hetero-structured materials to improve the catalytic activity [71].

Even though the hydrogen evolution reaction mechanism strongly depends on the catalyst surface, generally speaking two parallel reaction routs are most likely to occur in alkaline environment [23]. One route is the Volmer →Heyrovsky (reactions 4→5) whereas the other is the Volmer →Tafel (reactions 4→6) route [10, 33, 40].

(i) Volmer reaction: electrochemical hydrogen adsorption

$$H_2O_{(l)} + e^- \longrightarrow H_{(ads)} + OH^- \quad \{4\}$$

(ii) Heyrovsky reaction: electrochemical hydrogen desorption

$$H_2O_{(l)} + e^- + H_{(ads)} \longrightarrow H_{2(g)} + OH^- \quad \{5\}$$

(iii) Tafel reaction: chemical hydrogen desorption

$$H_{(ads)} + H_{(ads)} \longrightarrow H_{2(g)} \quad \{6\}$$

Where the $H_{(ads)}$ refers to the hydrogen atom adsorbed (adatom) on the metal surface acting as the working electrode. From the above reactions, only the Tafel reaction is independent of the pH because there is no charge transfer involved [10]. Consequently, only the Volmer-Heyrovsky mechanism can be studied by electrochemical techniques. The steady-state for the HER is met when the net rate of the electroadsorption is double the net rate corresponding to the H_2(g) formation [50]. A schematic representation of the reaction mechanism in the alkaline environment is presented in figure 2.8.

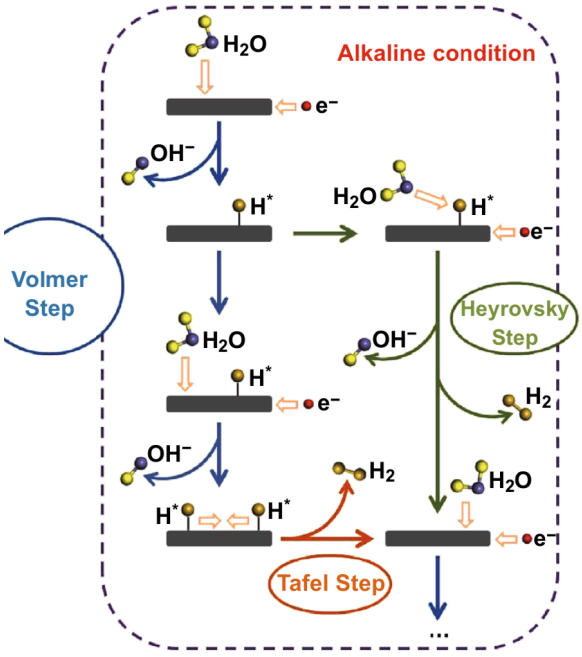

Figure 2.8: Schematic pathways for hydrogen evolution reaction under alkaline conditions [71]. H^* is equivalent to $H_{(ads)}$.

In addition to the different routes regarding the reaction mechanism, it is also possible that the adsorbed atom reaches equilibrium with the metal lattice allowing the $H_{(ads)}$ to penetrate from the outermost atomic layer of the metal towards the next sublayer and so on in a process called absorption.

[7] The reaction rates (kinetics) associated to HER influences over the saturation time of the catalyst when cathodically charging metals with hydrogen

This mechanism could be represented by equation 2.2. The absorption mechanism and the HER reaction occur simultaneously so that they are competing processes [27].

$$H_{(ads)} \rightarrow H_{(abs)} \tag{2.2}$$

Where the $H_{(abs)}$ refers to the hydrogen atom absorbed into the bulk material. The amount of absorbed hydrogen depends on the recombination of hydrogen atoms. So, if absorption needs to be promoted, the hydrogen gas formation needs to be slowed down. This is possible to achieve by adding, to the electrolyte, a so-called “recombination poison”. Substances containing elements from groups VA and VIA of the periodic table might perform as recombination poisons [8].

2.5.2. Influence of working electrode on HER

The chemical structure of the catalyst (an iron-based metal alloy in this study) directly influences the kinetics of the HER [33]. This dependence has to deal in some extend with the Sabatier’s principle which states that the “interaction” between the catalyst and the substrate has to be just the required, neither too strong nor too weak so that the catalysis process is the optimum [51].

Explicitly referring to the HER, the intermediate species (adsorbed hydrogen atoms) involved in either of the possible two-step reaction mechanisms (section 2.5.1) limit the overall reaction rate. Parsons [48] determined that the nature of the interaction for the HER depends on the Gibbs energy of adsorption (ΔG_{ads}). If this adsorption energy has a very high positive value, then the adsorption is very poor. In contrast, if the value is too low, then the desorption becomes very slow (the products can not be easily released). As long as the ΔG_{ads} has a low value, the adsorption increases until it reaches a maximum after which it will decay again. This behaviour leads to a volcano shape, which was plotted by Trasatti back in 1972 [65]. Due to the technical limitations to measure the hydrogen adsorption and that time, the H-metal bond energy was plotted instead (figure 2.9).

However, recent studies have pointed out that this representation is no longer fully accepted. On the one hand, variabilities have been found between different studies on the ascending part (left) and most importantly the descending part does not have anything to do with the metals mentioned in it but with the oxide film form on top of them during the HER [14].

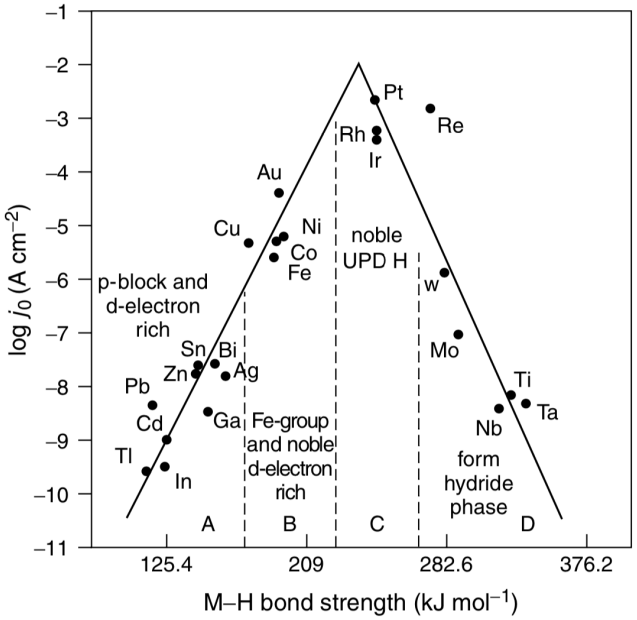

Figure 2.9: Experimental volcano plot of the standard exchange current density, log j_0, versus M–H bond energy on different metals [33]

2.5.3. Cyclic voltammetry (CV)

Cyclic voltammetry is an electrochemical technique that consists of applying a certain potential (input) to an electrolytic cell and recording the current (output) as a response. Figure 2.10 presents a schematic of this dynamic. The potential imposed allows to carry out desired reactions that do not occur spontaneously using electrical energy as source [5].

This electrochemical technique is applied very often to characterise passive films because it allows rapid identification of the peak potentials associated with redox reactions. Nonetheless, CV is susceptible to certain parameters as the scan rate and the number of cycles [20].

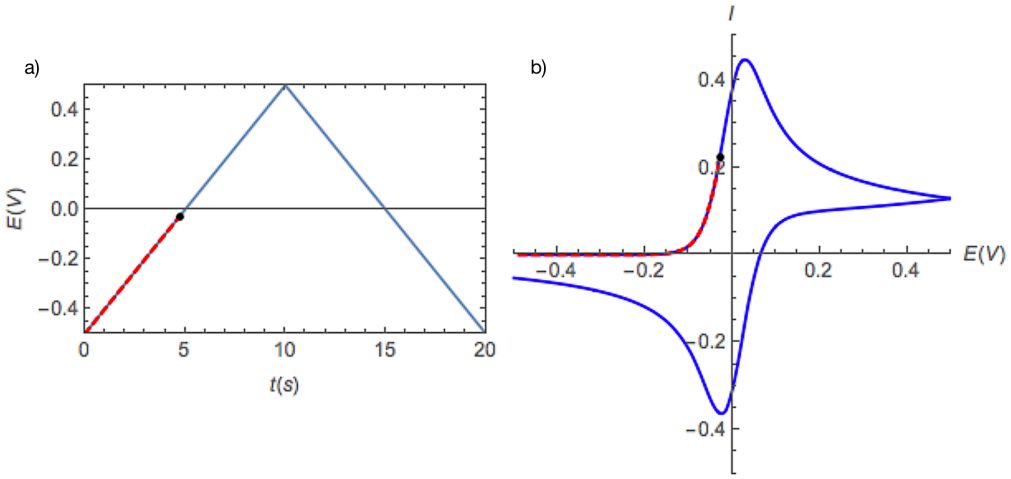

Figure 2.10: Representation of signals recorded during a cyclic voltammetry method: a) E vs. t (input) and b) I vs. E (output) [66]

A typical cyclic voltammogram for a reversible ideal system[8] is shown in figure 2.11. Where E_{pa} and E_{pc} correspond to the peak potentials whereas i_{pa} and i_{pa} are the currents associated to the peaks displayed on the anodic and cathodic branches, correspondingly. Additionally, figure 2.12 shows a comparison of cyclic voltammetric wave-shapes for different types of systems: reversible, quasi-reversible, and irreversible.

A three-electrode cell configuration is typical for conducting CV experiments. Figure 2.13 shows the setup of the electrolytic cell for the case of the HER in alkaline conditions where the following components are distinguished [36],

[8] Reversible systems exhibit a so-called “duck-shape”[17]

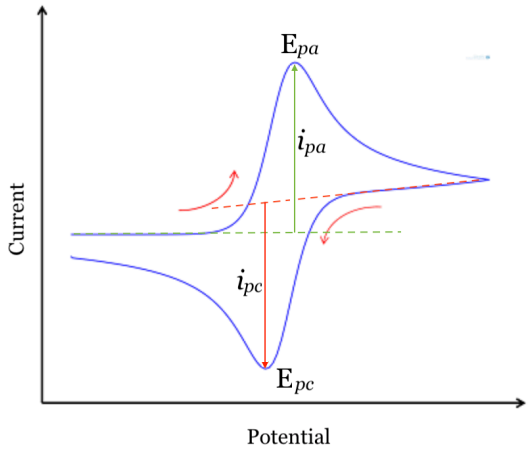

Figure 2.11: Basic components that characterise a cyclic voltammogram

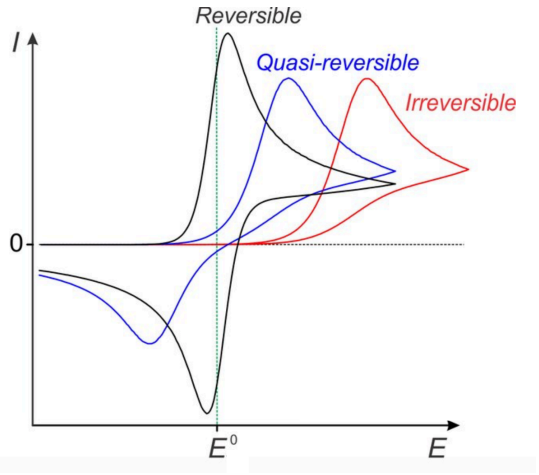

Figure 2.12: Comparison of the different wave shapes of cyclic voltammograms for different electron transfer processes,[35]

- Working electrode (WE) corresponding to the metal under study (the catalyst) that is cathodically polarised so that HER takes place on. The area exposed to the electrolyte is very well defined.
- Reference electrode (RE) is a stable reference point against which the potentials of other electrodes are measured. The stability of the RE might be affected due to contamination of the filling solution as well as the electrolyte can also get contaminated if there is leakage of ions from the electrode through the frit. This is the reason why the best is matching the filling solution of the RE with the electrolyte of the cell. If such contamination is unavoidable it is advisable to change the filling solution periodically [61]
- Counter electrode (CE) is a non-reactive material (usually platinum) that completes the circuit allowing the electrons to flow. The surface area of the CE should always be larger than the exposed area of the WE.

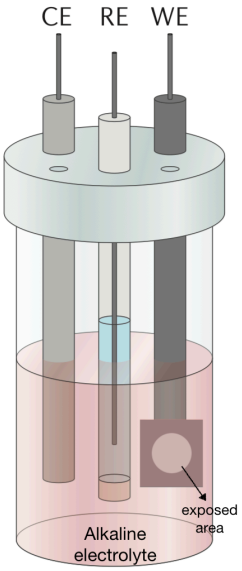

Figure 2.13: Schematic three-electrode electrolytical cell for hydrogen evolution reaction under alkaline conditions (adapted from [36])

Influence of Electrical Double Layer (EDL)

When talking about electron transfer reactions, it is important to refer to the so-called “electrical double layer”. This layer occurs in the interface between the electrode (e.g. WE) and the electrolyte. It is composed of two layers, the fixed and the mobile one. The fixed one corresponds to the ions adsorbed onto the electrode surface (either negative or positive depending on the polarisation of the electrode) whereas the mobile one is composed of opposite charge ions attracted by Coulomb force to the first layer.

The relevance of such a double layer lies in the fact that it acts as a capacitor. Meaning that when the WE is being charged, the EDL must be charged as well. This accumulation of charges at the interface generates a capacitive current that is not associated with the redox reactions (as the faradic current is), therefore, must be separated during data interpretation [76]. Figure 2.14 allows us to visualise the correct interpretation of the capacitive current (charging current) and the faradic current. The faradic current should always be measured using the capacitive current as a baseline. The capacitive

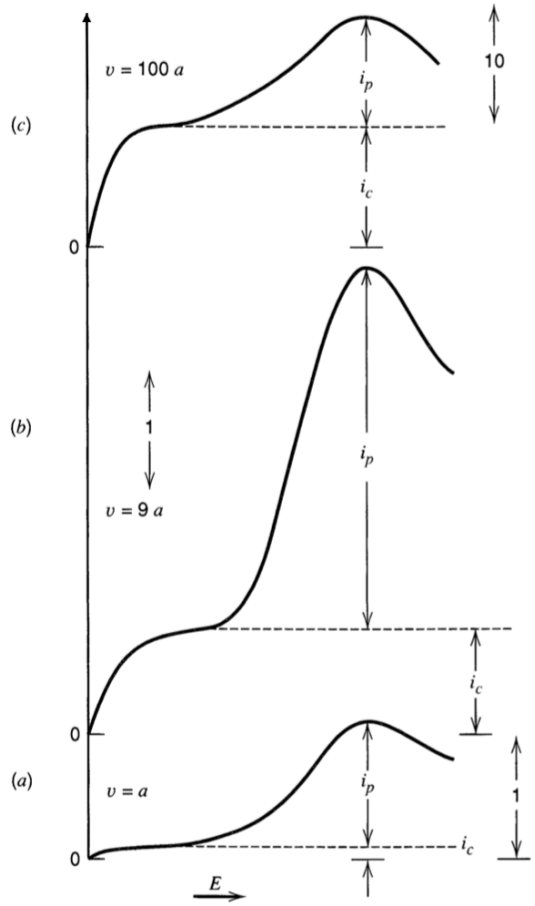

Figure 2.14: Effect of double layer charging at different sweep rates, showing the magnitude of capacitive charging current (I_c) and the faradic peak current (I_p). The current scale in (c) is 10X than in (a) and (b) [5]

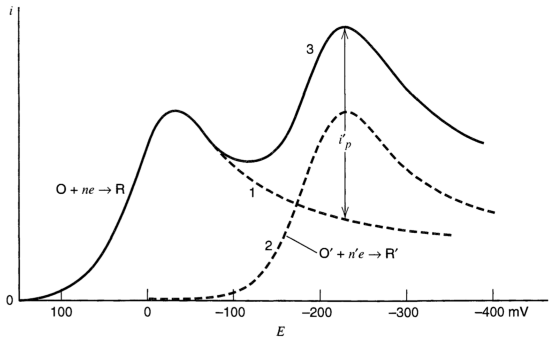

Figure 2.15: Interpretation of baseline for overlapped peaks during voltammetry [5]

current is susceptible to the scan rate, becoming more important at high scan rates [5].

Additionally, it is important to take into account the situation in which overlapping of peaks occurs. Figure 2.15 shows an example of such a case in which the baseline for the second peak must be taken from the foot of the first peak. However, such an interpretation of data is quite complicated to determine in reality. Therefore, despite the great advantages of cyclic voltammetry, it cannot be considered as a precise technique for quantification due to the difficulties measuring the capacitive charging current [5].

3

Experimental part

This chapter describes in detail the methodology[1] followed to study the interaction of hydrogen with 304L stainless steel and Invar alloy by different analytical techniques. Three stages were followed to conduct the study on the material: initial characterisation of the materials by XRF, XRD, and microscopy, hydrogen sorption-desorption behaviour study by electrochemical methods (cyclic voltammetry), and analysis of the effect of hydrogen intake on the material by XRD, and microscopy.

3.1. Materials

The 304L nominal stainless steel and the Invar alloy materials were provided by GTT company in laminates of 20 x 20 cm^2 with 1.2 mm and 0.7 mm thickness, respectively. Besides, the welded regions of these two materials were tested out. Figure 3.1 shows the regions of both materials (304L and Invar) subjected to analysis. For all the samples described bellow cut pieces of 20 x 16 mm^2 were used.

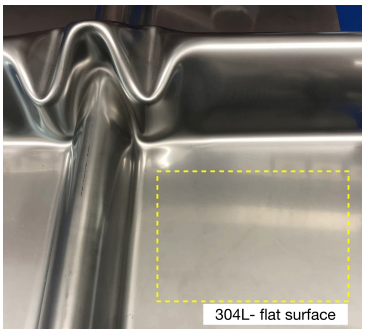

(a) 304L flat region

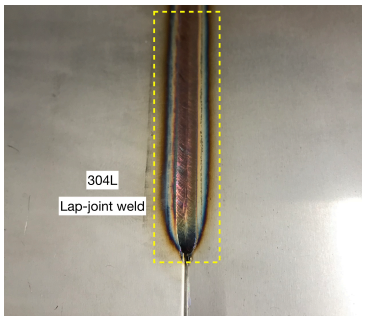

(b) 304L lap-joint weld

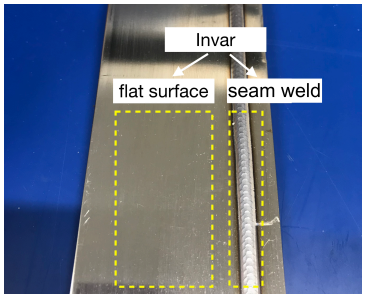

(c) Invar flat region & seam weld

Figure 3.1: Materials and correspondent regions tested out

[1]The methodology was based on a great extent on [44] and [67].

3.1.1. Sample preparation

Different surface finishes were tested for each type of material. Table 3.1 summarises the specifications of each sample tested out. In the case of the flat regions (both materials), whenever possible, three replicas were measured per loading time.

In the particular case of as-received 304L (after XRF characterisation) it was found that the material was coated with a TiO2 layer. Therefore, the as-received 304L (coated with TiO_2) and the uncoated 304L (polished) were treated as two different samples.

Table 3.1: Samples tested out for the Mark III and NO96 technologies

Technology		Part	Surface finishing	Remarks	H_2 loading Time
Mark III:	304L	Flat sections	as-received polished sanded	**Coated** with TiO_2 **Uncoated**, polished up to 1um with sanding paper grit #1200	30min, 60min, 90min, 2h 30min, 90min, 12h, 24h, 48h 30 min
		Lap-joint weld	as-received	-	30 min
NO96:	Invar	Flat sections	as-received polished sanded	- up to 1um with sanding paper grit #1200	30 min 30min, 60min, 90min, 2h, 12h 30 min
		Seam weld	as-received	-	30 min

3.2. X-Ray Fluorescence (XRF)

XRF analysis was conducted to study the chemical composition of the materials. The measurements were performed with a Panalytical Axios Max WD-XRF spectrometer and data evaluation was done with SuperQ5.0i/Omnian software.

3.3. Microscopy

To reveal the microstructure, the samples were polished and etched before being investigated using microscopy. The etchant composition and etching time for each material are described in table 3.2. Both optical and scanning electron microscopy techniques were applied to observe the samples in three stages:

1. Before H_2 exposure
2. After H_2 sorption, meaning that the electrochemical experiment stopped after having finished the chronoamperometric technique (details on section 3.5).
3. After H_2 desorption, meaning that the electrochemical experiment stopped after the four consecutive CV scans after H_2 loading (theoretically no hydrogen should be adsorbed on the surface anymore because it was electrochemically desorbed).

A *Leica DMLM* optical microscope and *JEOL JSM 6500F* scanning electron microscope were used for each technique, respectively. The SEM images were taken at 20 kV of acceleration voltage and 11 mm of working distance.

Table 3.2: Chemical composition of the etchants and time conditions used for revealing the microstructure of 304L and Invar samples.

Sample	Etchant composition	Remarks	Time
Uncoated 304L,[60]	2 mL HF 4 mL HNO_3 100 mL H_2O	Inmersion	Polished non-exposed to H_2: 12-13 min Polished exposed to H_2: 8 min
Invar,[38]	4g $CuSO_4$ 20 mL HCl 20 mL H_2O	Swab or immersion	Polished non-exposed to H_2: 1 min Polished exposed to H_2: 20-30 s

3.4. X-Ray Diffraction (XRD)

3.4.1. Identification and semi-quantification of phases

The XRD analysis was conducted for studying the phases present in each material. For the Invar and welds, only identification of phases was conducted.

On the other hand, the uncoated 304L stainless steel was subjected to a semi-quantification of phases to verify any possible changes in the percentage volume fraction of the phases after the H_2 loading because the results showed that it consisted of a two-phase material. To get rid of the texture effect, several scans were conducted at different ψ angles (from 0 to 60°). Next, the resultant XRD pattern comes from the sum of the scans at different tilting angles over which the semi-quantification was done. The I/Icor and relative intensity values were calculated with *Powdercell*, because the information of the ICDD pdf cards was not reliable. Because in the sum-scan only one clear peak of the ferrite phase was visible, the intensities were determined with *Topas6*. Table 3.3 describes the equipment and settings used in detail.

3.4.2. Residual stress and strain & strain-free lattice parameter

Residual strain and stress measurements were conducted to check the state of the sample before and after H_2 exposure according to the settings described in table 3.3 but only using the 2θ region between 80 to 100° including the Fe(200) reflection. Additionally, these measurements allow calculating the free-strain d-spacing (d_0), according to equation 3.1, and consequently the true lattice parameter.

$$\sigma_\phi = \frac{E}{(1+\nu)\sin^2\psi}\left(\frac{d_\psi - d_0}{d_0}\right) \tag{3.1}$$

Table 3.3: Settings for identification, semi-quantification of phases and residual stress measurements by XRD

	Measurement	
Conditions	**Uncoated 304L & Residual stress**	**Invar & Welds**
Instrument	Bruker D8 Discover with Eulerian cradle with parallel beam geometry	Bruker D8 Discover diffractometer, Incoatec Microfocus Source (IμS)
Emission source	Co Kα radiation, 45 kV 25 mA	Cu Kα1 radiation, 50 kV 1000 mA
Wavelength	1.790260 Å	1.54060 Å
Penetration depth	11 μm for Fe {111} reflection	1.8 μm for Fe {111} reflection
Measurement	The scans at different tilting angles are recorded while spinning the sample at 16 rev/s. Locked coupled 30-130° 2θ, step 0.04, time 2 s, ψ 0 to 60°, steps 5°	Continuous coupled θ-2θ scan 20°-140°, step size 0.020° 2θ, counting time per step 5 s for Invar counting time per step 1 s for welds
Data Evaluation	Bruker DiffracSuite EVA, Powdercell, Topas6, Panalytical Xpert Stress 2.0	Bruker software DiffracSuite.EVA vs. 5.1.

Where E corresponds to Young's modulus and ν to the Poisson's ratio. The diffraction angle (2θ) corresponding to the plane {220}, at a fixed rotation angle (ϕ) and different tilting angles (ψ), and the corresponding value of the wavelength (table 3.3) were used to calculate the d according to equation 3.2 (Bragg's Law adapted for hkl=220):

$$\lambda = 2 \cdot d_{220} \cdot \sin(\theta_{220}) \tag{3.2}$$

Where λ is the wavelength of the X-ray source, d is the inter-planar spacing of the diffracted plane and θ is the incident angle of the X-ray beam.

Next, the $\sin^2\psi$ method was employed to calculate the residual stress. The method consists of plotting the inter-planar d-spacing on the y-axes vs. $\sin^2\psi$ on the x-axes as shown in the figure 3.2. The stress can be calculated from the slope of the curve (m) and the elastic properties of the material [19].

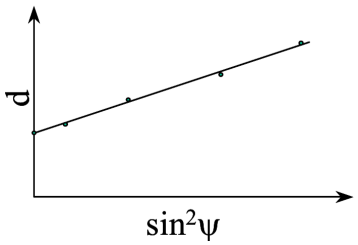

Figure 3.2: Example of d vs. $\sin^2\psi$ plot,[19]

3.5. Cyclic Voltammetry

3.5.1. Electrochemical cell: set-up

Electrochemical measurements were performed in a one-compartment acrylic cell. The electrolyte was a $1M$ KOH solution containing 4 g/L of thiourea[2]. The correspondent pH solution was registered in the range between 13.4 to 13.6[3]. A three-electrode configuration was selected, as depicted in figure 3.4a. A double junction $Ag/AgCl_{sat}$ electrode filled with a $4M$ KCl solution was used as a reference (RE), a platinum sheet square as a counter (CE), and the sample as working electrode (WE).

Sticky copper tape was glued in the backside of the sample 3.4b to facilitate the electrical connection. Then, the sample (flat sections only) was clamped in between the support and the cell, exposing only a circular area of about 0.5 cm^2, as shown in figure 3.3c. In the case of the welds, the entire surface (front and back sides) of the sample was masked except for a circular area of about 0.126 cm^2 corresponding to the exposed area. Figure 3.4 shows the electrochemical cell configuration for the welded regions.

The potential of the RE was measured against a well-known potential of a saturated calomel electrode (SCE), before and after the electrochemical experiment, to verify the stability of the reference potential. A slight decrement (-4mV) of the reference potential was detected after 48h of immersion of the RE in the KOH electrolyte. In addition, the filling solution of the RE was renewed periodically (at least once a week) to minimise the effect of contamination.

The experiment was conducted in a *Bio-Logic VSP-300* potentiostat that uses the software *EC-Lab®*. The set up of the experiment consisted of three consecutive electrochemical techniques (the sample was not removed in between the steps):

[2]Thiourea acts as a recombination poison, retarding H_2 gas formation, [67]
[3]The pH variability results from variations when weighting the reagents to prepare the solution

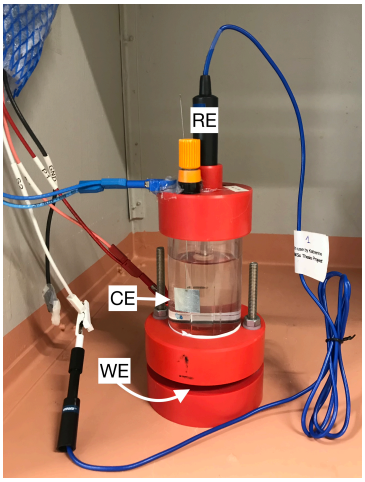

(a) Three-electrode mode: WE in horizontal position

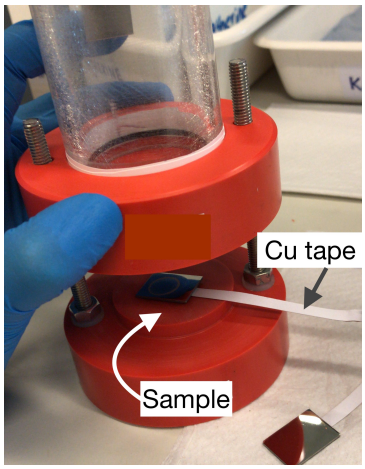

(b) Sample attachment in the clamp

(c) Cell inner view

Figure 3.3: Electrochemical cell configuration for flat samples

1. Cyclic Voltammetry (CV) ⟶ 2 scans
   1st scan: cleaning step
   2nd scan: baseline

2. Chronoamperometry (CA) ⟶ different loading times
   This is the step in which the HER takes place. In other words, hydrogen is evolving on the working electrode surface.

3. Cyclic Voltammetry ⟶ 4 scans
   1st scan: in which the hydrogen desorbed[4] is detected as a new peak in the cyclic voltammogram. Consecutive scans were performed to check the oxidation state of the metal surface.

The samples were characterised at two stages:

- **After sorption**: when the sample was removed from the electrolytic cell after the chronoamperometric step (step 2). Meaning that the HER took place for a certain period of time, but no other redox processes were involved until that point.
- **After desorption**: when the sample was removed from the electrolytic cell after having completed the 4th CV scan of the second cyclic voltammetry step (step 3).

The detail of the parametrisation of the methods are shown in figure 3.5 (taking as an example, the potential range for Invar). The sweep rate used is 0.01 V/s. For the cyclic voltammetry, one cycle is

[4]Only hydrogen desorbed associated with Heyrovsky step can be detected as a current response

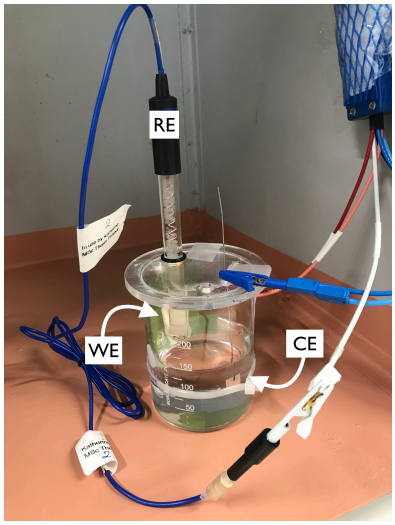

(a) Three-electrode mode: WE in vertical position

(b) Sample masking (3M^{TM} electroplating tape 470)

Figure 3.4: Electrochemical cell configuration for the welds

defined by three potentials: Ei the initial potential, $E1$ the vortex potential up to which the potential goes and turns back, and $E2$ as the final potential. In this case of study, $Ei = E2$ so that the cycle is closed. For the chronoamperometry technique, the potential at which the sample is kept during a certain time is the same as initial potential Ei in the cyclic voltammetry step 3.4.

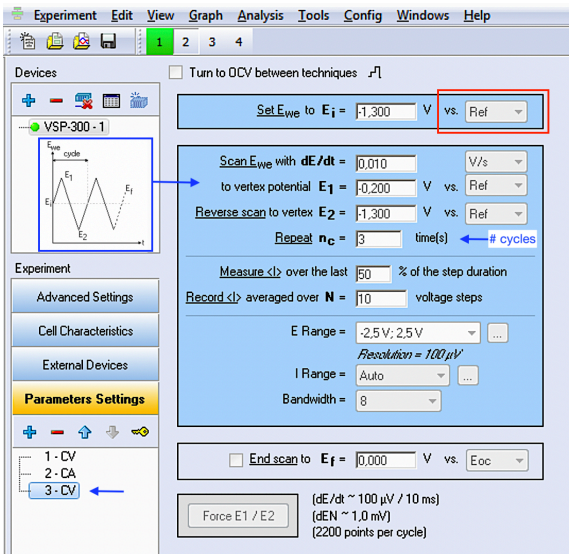

(a) Cyclic Voltammetry

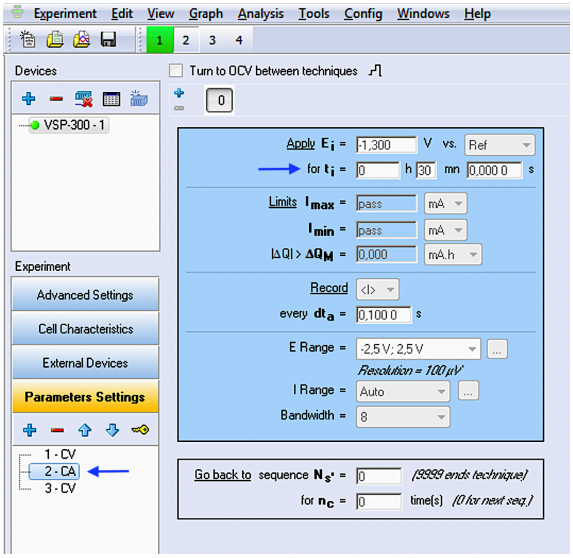

(b) Chronoamperometry

Figure 3.5: Parametrisation of electrochemical techniques in *EC-Lab* for an Invar sample

The potential range (Ei to $E2$ in figure 3.5a) along which the cyclic voltammetry step took place for each material is shown in table 3.4. The Ei for the cyclic voltammetry technique is the same used in the chronoamperometric technique. The explanation associated with the selection of these values is detailed in section 3.5.

Table 3.4: Potential range for the cyclic voltammetry technique vs.Ag/$AgCl_{sat}$

Material	Potential range [V]	
	$Ei = E1$	$E2$
304L	-1.22	-0.2
Invar	-1.30	-0.2

3.5.2. Data Processing: Quantification of desorbed hydrogen

The amount of hydrogen evolved and adsorbed can be quantified from the variables that the potentiostat records during the experiment, more specifically through the total charge (Q). Each electron is equivalent to one hydrogen atom (either adsorbed as in equation 4 or desorbed as in equation 5). Consequently, it is possible to directly correlate with the number of hydrogen atoms, either adsorbed or desorbed. If required, the number of hydrogen molecules generates (coming from the electrochemically desorbed hydrogen atoms) can be calculated knowing that hydrogen gas is a diatomic molecule. By Avogadro's number, the correspondent mass of hydrogen can be computed.

In the case of the **amount of evolved(adsorbed) hydrogen**, corresponding to the loading step, the total cumulative charge is directly given as an output variable from the experiment during the chronoamperometric method. The charge is giving in Coulombs and is then transformed into surface charge density ($\rho_{s(evolution)}$) by diving it into the area exposed, resulting in units of ($C.cm^{-2}$).

However, for the **amount of desorbed hydrogen** corresponding to the area of the hydrogen desorption peak[5] detected on the 1st CV scan after loading. For the area calculation, it was necessary to conduct a multi-peak fitting due to the overlapping of peaks and the complexity of the baseline of the cyclic voltammogram. The software *OriginLab*, package "Peak & Baseline analyser" was used for the analysis following the procedure describe below:

1. The anodic branch (J vs. E) corresponding to the 1st CV scan after hydrogen loading is used as input data. The range of interest, in which the hydrogen desorption peak appears (maybe overlapped) is selected. The "Fit Peak (Pro)" option is selected as a goal for the analysis, as shown in figure 3.6.
2. The 2nd CV scan before hydrogen loading is used as baseline, selecting the option "Use Existing Dataset" (figure 3.7). The baseline is autosubstracted and rescaled (figure 3.8) .

[5]Only the hydrogen desorbed from the Heyrovsky reaction can be detected as current flow because it is a reaction that involves electrons exchange. However, there is a certain amount of hydrogen desorbed from the Tafel reaction that cannot be detected by electrochemical techniques because it is a purely chemical reaction.

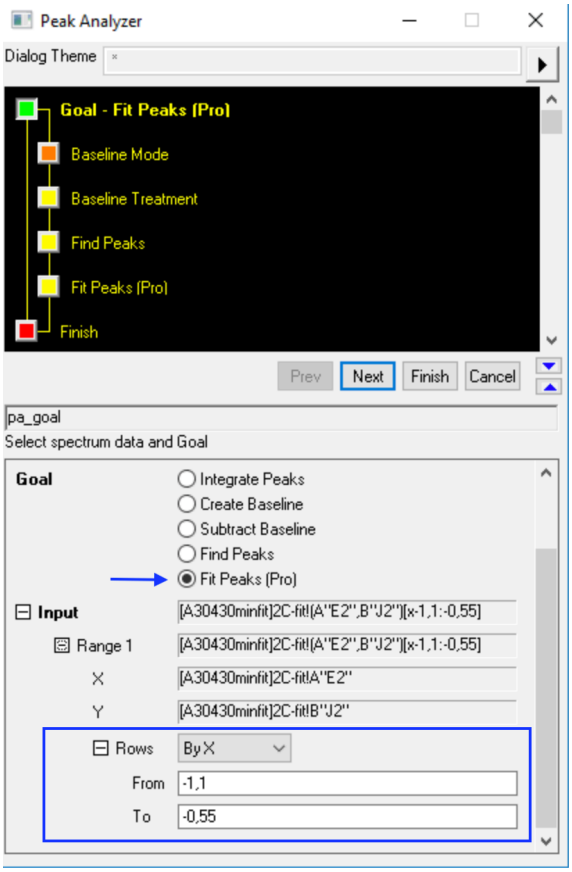

Figure 3.6: Parametrization of Goal & Input in Peak Analyzer-*OriginLab*

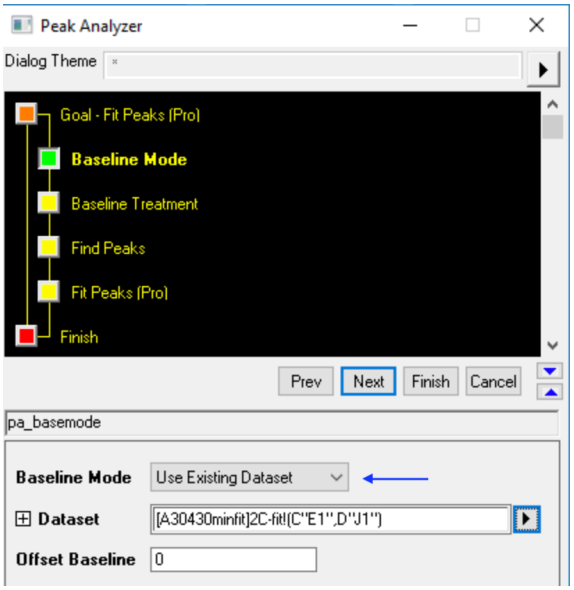

Figure 3.7: Parametrization of Baseline Mode in Peak Analyzer-*OriginLab*

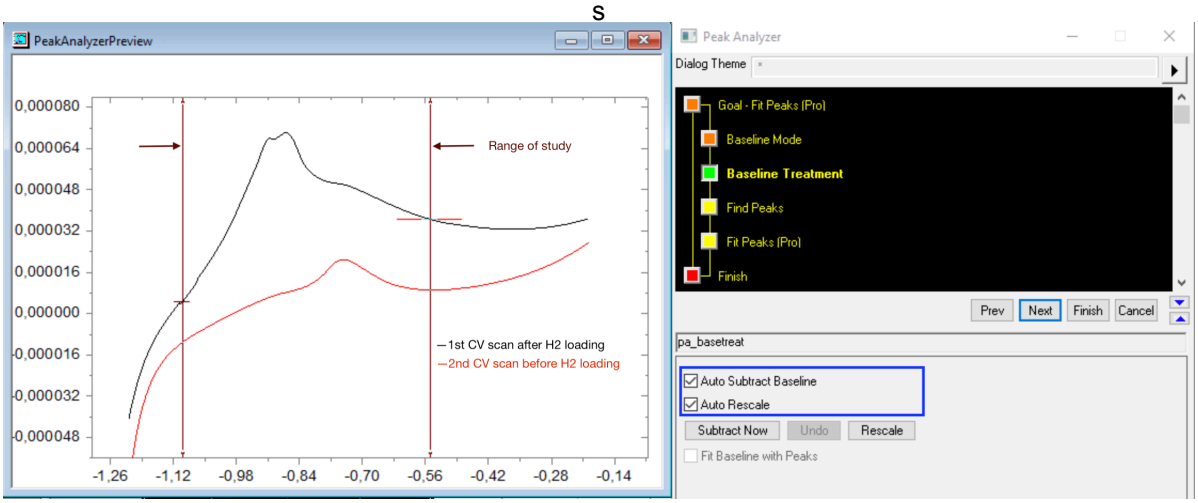

Figure 3.8: Parametrization of Baseline Treatment in Peak Analyzer-*OriginLab*

.

3. After the baseline subtraction, the output is a new curve which is now referred to zero. The peak fitting is conducted over this resulting curve. In the peak finding settings section, under the direction option, only positive peaks are allowed. Under the local points option, an adequate number needs to be selected until the number of detected peaks coincide with the assigned peaks (explained in section 4.4.3 depending on each specific case. If too many peaks are detected (with no electrochemical meaning), the number of local points needs to be increased.

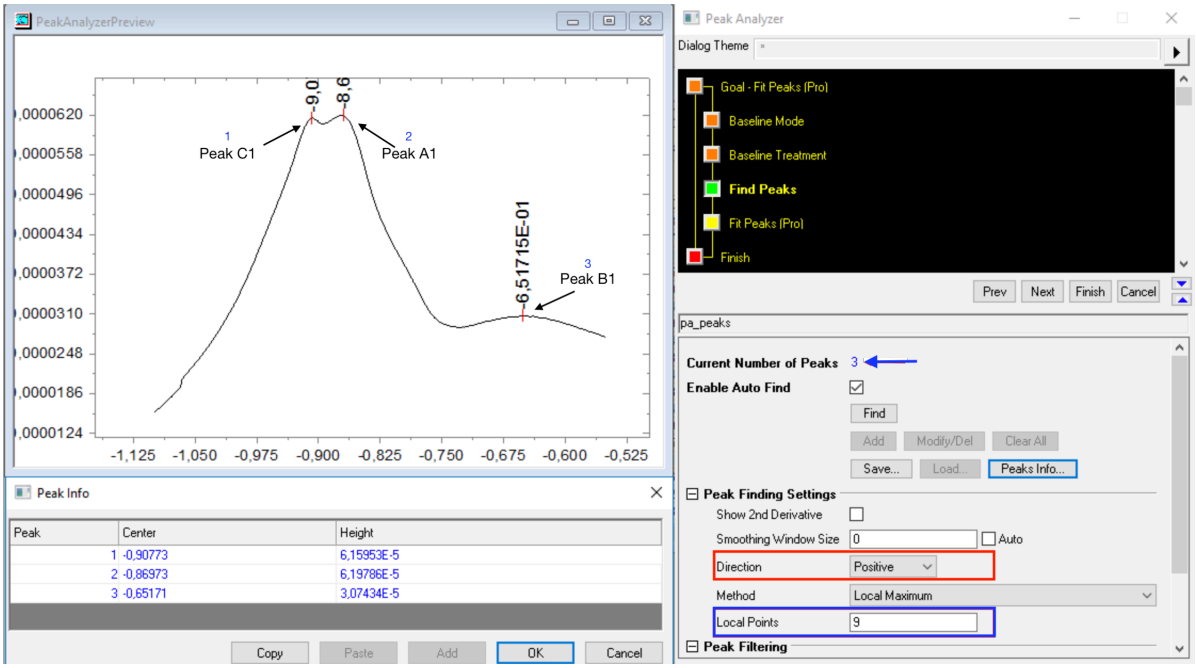

Figure 3.9: Parametrization of Find Peaks in Peak Analyzer-*OriginLab*

.

4. For the fit peak section, under the “Fit Control” button, the type of peak needs to be selected. According to literature, for cyclic voltammograms, either Gaussian or Lorentzian peaks can be used in the absence of a mathematical model for the specific case of study [4]. Additionally, the baseline parameter and the peaks’ centres were fixed before the fitting, as shown in figure 3.10.

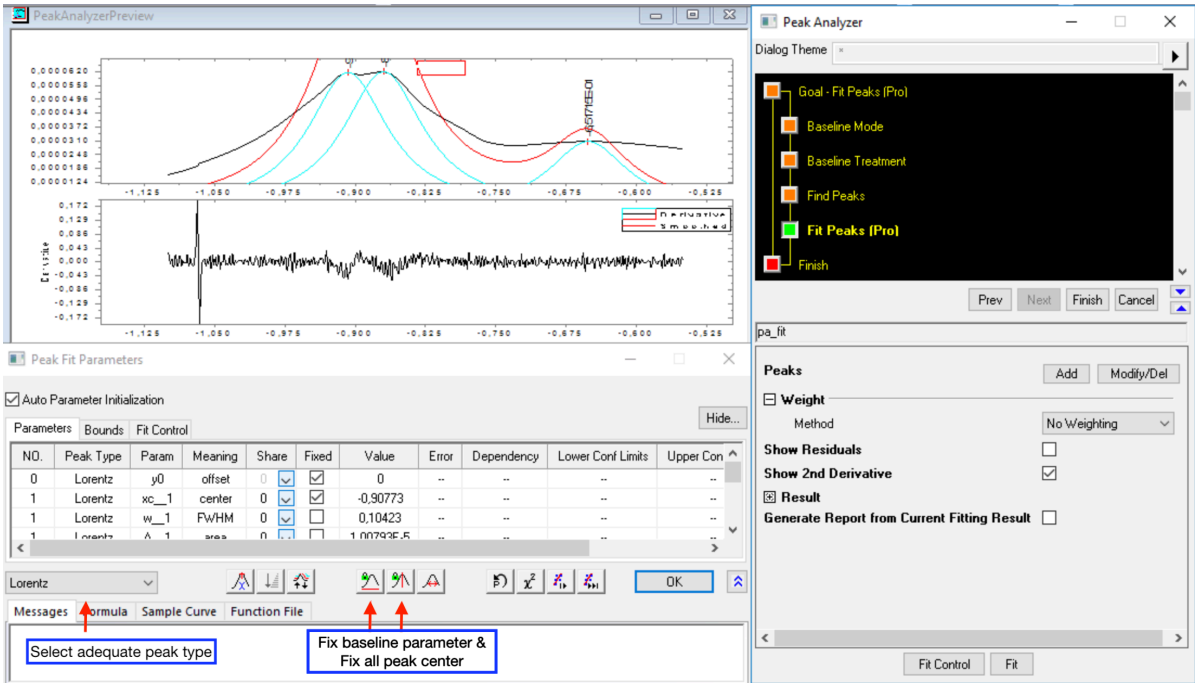

Figure 3.10: Parametrization of Fit Peaks (Pro) in Peak Analyzer-*OriginLab*

.

The selection of the range of study in step 1) and the type of peak in step 4) were varied until a reasonable fitting output, regarding the shape of peaks, was obtained. Due to the complex shape that the curve has, the fitting becomes a trade-off between a perfect fitted curve and a meaningful peak shape. For example in the case of polished 304L (sample 304L-P-30min-S1), figure 3.11 is one resulting fitting option in which the fitting is acceptable but the peak 3 is meaningless because it is known from 2nd CV scan before H_2 loading that the peak B1 in not so wide (it does not start at same potential that Peak A1). Figure 3.12 depicts three peaks that have a width that coincides with the expected values when looking at the baseline voltammogram. Therefore, the final fitting is only selected if found peaks after the deconvolution have an electrochemical correlation with the expected peaks (and their potential range) according to each specific case.

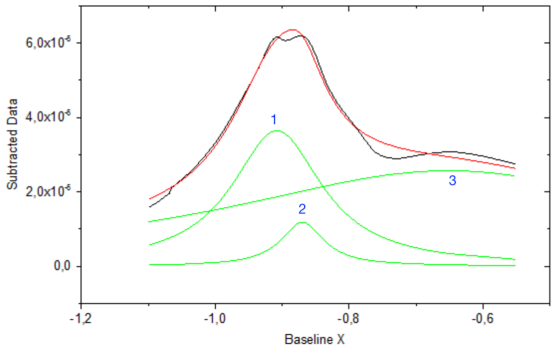

Figure 3.11: Option A of fitting for sample 304L-P-30min-S1

.

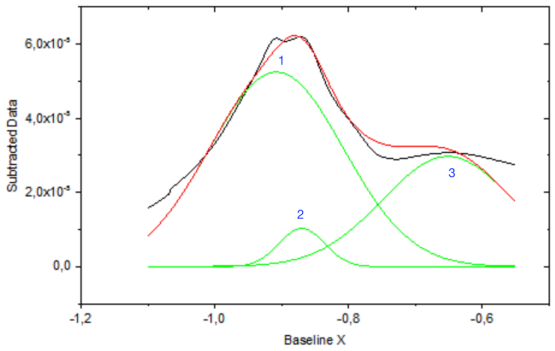

Figure 3.12: Option B of fitting for sample 304L-P-30min-S1

.

The area of the hydrogen desorption peak after the fitting is obtained in units of ($A \cdot V \cdot cm^{-2}$). To be transformed into surface charge density, it has to be divided into the sweep rate, which is **0.01 V/s** for all the cases (equation 3.3). The units' correspondence is shown in equation 3.4.

$$\rho_{s(desorption)} = \frac{peak\ area_{(desorption)}}{scan\ rate} \tag{3.3}$$

$$\left[\frac{C}{cm^2}\right] = \left[\frac{\frac{A}{cm^2} \cdot s}{\frac{V}{s}}\right] = \left[\frac{A \cdot V}{cm^2}\right] \tag{3.4}$$

It is important to point out how the sign of the charge density correlates with the electrochemical process going on. During the H_2 loading step, the charge is negative due to the contribution of the electrons coming from the adsorbed dissociated hydrogen atoms (on the WE) whereas the charge for the desorption peak is positive due to the holes left by electrons of the hydrogen atoms that have recombined (gas formation).

The efficiency of the electrochemical adsorption process (eq.3.5) is obtained by comparing the surface charge density evolved during the loading step (CA step) and the surface charge density corresponding to hydrogen desorption peak found on the anodic branch the 1st CV scan after the H_2 loading step.

$$\eta_{electrochemical\ adsorption} = \frac{\rho_{s(evolution)}}{\rho_{s(desorption)}} \propto \frac{H_{(adsorbed)}}{H_{(desorbed)}} \tag{3.5}$$

4

Results and Discussion

4.1. XRF

The chemical composition of the 304L stainless steel (after having removed the TiO_2 layer on top of the steel) and Invar alloy are detailed in tables 4.1 and 4.2, correspondingly.

Table 4.1: Chemical composition (wt%) of as-received 304L stainless steel (balance Fe)

Material	C	Cr	Ni	Mn	Si	Cu	Mo	P	S	Others
304L	0.019	18.07	9.22	1.25	0.53	0.31	0.15	0.03	0.01	0.36[1]

Table 4.2: Chemical composition (wt%) of Invar® alloy

Material	Fe	Ni	Mn	Si	Cr	Mo
Invar	63.25	36.17	0.33	0.17	0.05	0.02

4.2. Optical (OM) & Scanning Electron (SEM) Microscopy

This section details the observations obtained by the microscopy analysis.

4.2.1. Uncoated 304L

Initial state: before H_2 exposure

Figure 4.1 shows the microstructure of 304L before H_2 exposure observed by OM and SEM. The grain boundaries are well defined; the grain size varies from 20 to 80 μm. Additionally, several twins are observed which are distinctive from austenite phase.

[1] Including V, Ta, Nb, Cl, and Al

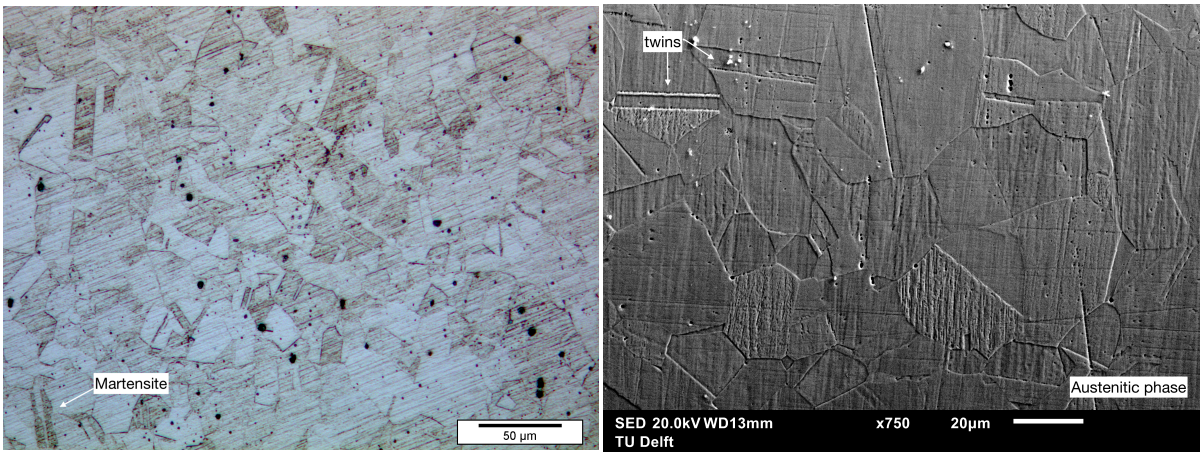

(a) OM x200 **(b)** SEM x750

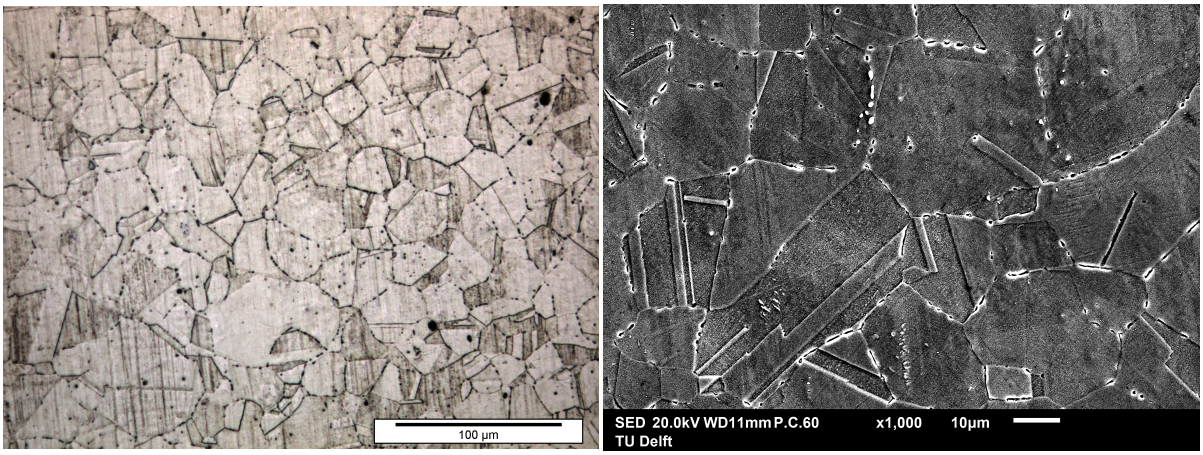

(c) OM x200 **(d)** SEM x1000

Figure 4.1: 304L stainless steel before H_2 exposure, etched

After H_2 exposure

Figure 4.2 shows how the surface after treatment looks like after the sorption and desorption process, respectively. The circle corresponding to the treated surface exhibits a slightly brownish colour that can only be distinguished, pointing light against the sample.

When looking at the exposed area by SEM without any etching process (figure 4.8), it is clear to distinguish the formation of a layer on top of the metal. The sample after sorption (figure 4.3a) presents a layer that seems to be thinner than the one after desorption (figure 4.4b). This appreciation is motivated by the fact that there are several spots that are not covered by this layer (bare metal can be seen) and because the border of such a layer does not present a relief on the surface as for the one after desorption. However, this is just a qualitative appreciation since the thickness of such a layer could not be quantified by the analytical techniques used in this work.

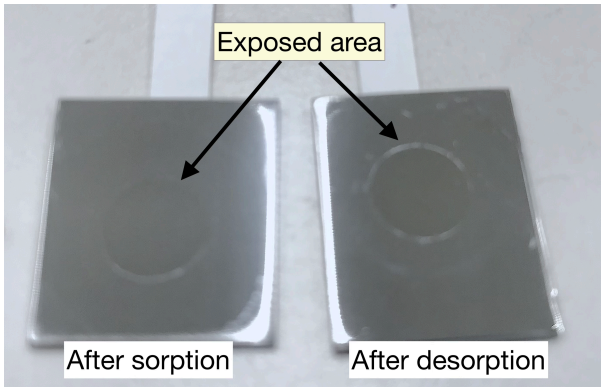

Figure 4.2: Polished 304L samples after sorption and desorption, no etched

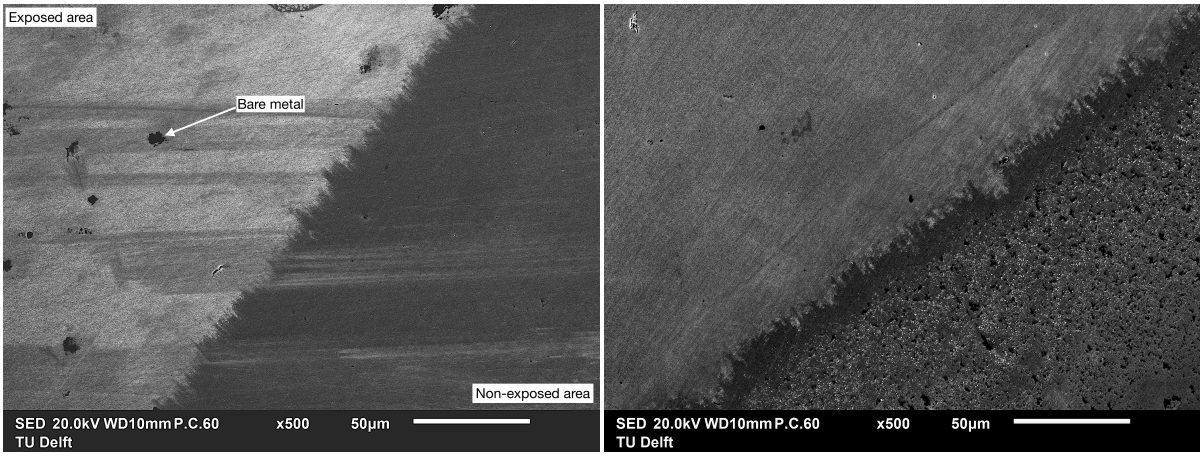

(a) SEM x500 after sorption **(b)** SEM x500 after desorption

Figure 4.3: 304L after H_2 exposure, no etched

Later, the same samples were etched to reveal the microstructure (figure 4.4). No significant difference in the microstructure was observed between the sample after H_2 exposure (figures 4.4a and 4.4b) and the microstructure of the sample before H_2 exposure (figure 4.1). Morgan et al. [43] report that after three weeks of exposing 304L stainless steel to pressurised hydrogen (69 MPa and 350^{o}C) no significant microstructural changes were observed by optical microscopy (no change in the amount of induced martensite). Considering that the conditions at which that experiment was conducted (high pressure and long exposure time) resulted in no changes, it seems logical that for a maximum period of 48 h, in the case of the present work, no differences can be observed between the treated and non-treated samples. However, they report that the stress-strain behaviour of the as-received and exposed samples was different. This will be analysed in section 4.3.

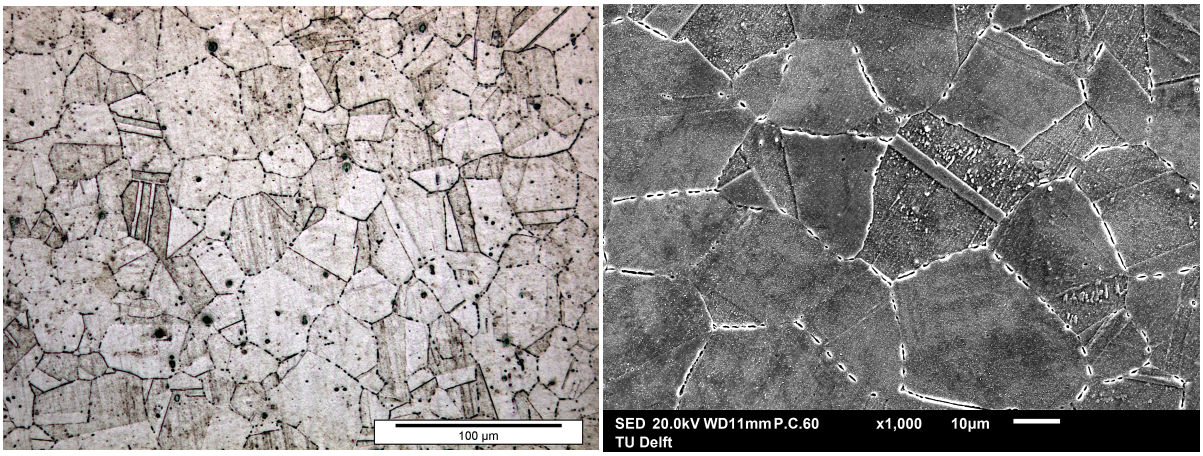

(a) OM x200 after 48 h of H_2 loading **(b)** SEM x1000 after desorption

Figure 4.4: 304L after 48 h of H_2 loading, etched

4.2.2. Coated 304L (with TiO_2 layer)

Initial state: before H_2 exposure

Figure 4.5 shows the as-received TiO_2 coating on top of the 304L stainless steel. Some sort of "grains" in different sizes are exhibited. The zoom-in of the surface of these grains shows a rough surface.

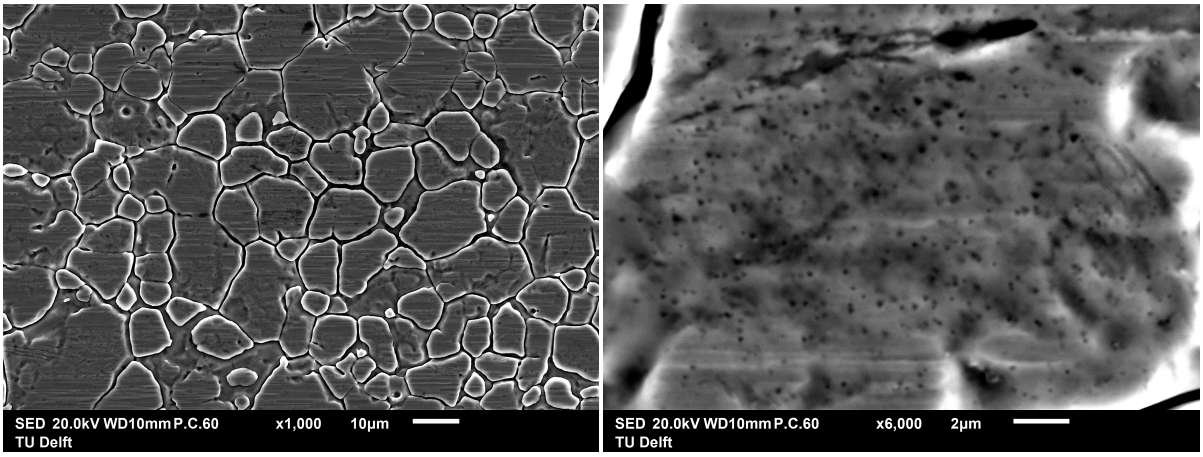

(a) SEM x1000 **(b)** SEM x6000

Figure 4.5: TiO2 coating of 304L stainless steel before H_2 exposure, no etched

After H_2 exposure

No changes at all were observed on the surface after the H_2 desorption process.

4.2.3. Lap joint weld joining two coated 304L sheets

Before H_2 exposure

Figure 4.6 shows the lap joint weld corresponding to 304L in its original state. An orange/brown colouration is observed all over the welded area corresponding to trevorite ($NiFe_2O_4$) oxide, according to the XRD analysis (section 4.3.2). Characteristic rings resulting from the welding process are distinguished.

After H_2 exposure

Figure 4.7 shows how the lap joint weld looks like after H_2 desorption. The area exposed is darker than the weld region before exposure. Another oxide is present corresponding to hematite (Fe_2O_3), detailed in section 4.3.2.

Figure 4.6: OMx100 - Lap joint weld before H_2 exposure, no etched

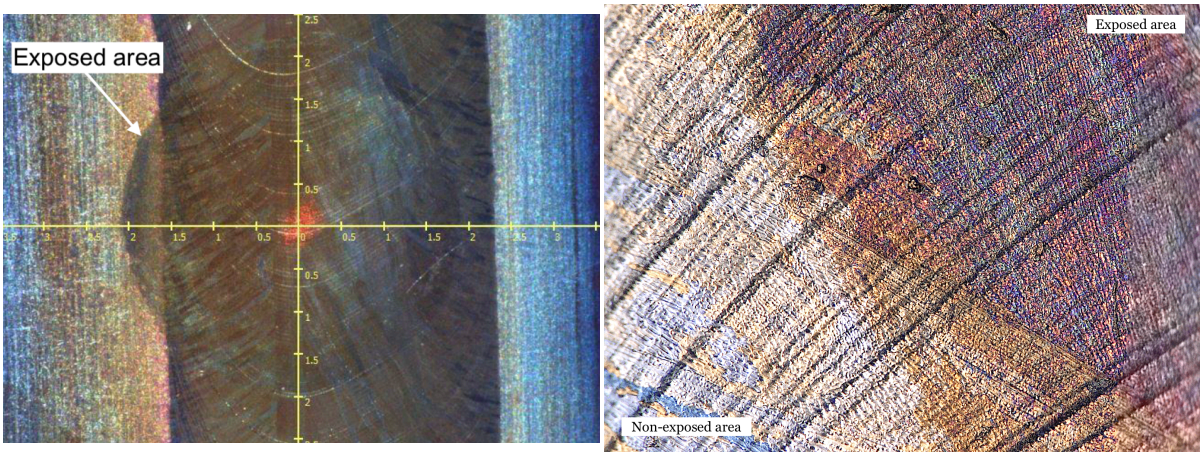

(a) Exposed area

(b) OM x500

Figure 4.7: Lap joint weld of 304L after H_2 desorption, no etched

4.2.4. Invar

Before H_2 exposure

Figures 4.8 shows the initial state of the microstructure of Invar (after etching) before H_2 exposure. Invar is a one-phase material (austenite), the presence of twins is observed. Grain size varies between 2 to 30 μm.

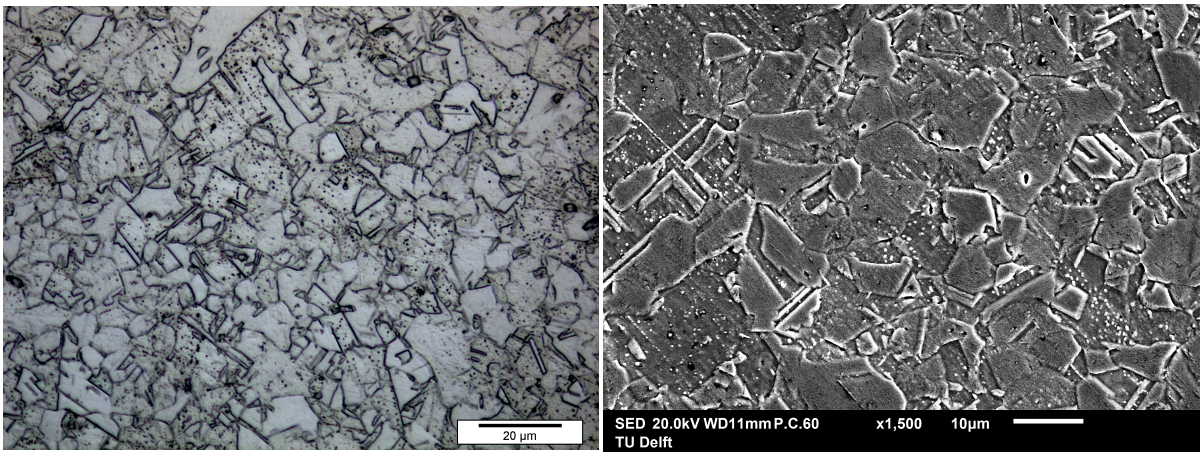

(a) OM x500 **(b)** SEM x1500

Figure 4.8: Invar before H_2 exposure, etched

After H_2 exposure

Figure 4.9 presents how the material looks like after H_2 exposure. It is evident to notice that the exposed area has become brown. Two different stages after exposure are shown: after sorption characterised by a light brown colouration and the stage after desorption in which the exposed area presents a dark brown colouration which corresponds to a layer formed on top of the metal as shown in figure 4.10. This colouration is characteristic of an iron oxide layer which is expected to be formed at the working pH and potential (as deduced in section 4.4.3).

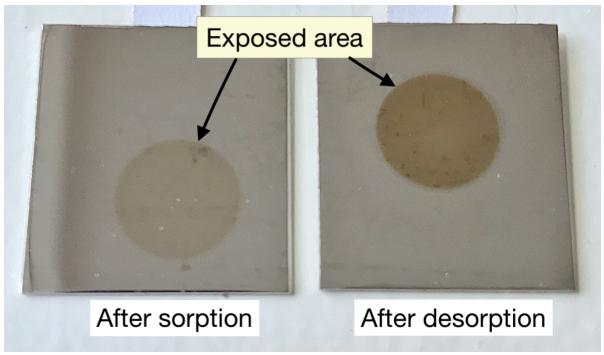

Figure 4.9: Polished Invar samples after sorption and desorption, no etched

Figure 4.11 presents the microstructure of Invar after H_2 exposure. If comparing with 4.8b, it is clear that the valleys of the surface are covered by some material which presumably corresponds to residues of the oxide layer previously formed. Additionally, comparing the surface topology of a sample observed just after sorption with one observed after desorption, a slight difference is shown. After sorption (4.11a) certain areas are not covered by these “lumps” whereas after desorption (4.11b) all the valleys are completely covered. This observation can be another indication that the oxide layer grows while hydrogen desorbs from the Invar, as shown in figure 4.9.

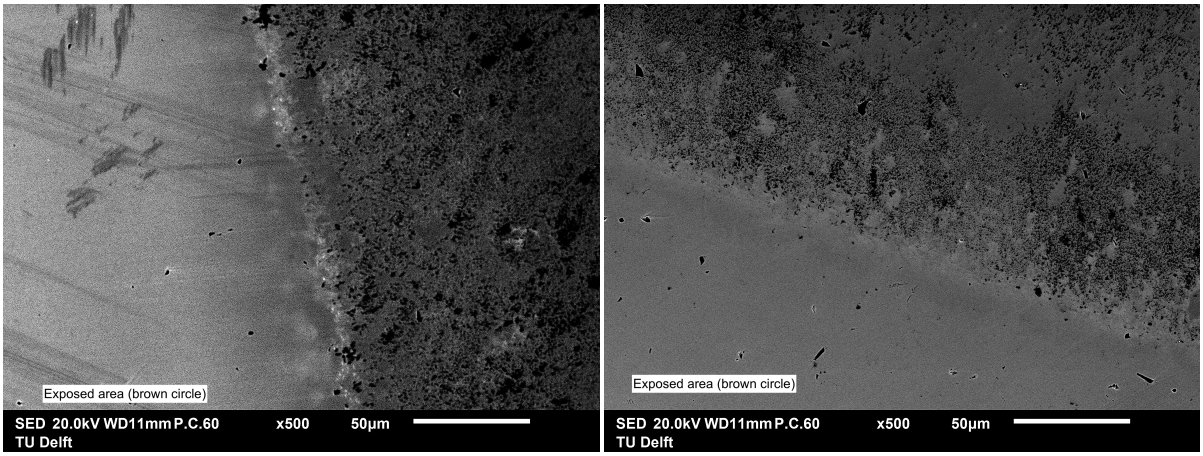

(a) SEM x500 after sorption **(b)** SEM x500 after desorption

Figure 4.10: Invar after H_2 exposure, no etched

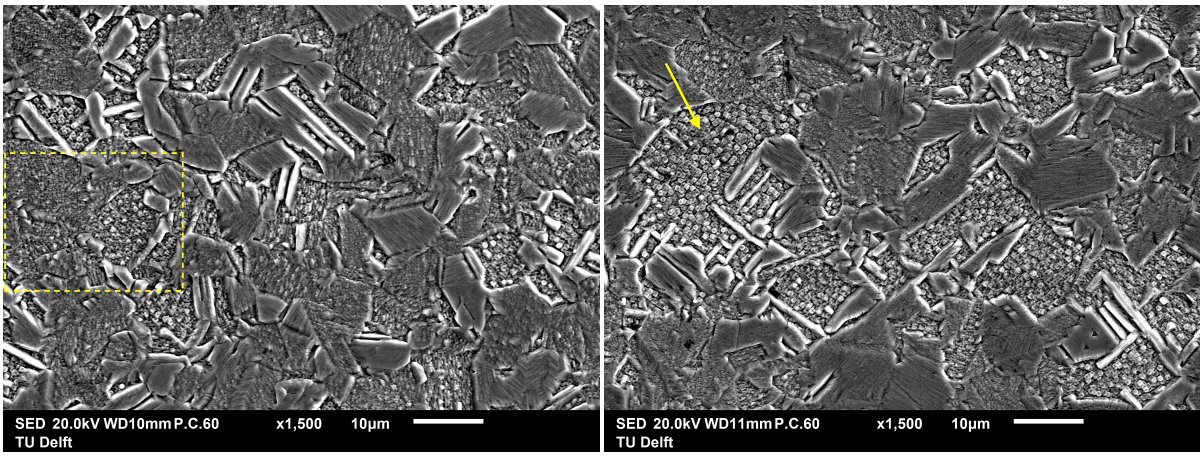

(a) SEM x1500 after sorption **(b)** SEM x1500 after desorption

Figure 4.11: Invar after H_2 exposure, etched

4.2.5. Seam weld joining two Invar sheets

Before H_2 exposure

Figure 4.12 shows the seam weld before hydrogen exposure. There is an oxide layer covering al the surface corresponding to a combination of trevorite and hematite oxides (detailed in section 4.3.4).

After H_2 exposure

Figure 4.13 shows how the seam weld joining Invar sheets looks like after H_2 desorption. The area exposed turned black/brown. XRD results found the same phases as before trevorite and hematite. However, the trevorite-hematite ratio before and after hydrogen exposure might have changed.

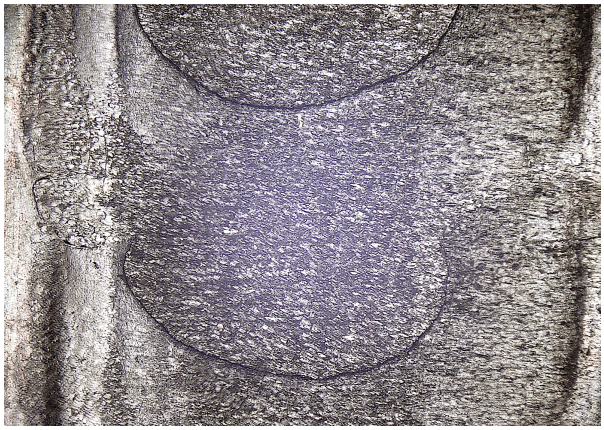

Figure 4.12: Seam weld of Invar before H_2 exposure OM x100, no etched

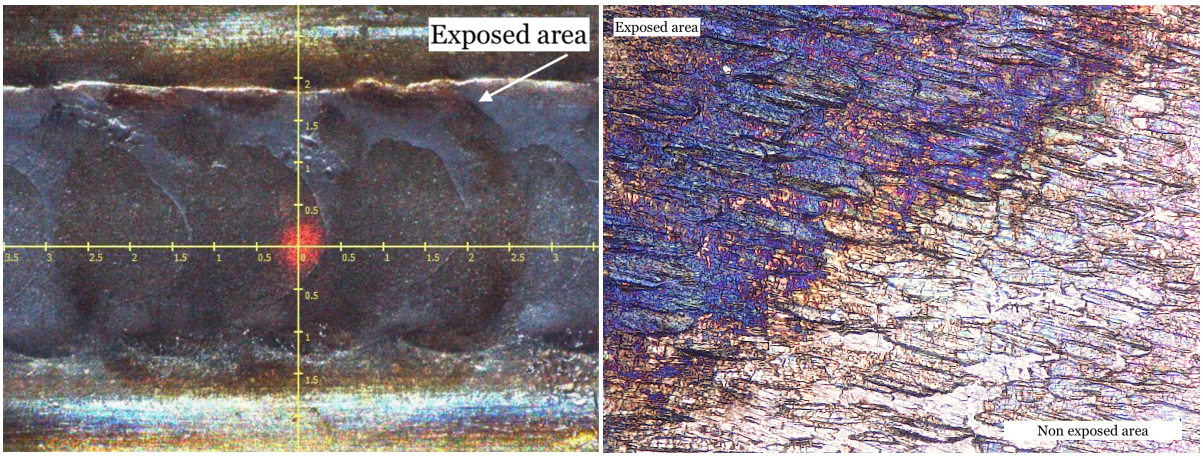

(a) Exposed area after desorption **(b)** OM x500 after desorption

Figure 4.13: Seam weld of Invar after H_2 exposure, no etched

4.3. XRD

This section presents the XRD patterns obtained before and after hydrogen loading for the different sections tested out. Also, the identification of phases and residual stress measurements are presented.

4.3.1. Uncoated 304L

Initial state: before H_2 exposure

Figure 4.14 shows the XRD pattern of uncoated 304L stainless steel in its original state. The most contributing peaks correspond to the austenitic iron phase (γ-Fe). Nonetheless, two small contributing peaks corresponding to the iron ferritic phase (α-Fe) were identified as well (pointed out with red arrows). The semi-quantification of these phases is presented in table 4.3. The results show that uncoated 304L is a two-phase material with an austenitic matrix and a small percentage of ferrite in it. The strain-free lattice parameter of the 304L stainless steel in its original state was $a_0 = 3.5907$ Å.

Table 4.3: Semi-quantification of phases present in polished-uncoated 304L before H_2 exposure detected by XRD

Database PDF[2]	Phase	Crystal structure	Volume fraction [wt%]
Fe0.7Ni0.3 (Taenite)	Austenite	FCC	95.2±1.2%
Fe,Ni (Kamacite)	Ferrite	BCC	4.8±1.2%

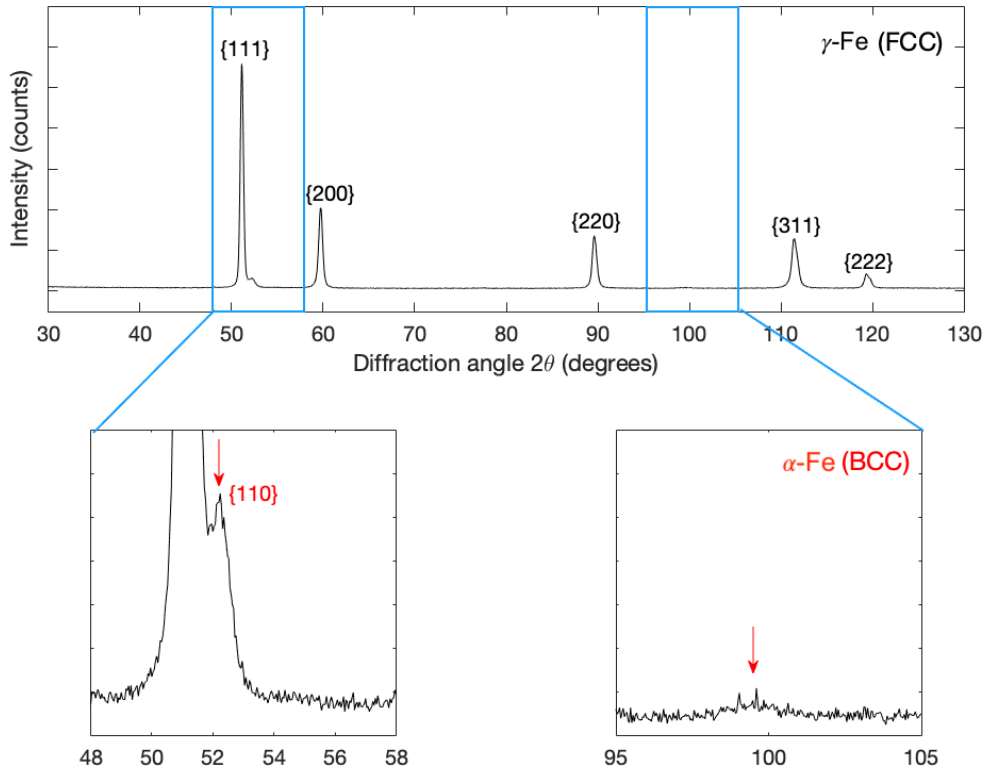

Figure 4.14: XRD pattern (sum of scans at different ψ from 0 to 60°) of polished-uncoated 304L before H_2 exposure (baseline)

After H_2 exposure

Figures 4.15 and 4.16 show the XRD patterns of the samples after the H_2 sorption and desorption, respectively. For each state evaluated (each loading time), a different sample was analysed by XRD.

In figure 4.15 it is shown how the intensity of the peaks corresponding to the austenitic phase after sorption is consistently higher (taller peaks) than the baseline, for loading times of 24 h and 48 h. For the 90 min loading, the height of the peaks is almost the same as for the baseline. Ronenak and Bergman(2005) studied phase transformations in austenitic stainless steels electrochemically charged with hydrogen reporting an increment of the intensity of the diffraction line of the {200} reflection corresponding to the $\gamma_{Hydride}$ phase with the increment of the charging time [54]. Therefore, it might be possible that the increment of the intensity in the diffraction peaks is related with the $\gamma_{Hydride}$ phase presence (explained in more detail in the following paragraphs).

[2]Powder Diffraction File

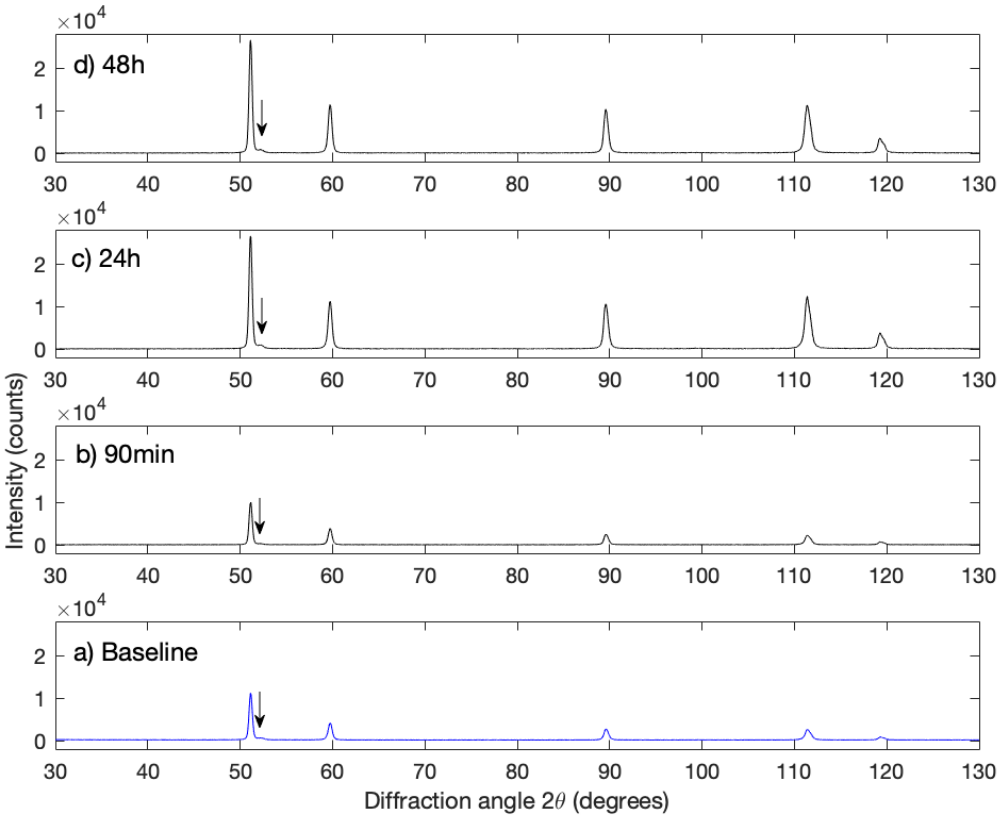

Figure 4.15: XRD patterns (sum of scans at different ψ angle from 0 to 60) of polished-uncoated 304L after H_2 sorption for different H_2 loading times

On the other hand, when looking at the behaviour of the samples after H_2 electrochemical desorption (figure 4.16), the first thing to point out is that the variation of the peaks' intensities are not that significant as it was after sorption. A zoom-in of the ferrite peak's variation is presented in figure 4.17 .

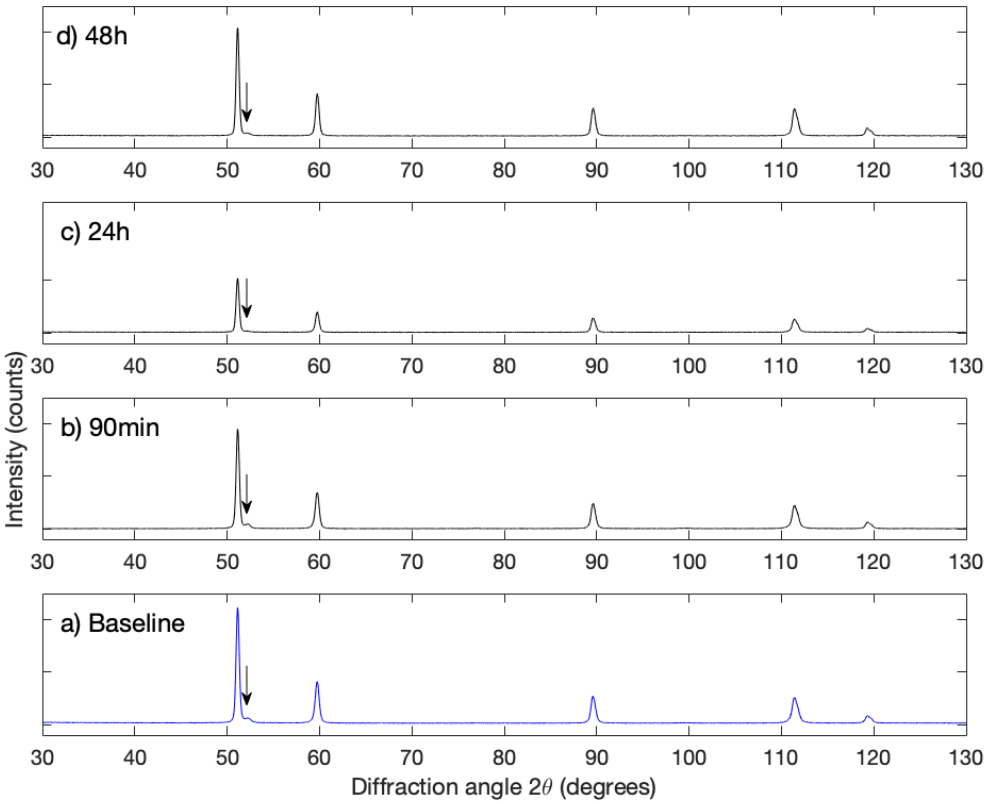

Figure 4.16: XRD patterns (sum of scans at different ψ angle form 0 to 60°) of polished-uncoated 304L after H_2 desorption for different H_2 loading times

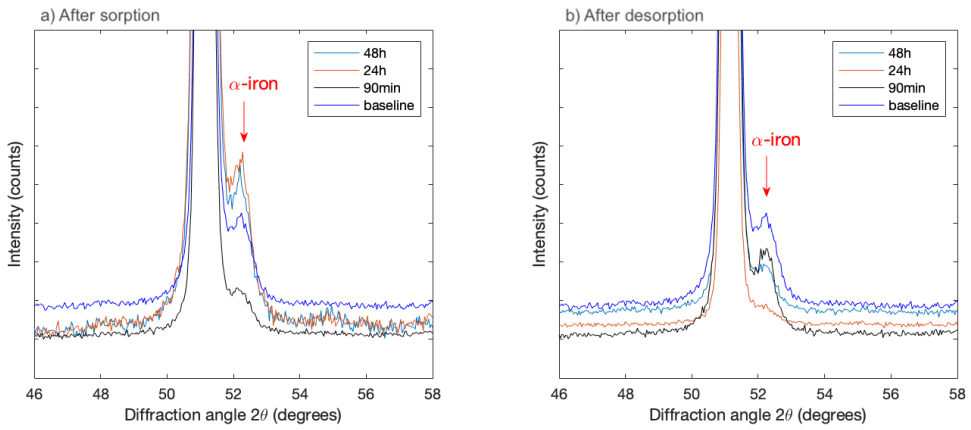

Figure 4.17: Zoom in of the peak corresponding to plane {110} in the ferritic phase of polished-uncoated 304L after H_2 (a)sorption and (b)desorption for different H_2 loading times

Table 4.4 shows a comparison of the volume fraction (specifically the austenitic phase), the residual stress, and the strain-free lattice parameter (a_0) values calculated before exposure, after sorption, and after desorption for different loading times. Additionally, an arrow (↑) indicates if an increment of the value with respect to the baseline occurred. In the case of the original state (baseline) two replicas were tested to check the reproducibility of the results.

Table 4.4: Evaluation of the change in the percentage volume fraction and strain-free lattice parameter for uncoated 304L before and after H loading

Sample	Condition	Austenite Volume Fraction		Residual Stress	a_0	
		[%]	Change vs. baseline	[MPa]	[Å]	Change vs. baseline
Baseline (Before loading)	Replica 1	95.0±1	-	-291±15	3.5907	-
	Replica 2	95.8±0.6	-	-278±15	3.5907	-
After sorption	90 min	97.6±0.4	↑	-314±13	3.5907	none
	24 h	96.6±0.5	↑	-318±17	3.5918	↑
	48 h	96.8±0.4	↑	-286±12	3.5916	↑
After desorption	90 min	95.8±0.7	none	-295±20	3.5908	none
	24 h	98.1±0.3	↑	-90±25	3.5913	↑
	48 h	97.8±0.3	↑	-109±14	3.5913	↑

A subtle increment of the lattice parameter with the loading time until 24 h is observed when the sample is analysed just after sorption. This observation can be explained by the expansion of the crystal structure due to hydrogen ingress, previously discussed in the literature (section 2.4.2). After the hydrogen desorption, the crystal structure tries to go back to its original state, the reason why the lattice parameter presents less increment after desorption than after sorption. The increment of the lattice parameter is associated with the formation of iron-hydride, as explained by Nishino et al. [75]. The $\gamma_{Hydride}$ phase is very unstable and can only be detected immediately after hydrogen charging which makes it difficult to study [15]. Both the hydrate and the matrix have the same crystal structure (austenite) so that it is not possible to differentiate one from the other by XRD analysis, except by the small increment in the lattice parameter. The author reported an increment between 0.2 to 1.2% on the lattice parameter as a consequence of the formation of iron-hydride. Nonetheless, in the present the study, the increment was only of 0.03% at the highest (after 24 h of loading).

Complementary, table 4.4 also summarises the semi-quantification of phases after different H_2 loading times. The results show that the percentage of the austenitic phase has increased in both cases after sorption and after desorption. As mentioned in the literature (section 2.4.2), hydrogen-induced martensite has been reported as the expected effect of hydrogen in metastable austenitic steels. However, the particular 304L stainless steel subjected to study has a ferritic phase besides the austenitic matrix, which was never assessed by these previous investigations. In the case of a two-phase 304L stainless steel, the compressive residual stress and the subtle increment of the strain-free lattice parameter observed in the austenitic phase are resulting from the hydrogen sorption/desorption processes could have influenced over the ferritic phase formation. Since the crystal lattice of the austenitic phase (γ-Fe) expands internally by the hydrogen ingress, the neighbours' lattices are subjected to compressive stresses that will propagate to the ferritic phase (α-Fe) as a relaxation mechanism. The result is a possible phase transformation from BCC to FCC (ferrite to austenite) under compression that is evidenced in the results as an increment of the austenite volume fraction. In addition, the increment of the austenite phase involves the densification of the material[3].

A study made by Shyvaniuk et al. also observed a similar transformation (from γ to α' phase) after gaseous hydrogenation of a metastable austenitic stainless steel occurring at low temperature (547K). Based on quantum calculations (DFT) and experiments on strained 304 L, the authors propose that hydrogen enhances the thermodynamic stability of the FCC phase with respect to that of the bcc phase. In addition, the increment of the thermodynamic equilibrium concentration of vacancies induced by hydrogen promotes an enhancement of diffusivity of the metal atoms which can be another factor to the ferrite reversion [58].

[3]An FCC lattice has four atoms per unit cell whereas BCC only two atoms

4.3.2. Lap joint weld joining coated 304L stainless steel

Initial state: before H_2 exposure

Figure 4.18 shows the XRD pattern of the as-received lap joint weld. Two phases were distinguished, an austenite phase and an oxide phase, trevorite ($NiFe_2O_4$). Trevorite is a mixture of oxides Fe_2O_3 and NiO.

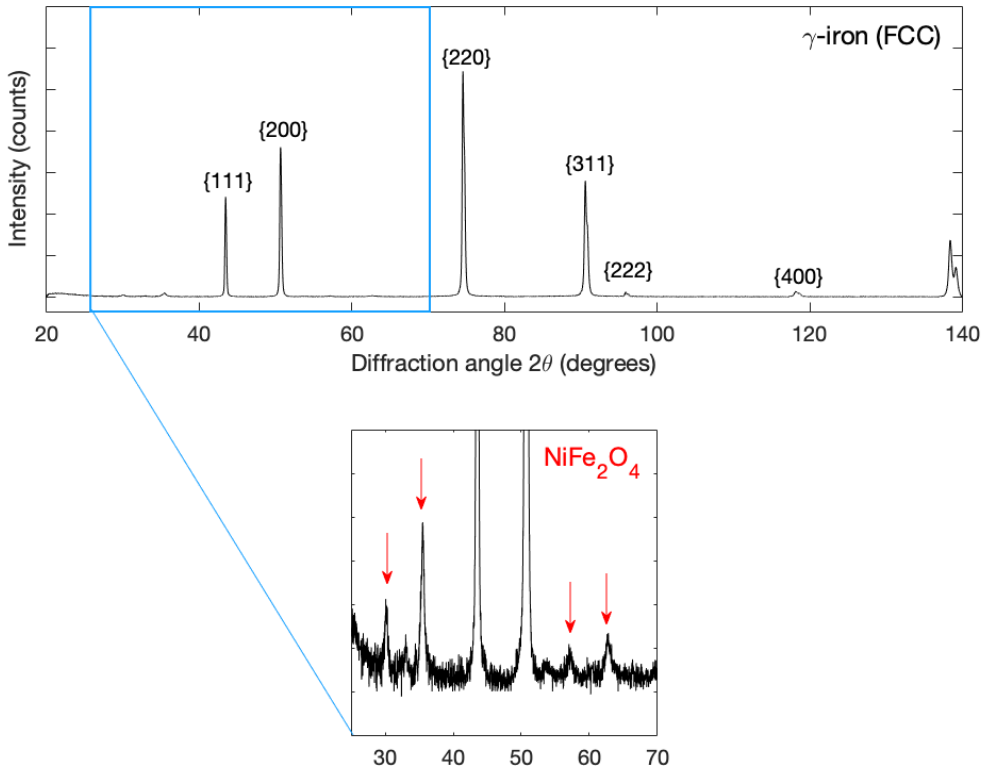

Figure 4.18: XRD pattern of lap joint of coated 304L before H_2 exposure (baseline)

After H_2 exposure

Figure 4.19 shows the XRD pattern of the lap-joint weld after desorption. It is observed that two new phases were found, one corresponding to hematite (Fe_2O_3) and the other one corresponding to a second phase of Iron-Nickel (Fe0.63Ni0.37).

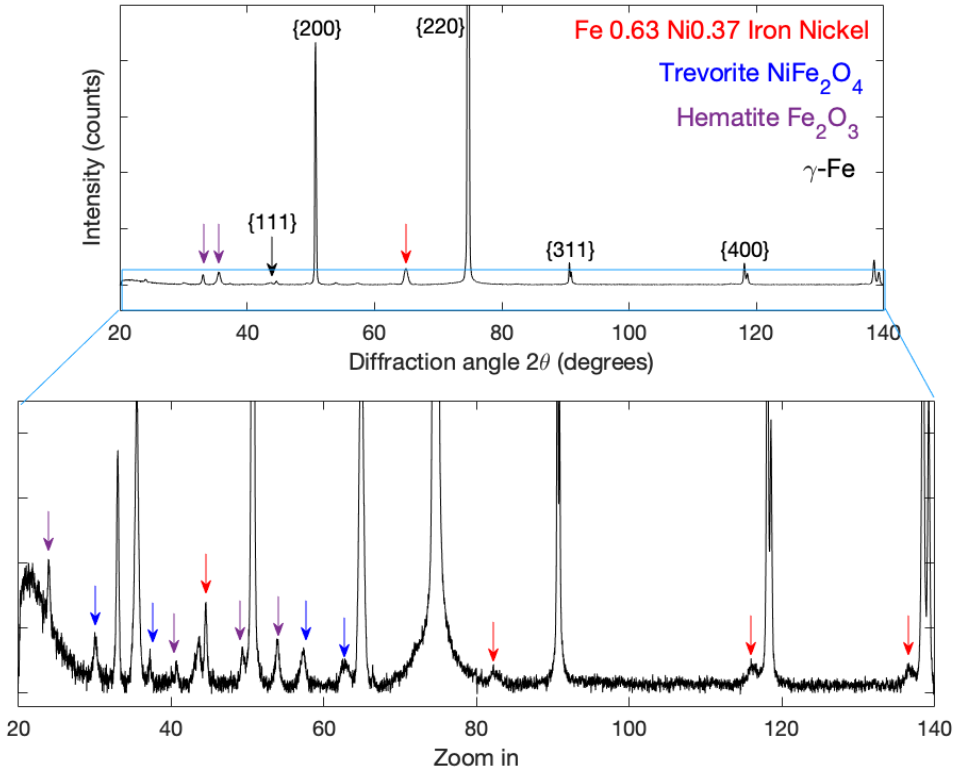

Figure 4.19: XRD pattern of lap joint of coated 304L after H_2 desorption

4.3.3. Invar

Initial state: before H_2 exposure

Figure 4.20 shows the XRD pattern of Invar alloy in its original state. The results show a single austenitic phase (γ-Fe,Ni) (table 4.5). The intensity of the peaks might be affected by texture because the sample was only tested at one tilting angle (ψ=0°). The the same applies for the evaluations after the H_2 exposure. The strain-free lattice parameter was $a_0 = 3.5938 \pm 0.0004$ Å.

Table 4.5: Invar-XRD-before

Database PDF	Phase	Crystal structure	Volume fraction [wt%]
Fe0.7Ni0.3 (Taenite)	Austenite	FCC	100%

After H_2 exposure

The XRD patterns after exposure did not present any additional peak in comparison with figure 4.20, reason why they are not presented in this section (check on Appendix B.0.1).

The parameters obtained from the residual stress measurement are presented in table 4.6. The results show that the sample is under compression in the two ϕ angles tested (0 and 90^o) which is expected by the hydrogen inside the lattice structure. On the other hand, no change in the lattice parameter was found.

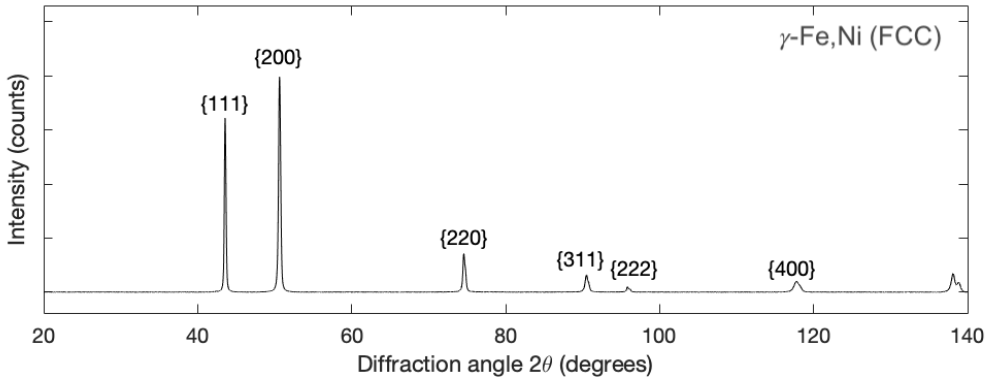

Figure 4.20: XRD pattern of polished Invar before H_2 exposure (baseline)

Table 4.6: Evaluation of the residual stress and strain-free lattice parameter for Invar before and after H_2 loading

Sample	ϕ	Residual Stress [MPa]	a_0 [Å]
Baseline (Before loading)	0 90	-112±40 -145±8	3.5938±0.0004
After sorption 90 min	0 90	-257±12 -195±36	3.5939±0.0006
After desorption 90min	0 90	-285±19 -319±44	3.5937±0.0000

4.3.4. Seam weld (resistance weld) joining Invar sheets

Initial state: before H_2 exposure

The XRD patterns corresponding to the initial state of the seam weld are presented in figure 4.21. In this case, three phases were recognised, the iron-nickel austenitic phase, hematite (Fe_2O_3) and trevorite ($NiFe_2O_4$).

AfterH_2 desorption

No new phases were found after the H_2 desorption process. However, it is possible that the volume fractions of the phases present might have changed, but no quantification was conducted. In conclusion, there were no new phases observed in both the plain Invar and the seam welds.

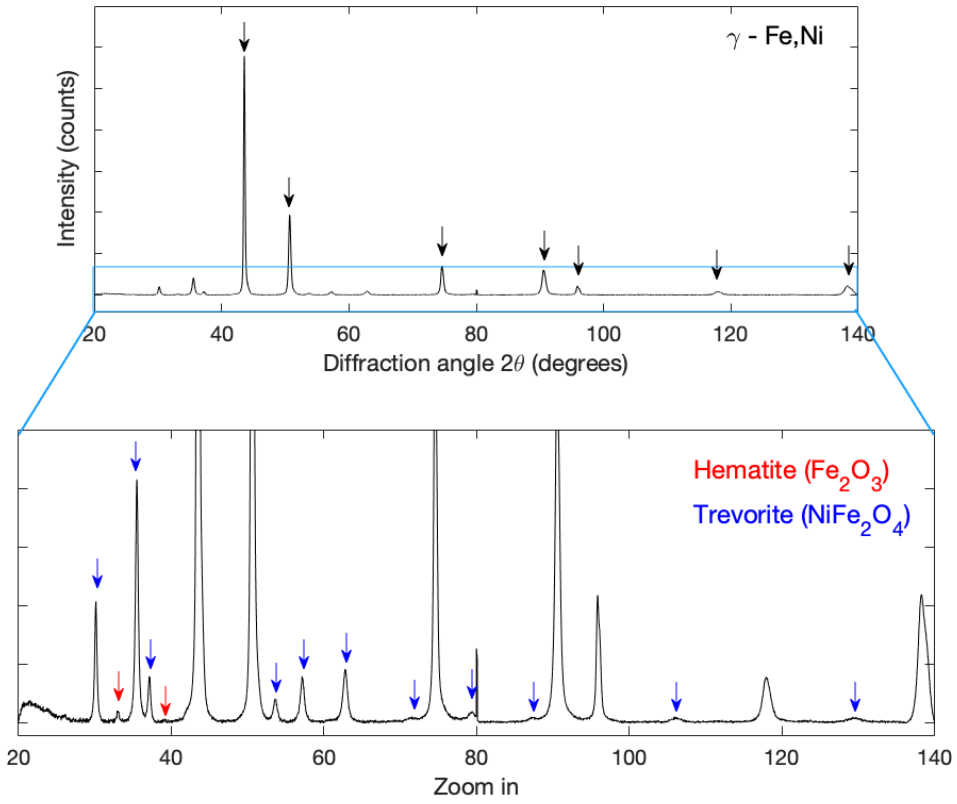

Figure 4.21: XRD pattern of seam joint of Invar before H_2 exposure (baseline)

4.4. Cyclic Voltammetry

4.4.1. Determination of potential range of study

To determine the potential range described in section 3.5, some preliminary tests were conducted. Previous studies on steel samples (on Aermet 100 [67] and on SAE 1010 [44]) suggest an initial potential (Ei) from -1,3 V vs. SCE or -1.25 V vs. SCE, respectively. As known from the literature, each type of steel is essentially a different catalyst for the HER. Consequently, the onset of HER slightly differs from the steel composition changes.

If converting the Ei mentioned above with respect to $Ag/AgCl_{sat}$ reference electrode the correspondent values are -1.25 V or -1.19 V. Therefore, several initial potentials around these values were tested out on 304L stainless steel and Invar samples as starting points.

Uncoated 304L

Figure 4.22 shows the shape of the 1st scan after H_2 loading for the different initial potentials vs.$Ag/AgCl_{sat}$ in comparison with the baseline scan (2nd scan before H_2 loading). Going from Ei=-1.20 V to Ei=-1.23 V an increment on the H_2 desorption peak is observed (the peak assignment is detailed in section 4.4.3), being the last, the one that gives a better peak resolution. Following this trend, one would expect that the peak increment continues as the initial potential of CV becomes more negative. However, this does not occur. Looking at the CV scan corresponding to Ei=-1.25 V, one sees that the H_2 desorption peak is smaller than the one generated at Ei=-1.23 V. Looking at figures 4.22 and 4.23 together, the decrement in the peak can be explained by the fact that less H_2 atoms were adsorbed as it will be explained next.

Figure 4.23 presents the chronoamperometric curves resulting from H_2 loading during 30 min for

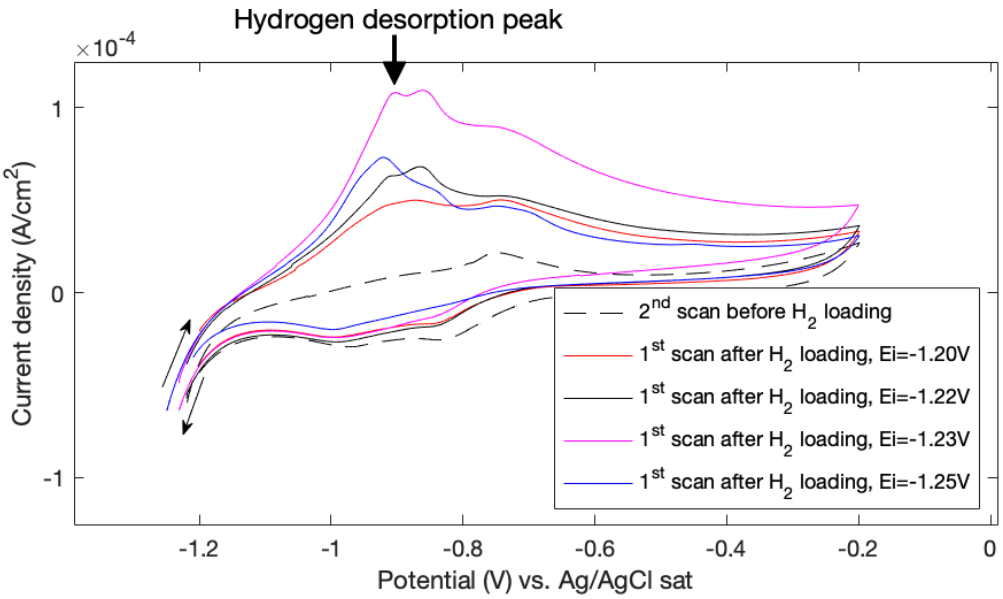

Figure 4.22: Preliminary tests on uncoated polished 304L comparing the desorption CV after H_2 loading at different initial potentials vs. the baseline CV scan before H_2 loading

each Ei. This figure shows that, as the Ei takes more negative values, the curve's shape deforms. At Ei=-1.23 V vs. $Ag/AgCl_{sat}$ there is a slightly current increment that becomes more pronounced when Ei=-1.25 V (shown in the graph as a pit). Since the electrolytic cell configuration guarantees a constant area and the potential is being kept constant during the experiment, the only reason why the current can be suddenly increasing is due to an apparent change in the active area. Meaning that not all the exposed area (physically delimited by the cell) was participating in the current flow because at more negative potentials, there is H_2 bubbles formation. If a bubble is formed on the sample surface, it acts as a shield that prevents current to flow through. When the bubble eventually pops-up, this previously covered area becomes exposed again showing an apparent "increment" in the current density.

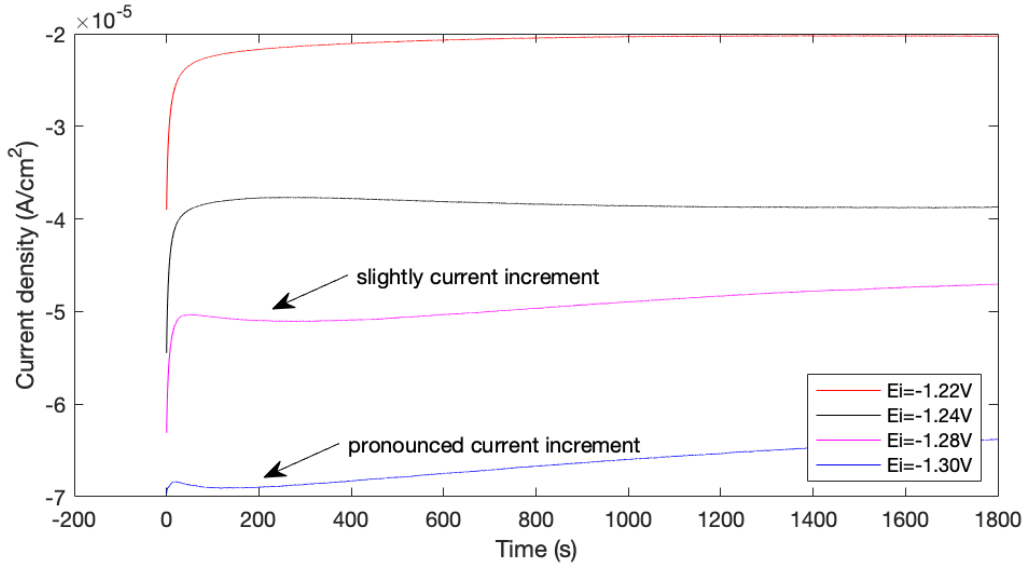

Figure 4.23: Chronoamperometric curves of polished 304L resulting from H_2 loading during 30 min for each Ei vs. $Ag/AgCl_{sat}$

Ozdirik et al. [44] remark the importance of avoiding H_2 the formation of the bubbles during the experiment. However, due to the electrolytic cell configuration used in the present experiment, it was

not possible to visually check if the H_2 bubbling was taking place. There is no visibility to the exposed area during the experiment. Therefore, the way used to determined is H_2 bubbling was taking place is by checking at the stability of the chronoamperometric curve (current vs. time).

In summary, the selection of the potential range (mostly the Ei) is a trade-off between a clear hydrogen desorption peak and a stable chronoamperometric curve. For the particular case of study 304L stainless steel, Ei=-1.22 V vs. $Ag/AgCl_{sat}$ was selected as the most negative potential in which bubbling can be avoided, and H_2 desorption peak is representative enough.

From the previous results, it is remarkable to mention the dependency existing between the potential imposed to the sample and the amount of hydrogen that is electrochemically desorbed (quantified by the area of the hydrogen desorption peak). This dependency is certainly a limitation of the experiment if the amount of hydrogen desorbed wants to be taken as a measure of adsorption. To overcome misinterpretation of the results, the quantified values (section 4.4.4) corresponding to the amount of hydrogen adsorbed/desorbed, are interpreted in terms of efficiency (as shown in section 3.5.2).

Cheng and Niu [11] reported that the dependency between the amount of absorbed hydrogen with the cathodic polarisation, during HER on steel, is only significant at very low cathodic polarisation values. Once higher cathodic polarisation (more negative values) is reached the amount of absorbed hydrogen atoms do not further increase. In the case of the present project, low cathodic polarisation is required since the aim is promoting the hydrogen atoms to adsorb into the metal (Volmer step) not generating hydrogen gas (Heyrovsky or Tafel steps).

Invar

For Invar, the same analysis was conducted but starting from the selected initial potential for 304L, to have some comparison point. However, as shown in figure 4.24, there is no H_2 desorption peak showing when starting the CV at Ei=-1.22 V as happened with 304L. If Ei becomes more negative, at Ei=1.28 V a defined H_2 desorption peak starts to show. Nevertheless, a slightly more negative value, Ei=-1.30 V vs. $Ag/AgCl_{sat}$, was selected to facilitate the later quantification of this peak.

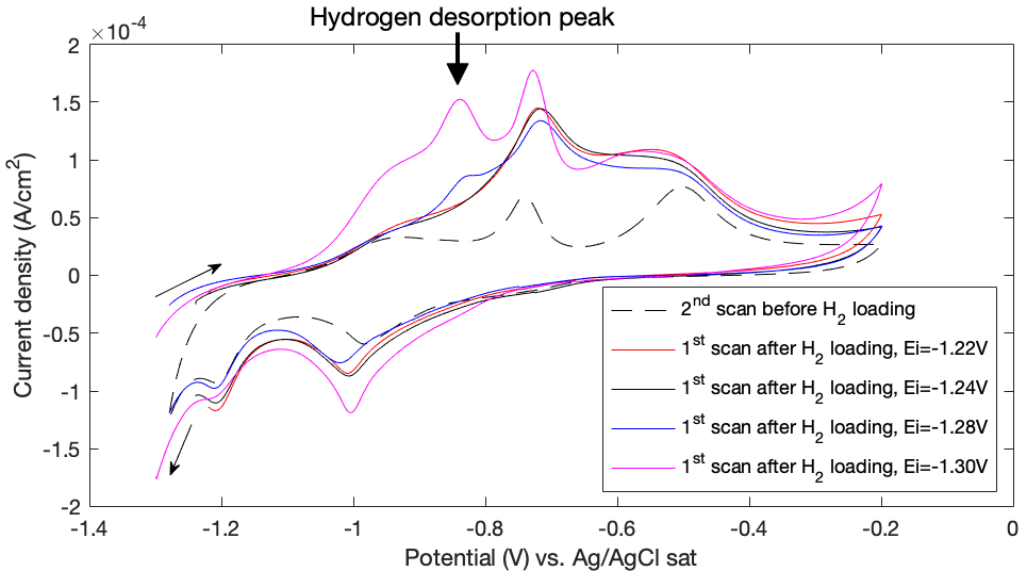

Figure 4.24: Preliminary tests on polished Invar comparing the desorption CV after H_2 loading at different initial potentials vs. the baseline CV scan before H_2 loading

If following the same reasoning that for 304L, it is interesting to take a look into how the chronoamperometric curves looked for Invar. Figure 4.25 shows that all the curves kept stable (no dips) during the loading time, meaning that there was no remarkable H_2 bubbling in any of the different Ei tested. Therefore, the decision of the initial potential was only related to the height of the H_2 desorption peak in this particular case.

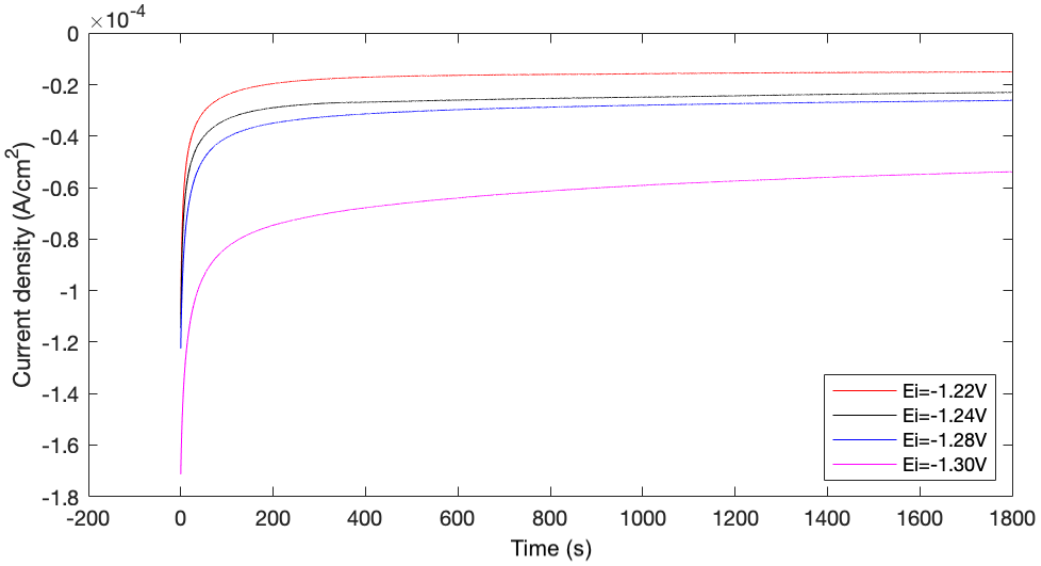

Figure 4.25: Chronoamperometric curves of polished Invar resulting from H_2 loading during 30 min for each Ei vs. $Ag/AgCl_{sat}$

4.4.2. Pourbaix Diagram for understanding Redox process during CV

A Pourbaix diagram is a really handy tool to do the peak assignment of the cyclic voltammograms of each correspondent material. For this purpose, both hydrogen and the metal catalyst diagrams need to be analysed in the corresponding region of interest.

Uncoated 304L

Figure 4.26 shows the Pourbaix diagram of a Fe(72%)-Cr(19%)-Ni(9%) alloy resembling the composition ratio (in weight) of 304L steel if no other alloying elements were present. Iron, chromium and nickel were taken into consideration because they represent the higher percentage in weight among all the elements present in table 4.1.

For the understanding the electrochemical processes alongside the potential range studied (-1.25 V to -0.2 V vs. $Ag/AgCl_{(sat-KCl)}$), which is delimited by the dark-turquoise shaded region on the graph, it is necessary to take a look into all the stable chemical species coexisting. The points (a to f) correspond to the different regions distinguished at pH=13.45[4] along the potential range region. The chemical species associated with each region are detailed in table 4.7.

The dash-line (**LLW**) corresponds to the lower limit of water stability, below which the liberation of hydrogen starts. The thermodynamic onset of HER is marked (around -0.99 V vs. $Ag/AgCl_{(sat-KCl)}$). Nonetheless, an overpotential needs to be considered for the reaction to occur experimentally due to intrinsic resistances of the electrolytic cell as well as the activation overpotential required for the hydrogen evolution on the specific electrode material (-0.15 V for the case of iron).

Table 4.8 shows in detail the oxidation number of each metallic element in the different compounds listed in table 4.7. By analysing element by element from one region to the next one, it is easy to predict and oxidation or reduction process. In this regard, table 4.9 summarises the oxidation processes and the standard potentials E^o of each redox reaction happening at pH=13.45.

The potential is derived from figure 4.26 by simply finding the intersection point between the working pH (red vertical line at pH=13.45, for example) and the limiting lines of each region in the potential range studied (sloped lines corresponding to electron transfer reactions or “redox”) and then reading the corresponding potential value (showed as purple dot-lines pointing left in the graph).

[4]pH selected between the pH range to exemplify the method

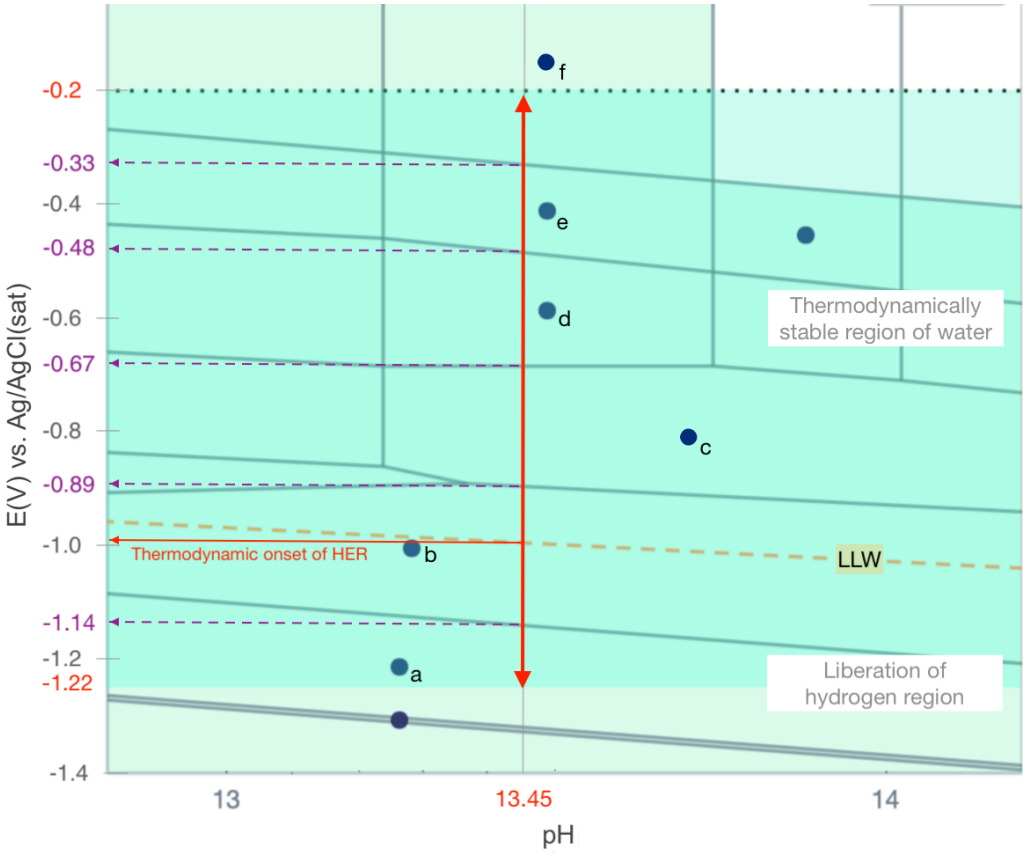

Figure 4.26: Pourbaix diagram of Fe(72%)-Cr(19%)-Ni(9%) in the pH range from 13 to 14 [26, 49]. The potential is referred to $Ag/AgCl_{(sat-KCl)}$. The regions of stability are indicated by 'a' to 'f' and the corresponding compounds are given in table 4.7

It is important to consider that the standard potential E^o values read from 4.26 should be interpreted with some degree of flexibility. This has to do with the fact that the pH of the electrolyte solution may slightly vary from one experiment to another (13.40 < pH < 13.6) due to human error in the mass weighting during solution preparation. Therefore the E^o also varies in a short-range according to the sloped boundary lines of each region. This is the reason why it is preferable to report a range, rather than a specific value, in which the E^o is more likely to occur. Table 4.8 compiles the information regarding the redox reactions happening at the uncoated 304L surface. It is remarkable that some elements oxidises in two stages like for example iron oxidation from Fe(II) into Fe(III) happens first in redox reaction #3 and later again in redox reaction #5. This is happening because the elements subjected to redox reactions are part of more than one compound due to the complexity of the alloy.

The theoretical prediction of the Fe_2NiO_4 coincides with the oxide found by XRD in the lap-joint weld sample as described in section 4.3.2. The lap-joint weld can be taken as the oxidised state of the 304L plain material.

Table 4.7: Stable compounds in each region of the Fe-Ni-Cr Pourbaix diagram (Figure 4.26) [26, 49]

Region	Compounds		
a	$FeNi_{3(s)}$	+ $Cr_2FeO_{4(s)}$	+ $HFeO_2^-$
b	$Ni_{(s)}$	+ $Cr_2FeO_{4(s)}$	+ $HFeO_2^-$
c	$Ni_{(s)}$	+ $Cr_2FeO_{4(s)}$	+ FeO_2^-
d	$Fe_2NiO_{4(s)}$	+ $Cr_2FeO_{4(s)}$	+ FeO_2^-
e	$Fe_2NiO_{4(s)}$	+ $Cr_2O_{3(s)}$	+ FeO_2^-
f	$Fe_2NiO_{4(s)}$	+ CrO_4^{2-}	+ FeO_2^-

Table 4.8: Oxidation number of each metallic element in the different compounds listed in table 4.7

Compund	Oxidation number		
	Fe	Cr	Ni
$FeNi_{3(s)}$	0		0
$Cr_2FeO_{4(s)}$	+2	+3	0
$HFeO_2^-$	+2		
$Ni_{(s)}$			0
FeO_2^-	+3		
$Fe_2NiO_{4(s)}$	+3		+2
$Cr_2O_{3(s)}$		+3	
CrO_4^{2-}		+6	

Table 4.9: Theoretical potential of redox reactions (vs. $Ag/AgCl_{(sat-KCl)}$) according to figure 4.26 within the working pH range.

#	Regions	Compounds	Redox reaction	Potential range [V]
1	a $\rightleftharpoons$ b	$FeNi_{3(s)} \rightleftharpoons Cr_2FeO_{4(s)}$	Fe(0) $\rightleftharpoons$ Fe(II)	-1.13 to -1.16
	Onset of HER	**$2\,H_2O_{(l)} + 2\,e^- \rightleftharpoons 2\,OH^- + H_{2(g)}$**		**-0.99 to -1.10**
2	b $\rightleftharpoons$ c	$HFeO_2^- \rightleftharpoons FeO_2^-$	Fe(II) $\rightleftharpoons$ Fe(III)	-0.89 to -0.91
3	c $\rightleftharpoons$ d	$Ni_{(s)} \rightleftharpoons Fe_2NiO_{4(s)}$	Ni(0) $\rightleftharpoons$ Ni(II)	-0.67 to -0.70
4	d $\rightleftharpoons$ e	$Cr_2FeO_{4(s)} \rightleftharpoons Fe_2NiO_{4(s)}$	Fe(II) $\rightleftharpoons$ Fe(III)	-0.48 to -0.50
5	e $\rightleftharpoons$ f	$Cr_2O_{3(s)} \rightleftharpoons CrO_4^{2-}$	Cr(III) $\rightleftharpoons$ Cr(VI)	-0.33 to -0.35

Invar

The same analysis previously done for uncoated 304L was conducted for Invar, Fe(64%)-Ni(36%) alloy, resulting in figure 4.27. Since the initial potential for Invar is slightly more negative than for 304L and the composition ratio of Fe: Ni also changes, there are some regions of the Pourbaix diagram that get included in the analysis. Like regions 'a' and 'e' that were out the pH region of interest for 304L.

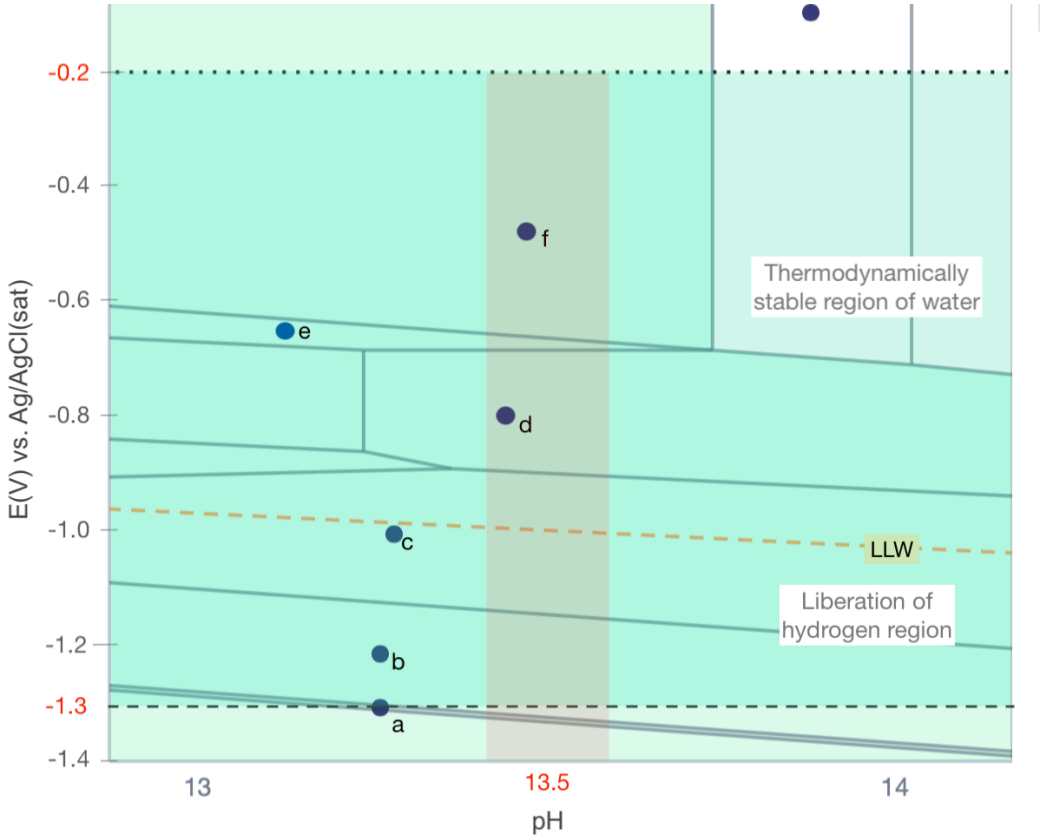

Figure 4.27: Pourbaix diagram of Fe(64%)-Ni(36%) alloy in the pH range from 13 to 14 [49]. The potential is referred to $Ag/AgCl_{(sat-KCl)}$. The regions of stability are indicated by 'a' to 'f' and the corresponding compounds are given in table 4.10

Once, both the regions and the pH range of study were determined, it was possible to obtain table 4.10 were all the possible, stable compounds are detailed. Complementary, table 4.11 details the oxidation number of each element of the components previously described.

Table 4.10: Stable compounds in each region of the Fe-Ni Pourbaix diagram (Figure 4.27) [26, 49]

Region	Compound	
a	$FeNi_{(s)}$	+ $HFeO_2^-$
b	$FeNi_{3(s)}$	+ $HFeO_2^-$
c	$Ni_{(s)}$	+ $HFeO_2^-$
d	$Ni_{(s)}$	+ FeO_2^-
e	$Ni_{(s)}$	+ $Fe_2NiO_{4(s)}$
f	$Ni(OH)_3^-$	+ $Fe_2NiO_{4(s)}$

Further on, it was possible to determine the possible reactions associated with the changes in oxidation number for each metal. Table 4.12 compiles all this information. Again, it is remarkable that both iron and nickel oxidise in two stages. Iron goes from Fe(0) to Fe(II) in reactions #1 and #2, while nickel goes from Ni(0) to Ni(II) in reactions #4 and #5.

Table 4.11: Oxidation number of each metallic element in the different compounds listed in table 4.10

Compund	Oxidation number	
	Fe	Ni
$FeNi_{(s)}$	0	0
$FeNi_{3(s)}$	0	0
$HFeO_2^-$	+2	
$Ni_{(s)}$		0
FeO_2^-	+3	
$Fe_2NiO_{4(s)}$	+3	+2
$Ni(OH)_3^-$		+2

The compounds Fe_2NiO_4 and FeO_2^- (that comes from Fe_2O_3) coincide with the oxides found by XRD in the seam weld sample as described in section 4.3.4. The seam weld can be taken as the oxidised state of the Invar plain material.

Table 4.12: Theoretical potential of redox reactions (vs. $Ag/AgCl_{(sat-KCl)}$) according to figure 4.27 within the working pH range.

#	Regions	Compounds	Redox reaction	Potential range [V]
1	a $\rightleftharpoons$ b	$FeNi_{(s)} \rightleftharpoons HFeO_2^-$	Fe(0) $\rightleftharpoons$ Fe(II)	-1.32 to -1.34
2	b $\rightleftharpoons$ c	$FeNi_{3(s)} \rightleftharpoons HFeO_2^-$	Fe(0) $\rightleftharpoons$ Fe(II)	-1.14 to -1.16
	Onset of HER	$\mathbf{2\,H_2O_{(l)} + 2\,e^- \rightleftharpoons 2\,OH^- + H_{2(g)}}$		**-0.98 to -1.20**
3	c $\rightleftharpoons$ d	$HFeO_2^- \rightleftharpoons FeO_2^-$	Fe(II) $\rightleftharpoons$ Fe(III)	-0.89 to -0.91
4	d $\rightleftharpoons$ e	$Ni_{(s)} \rightleftharpoons Fe_2NiO_{4(s)}$	Ni(0) $\longrightarrow$ Ni(II)	-0.68 to -0.69
5	e $\rightleftharpoons$ f	$Ni_{(s)} \rightleftharpoons Ni(OH)_3^-$	Ni(0) $\rightleftharpoons$ Ni(II)	-0.65 to -0.66

4.4.3. Peak assignment

Once the theoretical E^o for the redox processes and the HER have been positioned along with the potential range of study for each material, uncoated 304L and Invar, the peak assignment consisted on correlating the theoretical values of E^o with the Ep of the peaks found on the cyclic voltammograms. To facilitate the peak identification, it was assumed that there is no H_2 sorption (consequently no H_2 desorption peak either) before the H_2 loading[5]. Therefore, the **2nd CV scan before H_2 loading** for all samples becomes the **baseline** so that any later comparison or calculation will refer to it.

It is important to mention that a very small amount of hydrogen is probably being adsorbed into the material when the potential is in the region close to the Ei. Uluc [67] proposes certain equations to evaluate the amount of hydrogen involved in the first and second scan before H_2 loading. Nevertheless, this amount is so small that it does not generate a hydrogen desorption peak on the CV scans before H_2 loading.

Uncoated 304L

Figure 4.28 shows the typical shape of a CV corresponding to the 2nd scan before H_2 loading for a polished uncoated 304L samples. The nomenclature used for the peaks intends to show the correlation some peaks may have between each other. The capital letter indicates a redox couple meaning that the two peaks correspond to the same redox process. On the other hand, the number refers to the branch to which the peak belongs (**1 for anodic** and **2 for cathodic**).

The association of two peaks to the same redox process was only based on the visual correlation of the peaks displaying almost similar i_{pa} and i_{pc}[6]. Since the current peaks (cathodic and anodic) of the

[5]This assumption is valid considering that the time at which the sample is kept at the hydrogen evolution potential is instantaneous.

[6]In reversible redox systems the ratio $i_{pa}/i_{pc} = 1$, whereas in quasi-reversible and irreversible reactions the ratio $i_{pa}/i_{pc} \neq 1$.

Table 4.13: Experimental standard peak potential vs. Ag/AgCl$_{(sat-KCl)}$ of the peaks before and after H_2 exposure for uncoated polished 304L (read from figures 4.28 and 4.29)

Condition	Before			After		
Couple	Potential [V]					
peak	E_{pa}	E_{pc}	E^o	E_{pa}	E_{pc}	E^o
A	-0.8870	-0.9702	-0.9286	-0.8670	-0.9882	-0.9276
B	-0.7487	-0.8382	-0.7935	-0.7437	-0.8441	-0.7939

Table 4.14: Comparison of experimental vs. theoretical standard potential value vs. Ag/AgCl$_{(sat-KCl)}$ for peaks of uncoated polished 304L

Peak couple	E^o [V]		Redox Reaction Associated
	Experimental value	Theoretical range	
A	-0.93	-0.89 to -0.91	Fe(II) $\rightleftharpoons$ Fe(III)
B	-0.79	-0.67 to -0.70	Ni(0) $\rightleftharpoons$ Ni(II)

redox reactions paired together is clearly not the same, it is most likely that they correspond to quasi-reversible systems. There is also the possibility that a monolayer or submonolayer impurities caused the hysteresis observed between the cathodic and anodic branches [27]. The study of the reversibility of the redox couples is out of the scope of this project.

The same considerations were made over the analysis of all samples.
The values of the peak potentials Ep indicated in 4.28 and the calculated standard potentials (E^o) are detailed in table 4.13. Equation 4.1 is used to calculate the E^o.

$$E^o = \frac{E_{pc} + E_{pa}}{2} \tag{4.1}$$

Further on, E^o is compared with the theoretical values from table 4.9 to determine to which redox reaction each peak is related to, as shown in table 4.14. As mentioned earlier, the peaks are not exactly at the predicted theoretical potential range because the experimental set up itself adds some resistance, plus there is some over-potential associated with each working electrode. Nonetheless, the order in which the peaks appear is already a good clue to correlate what peak most likely corresponds to which redox process.

The forward swept starts from Ei=-1.22 V vs.Ag/AgCl$_{(sat-KCl)}$ showing peak A1 followed by peak B2 on the anodic brach (oxidation process). On the contrary the reverse swept starts at $E1$=-0.2 V vs.Ag/AgCl$_{(sat-KCl)}$ showing peak B2 followed by peak A2 on the cathodic brach (reduction process). Couple A is attributed to redox reaction of iron (Fe(II) →Fe(III)) whereas peak B1 is attributed to the redox reaction of nickel (Ni(0) →Ni(II)).

The shift on Ep between anodic and cathodic branches of a redox couple has to deal with the mass transport effect throughout the diffusion layer. This behaviour is characteristic of cyclic voltammetry and gives the so-called “duck shape” previously mentioned in literature.

Figure 4.29 shows how the cyclic voltammogram changes from the baseline (figure 4.28) after 30 min of H_2 loading. When identifying the peaks, it is clear that the redox couples A and B remained about the same potential as before the H_2 loading. However, there is a new peak on the anodic branch, peak C1 ($Ep = -0.9057$ V vs.Ag/AgCl$_{(sat-KCl)}$), that is associated with the oxidation of hydrogen. Specifically, peak C1 corresponds to the desorption of hydrogen. The peak assignment of hydrogen and iron coincides with the one presented by Strehblow et al. in the analysis of passivity of iron in alkaline conditions [62]. The hydrogen sorption occurs during the chronoamperometry technique while the hydrogen desorption in the 1st CV scan after the H_2 loading. The hydrogen desorption peak arises from the gas formation when atomic hydrogen recombines into a diatomic molecule and is released from the sample surface.

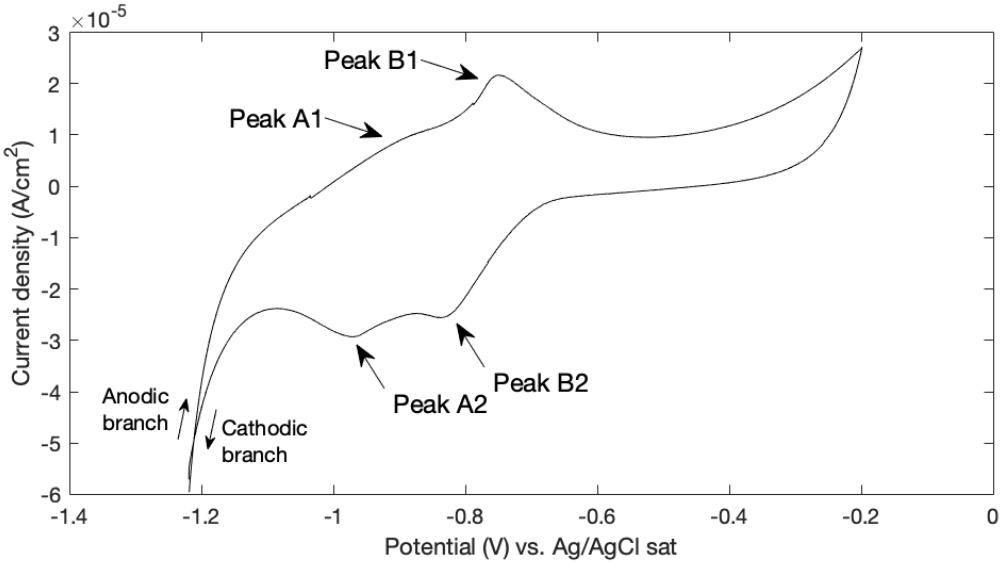

Figure 4.28: 2nd CV scan before H_2 loading for polished-uncoated 304L (sample: 304L-P-S2) indicating the identified peaks

Now, it becomes interesting to check if the sample goes back to each original state after desorption has happened. For which, the three consecutive CV scans after desorption were plotted. As depicted in figure 4.30, from the 2nd CV scan after H_2 loading onwards peak C1 disappears and the shape of the cyclic voltammograms resembles the one exhibited before the H_2 loading. On the one hand, this behaviour demonstrates that there is H_2 sorption-desorption process is occurring. But on the other hand, it is also evident that the final state of the sample (4th scan after H_2 loading) is not exactly the same as the original state of the sample (1st scan before H_2 loading). Even though the present peaks are the same, the Ep values are a bit shifted to the left (more evidently in the cathodic branch). From this observation, it can be inferred that either the chemical, the microstructural or both states of the sample are irreversibly changed after the electrochemically induced hydrogen sorption/desorption process.

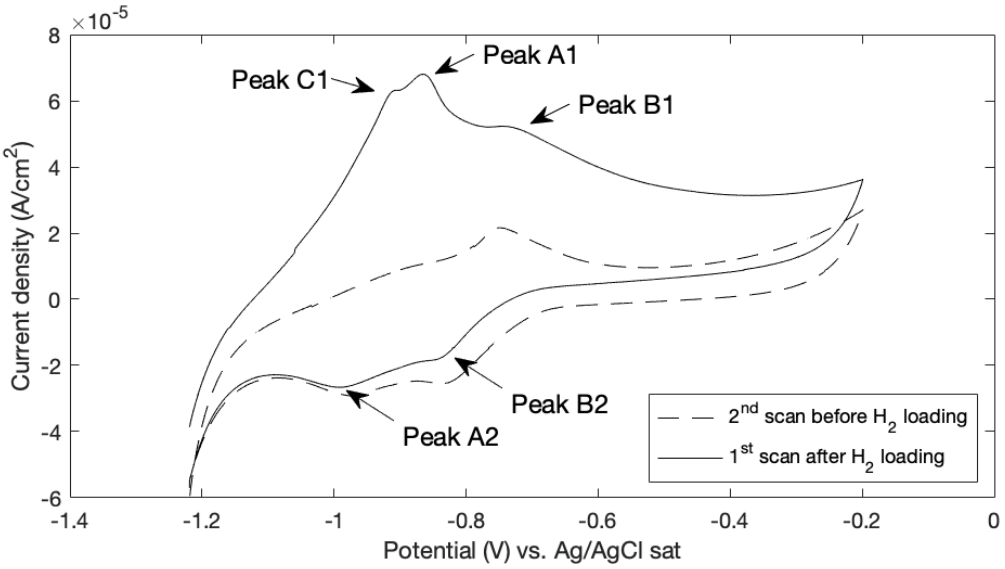

Figure 4.29: 1st CV scans after 30 min of H_2 loading for polished-uncoated 304L (sample: 304L-P-S2) indicating the identified peaks

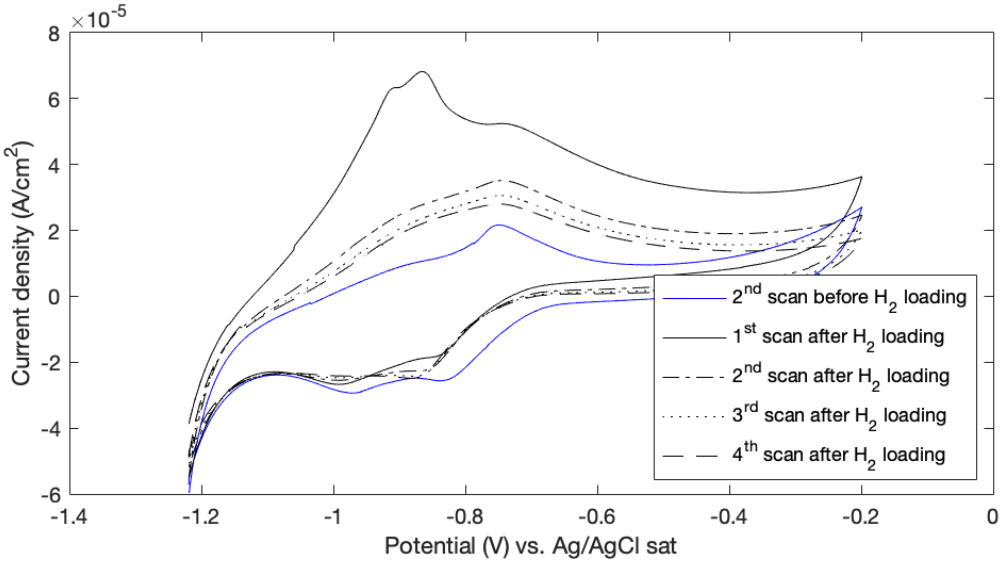

Figure 4.30: Consecutive four CV scans after 30 min of H_2 loading in comparison with 2nd scan before H_2 loading for polished-uncoated 304L (sample: 304L-P-S2)

304L coated with TiO2

Additionally, as pointed out in section 3.1. The as-received 304L stainless steel has a TiO2 coating on top. This implies that the interaction with hydrogen will be different from the one obtained if the steel would be exposed directly. Therefore an independent analysis on the coated surface was required.

Figure 4.31 shows the 2nd CV scan after cleaning scan for the as-received 304L (coated with TiO2). There is a possible redox couple named A, and a small peak B1 in the anodic branch. However, the assignment of these peaks was not conducted. Pourbaix diagrams are only available for pure metals or mixtures of them. In this case, the coating is an oxide for which no Pourbaix diagram is available.

Nevertheless, when analysing figure 4.32, one sees that after 30 min of H_2 loading the peaks associated to TiO_2 itself (redox couple A and peak B1) remain the same. One new peak is clearly identified and is located around the E^o at which hydrogen desorption was previously identifies for bare 304L. In this regard, there is no place for the confusion that peak C1 correspond to the hydrogen desorption peak.

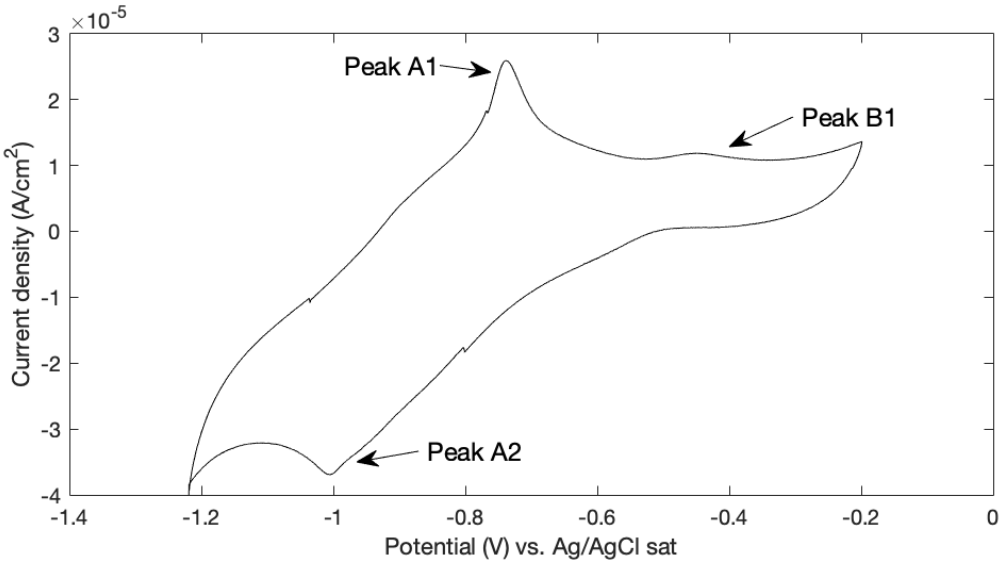

Figure 4.31: 2nd CV scan before H_2 loading for coated 304L (sample: 304L-TiO2-S3) indicating the identified peaks

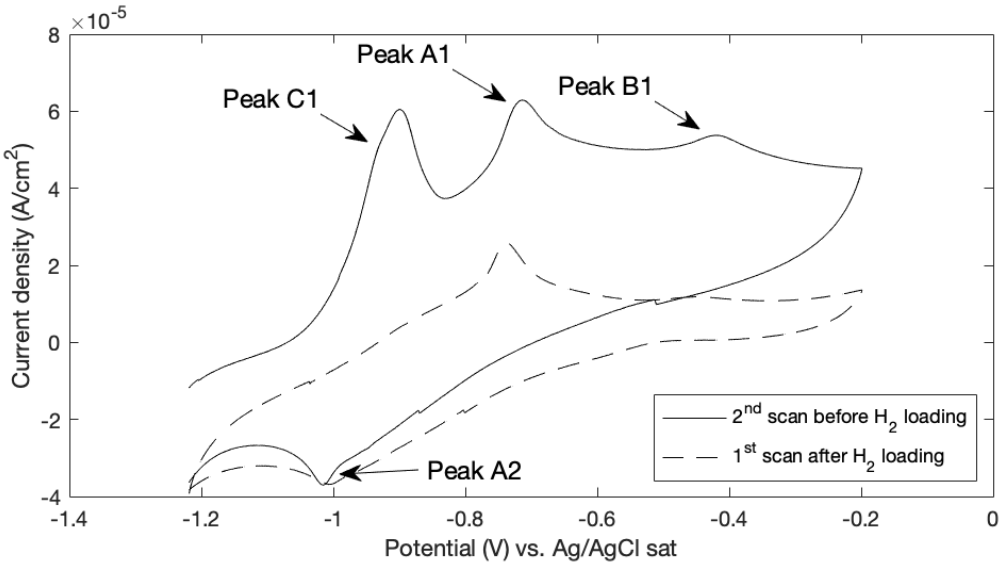

Figure 4.32: 1st CV scan after 30 min of H_2 loading for coated 304L (sample: 304L-TiO2-S3) indicating the identified peaks

Lap joint of 304L stainless steel

A lap joint weld is attaching the 304L sheets together. Figure 4.33 shows how the cyclic voltammogram of such a lap joint weld looks like before H_2 exposure. Only one redox couple is observed (couple A). Figure 4.34 shows the 2nd CV scan after 30 min of H_2 loading for the lap-joint of 304L. A new peak

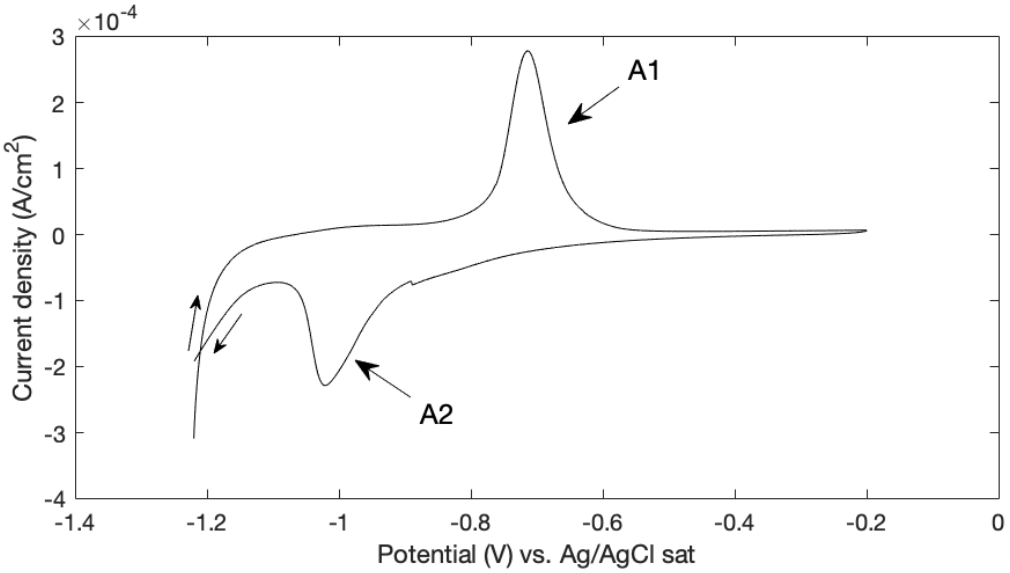

Figure 4.33: 2nd CV scan before H_2 loading for the lap joint of 304L indicating the identified peaks

is clearly shown after the H_2 exposure (peak B) which is associated with hydrogen desorption. It is interesting to point out in this cyclic voltammogram that the capacitive current effect is less than for coated and uncoated 304L.

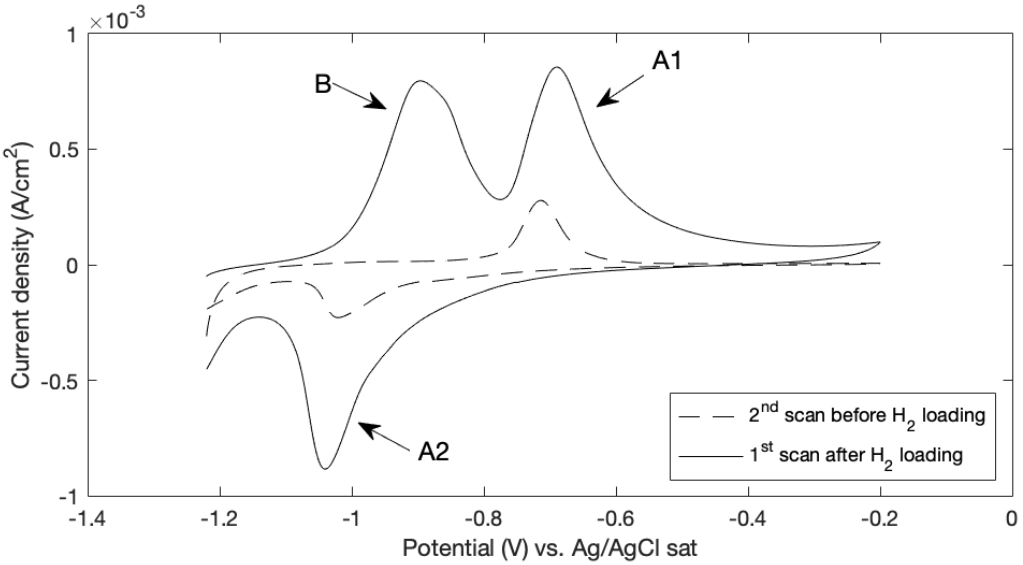

Figure 4.34: 1st CV scan after 30 min of H_2 loading for the lap joint of 304L indicating the identified peaks

Invar

The Invar sample becomes a nice comparison with the 304L stainless steel in the way that it allows to visualise how the chemical composition affects the peaks that are shown in the cyclic voltammograms. The Invar alloy contains up to 36% of Ni in comparison with the 9% present in 304L. This nickel increment is enough to show extra redox couples in comparison with uncoated 304L. Also, the Ei used for this alloy ($Ei = -1.30$ V vs. Ag/$AgCl_{(sat-KCl)}$) was slightly more negative than the used for 304L ($Ei = -1.22$ V vs. Ag/$AgCl_{(sat-KCl)}$) which increased the range and possibility of other redox processes to take place. The peaks shown in figures 4.35 and 4.36 are detailed in table 4.15. Couple A associated with Fe oxidation from Fe(0) to Fe(II) is new. Same as for couple D which is associated with the second stage of Ni oxidation from Ni(0) to Ni(II) according to table 4.11.

The remaining redox couples, B and C, are again related to iron and nickel oxidation (same as for 304L) with the only difference that they are not shown at the exact same potential. However, this was already predicted theoretically from the Pourbaix diagram.

In the same way, figure 4.36 shows a change with respect to the baseline cyclic voltammogram after 30 min of H_2 loading. All the previously discussed peaks are still present, in some cases with a slight shift. In addition to them, a new peak, named peak E1 appears. Peak E1 ($Ep = 0.8567$ V vs. Ag/$AgCl_{(sat-KCl)}$) corresponds to the hydrogen desorption peak.

It is important to report that it was observed that the baseline sometimes might slightly differ from figure 4.35. In some cases, the redox couples C and D appear to be combined as only one peak in a potential located in between. This effect might be because the surface state of the sample is not

Table 4.15: Experimental standard peak potential vs. Ag/$AgCl_{(sat-KCl)}$ of the peaks before and after H_2 exposure for polished Invar (read from figures 4.35 and 4.36)

Condition	Before			After		
Couple	Potential [V]					
peak	E_{pa}	E_{pc}	E^o	E_{pa}	E_{pc}	E^o
A	-0.9429	-1.1990	-1.0710	-0.9387	-1.1950	-1.0669
B	-0.7349	-0.9908	-0.8629	-0.7406	-0.9981	-0.8694
C	-0.6319	-0.9518	-0.7919	-0.6106	-0.9558	-0.7832
D	-0.5018	-0.5804	-0.5411	-0.4886	-0.5823	-0.5355

Table 4.16: Comparison of experimental vs. theoretical standard potential value for peaks of polished Invar

Peak couple	E^o		Redox Reaction Associated
	Experimental value	Theoretical range	
A	-1.07	-1.14 to -1.16	Fe(0) $\rightleftharpoons$ Fe(II)
B	-0.86	-0.89 to -0.91	Fe(II) $\rightleftharpoons$ Fe(III)
C	-0.79	-0.68 to -0.69	Ni(0) $\rightleftharpoons$ Ni(II)
D	-0.54	-0.65 to -0.66	Ni(0) $\rightleftharpoons$ Ni(II)

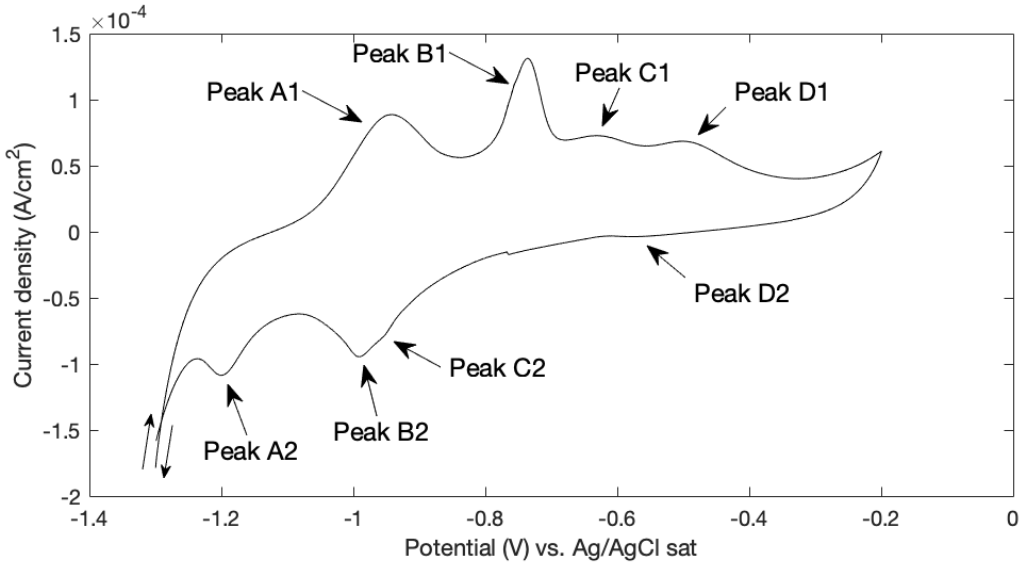

Figure 4.35: 2nd CV scan before H_2 loading for polished Invar (sample: Invar-P-S1) indicating the identified peaks

always easily reproducible due to the complexity associated with the oxide layers. An example of such a baseline is replica Invar-P-30min-S2 presented in Appendix A.3.1.

Figure 4.37 shows how the final state of the sample after four consecutive scans changes from the baseline. The most evident difference is related with the redox couple B. These peaks get enlarged in every cycle after 30 min of H_2 loading, being the 4th cycle the one in which the peaks have reached its maximum height. If a comparison is made with 304L (figure 4.30), this peak enlargement is not observed after 30 min of H_2 exposure. This makes a lot of sense considering that 304L is stainless steel that contains around 18% of chromium. Chromium generates a passive layer of chromium oxide on the surface of the 304L stainless steel samples and therefore protect the steel from oxidation. Conversely, Invar contains only 0.05% of Cr which make it more susceptible to oxidation after hydrogen exposure.

The enlargement of redox iron peaks helps to explain the change in colour in the exposed area, as observed in figure 4.9. The brown circle is then iron oxide formed as a consequence of hydrogen sorption/desorption process.

It is also interesting to point out that the oxide layer becomes more pronounced (maybe thicker) once the hydrogen is desorbed from the sample. This result may arise from the fact that the sample goes through two stages of chemical vulnerability. The first one during sorption when the H-metal bond (explained in section 2.5.1) is formed, and the second when these bonds are broken to let atomic hydrogen be released from the surface. Then the metal is available to bond, and there is a chance that the bonding occurs with oxygen (competitive adsorbent) leading the oxide formation.

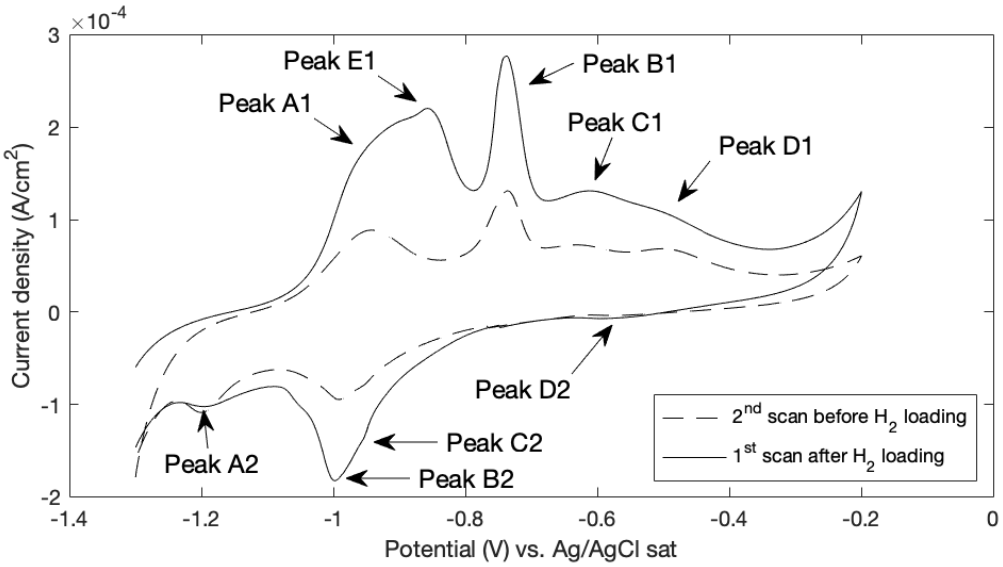

Figure 4.36: 1st CV scan after 30 min of H_2 loading for polished Invar (sample: Invar-P-S1) indicating the identified peaks

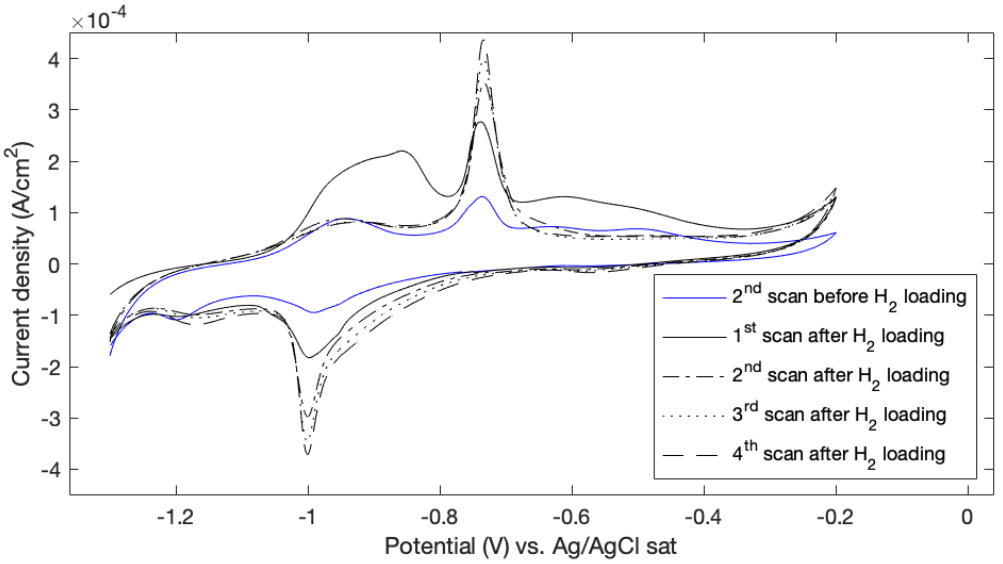

Figure 4.37: Consecutive four CV scans after 30 min of H_2 loading in comparison with 2nd scan before H_2 loading for polished Invar (sample: Invar-P-S1)

Invar's seam weld

Figure 4.38 shows the cyclic voltammogram of the seam weld of Invar before H_2 exposure. One redox couple is clearly recognised. Next, figure 4.39 shows the 2nd CV scan after 30 min of H_2 loading for

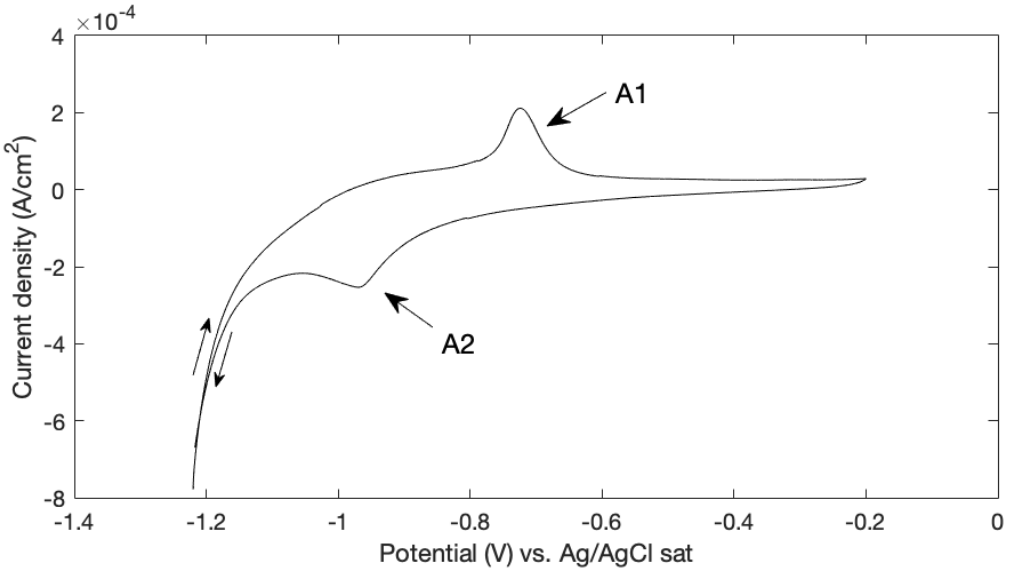

Figure 4.38: 2nd CV scan before H_2 loading for the seam weld of Invar indicating the identified peaks

the seam weld. A new peak is clearly shown after the H_2 exposure (peak B) which is associated with hydrogen desorption.

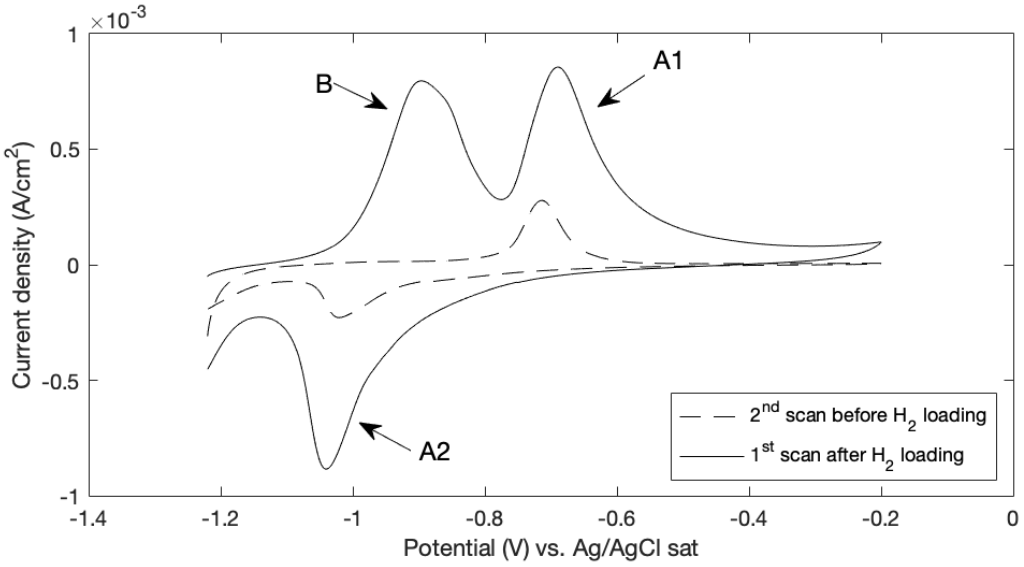

Figure 4.39: 1st CV scan after 30 min of H_2 loading for the seam weld of Invar indicating the identified peaks

4.4.4. Influence of H_2 loading time on the adsorption

Uncoated 304L

Figure 4.40 shows how the hydrogen desorption peak (the first peak from the left in the region of interest (corresponding to peak C1 in figure 4.29) considerably increases with the increment of H_2 loading time until 24 h. This increasing trend implies that the 304L surface can keep taking hydrogen for 24 h.

After the 24 h of loading the peak starts to reduce, as shown for 48 h and 60 h loading. The reduction of adsorbed hydrogen can be probably related to change in the ion transport mechanism due to the oxide layer formation, as schematically represented in figure 4.41. As time passes by, the oxide layer, forming in between the metal and the electrolyte, gets thicker, which changes the ion transfer path and the electrical double layer between the solid and the liquid. In the presence of an oxide layer, the ions go through three transport processes: metal-oxide interface, trough the oxide film itself, and oxide-electrolyte interface. Any of these three transport processes can be rate determining. In addition, the oxide layer formed can also have a lot of microstructural imperfections (e.g. vacancies) and in some cases can even be amorphous, which influences the ion migration [62]. In the case of Fe, Ni, and Cr, the oxide layers formed are semiconductive reason why the HER can still take place but on a different catalytic surface in comparison with the bare metal. Additionally, it can be observed that the peak potential (E_{pa} of hydrogen desorption) slightly varies, nonetheless, that is most probably an effect of small differences in the pH electrolyte.

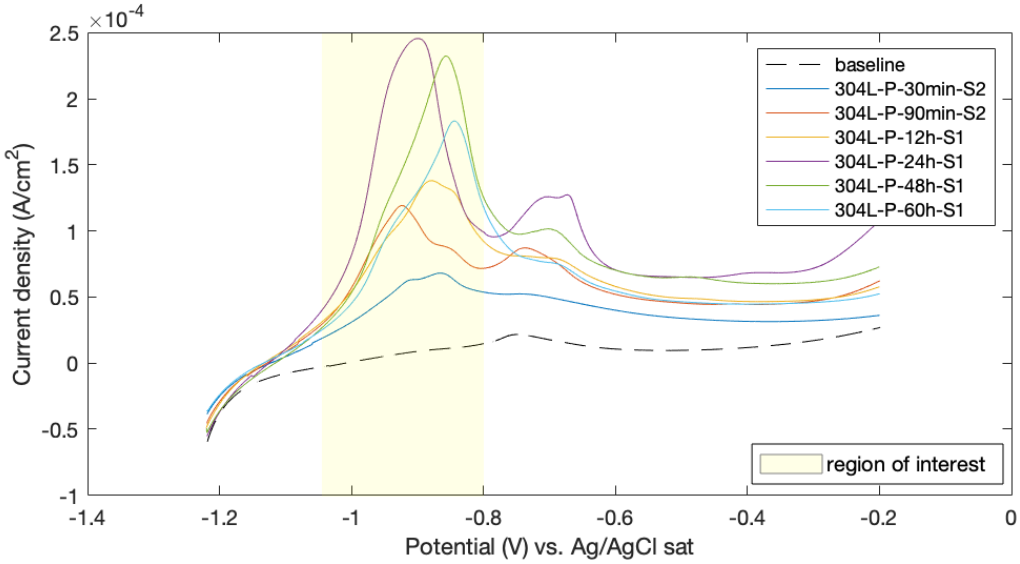

Figure 4.40: 1st CV scan after different H_2 loading times for 304L polished samples

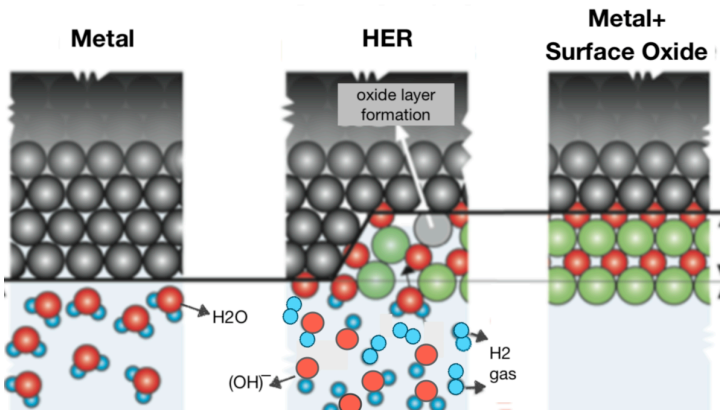

Figure 4.41: Schematic representation of the oxide layer formation on the metal surface during HER, adapted from [57]

Next, figure 4.42 presents the quantification of the hydrogen desorption peak for various loading times based on figure 4.40 in terms of surface charge density. The trend is characterised by a bell shape with a maximum adsorption value observed at 24 h of loading, which corresponds to the highest peak observed in figure 4.40. Rozenak [54] evaluated hydrogen electrochemical charging of 304 steel

during different times, and he reports that the sample reached the highest concentration of hydrogen at 24 h of loading after which the concentration started to decrease. This result coincides with the trend presented in 4.42.

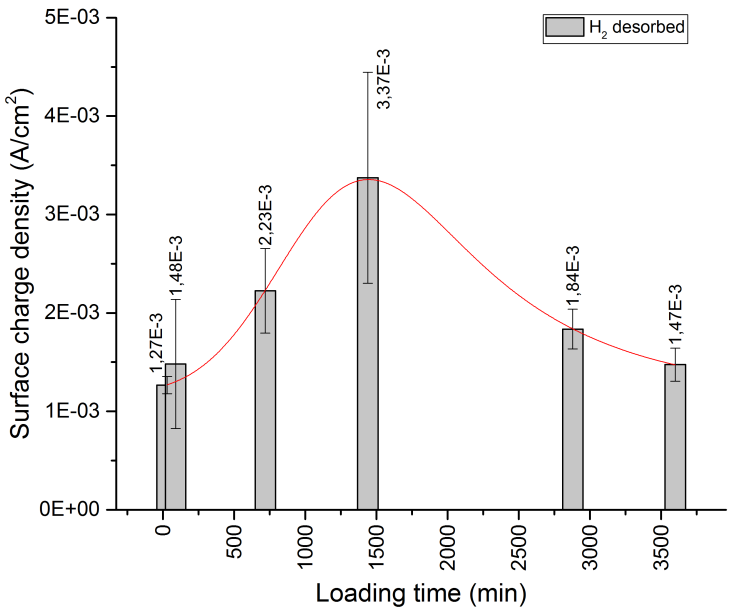

Figure 4.42: Quantification of surface charge density at different H_2 loading times for polished 304L samples, calculated from the H_2 desorption peak in the 1st CV after loading. The red line is a guide to visualise the curve trend.

Further on, figure 4.43 presents the surface charge density during hydrogen evolution (chronoamperometric step) at different times. Here, an increasing trend (towards more negative values) is observed. Implying that the longer the catalyst is kept at the hydrogen evolution potential, the more electrons will be detected (as current) as HER (equation 2) develops.

To make an overview of how much hydrogen was adsorbed in comparison to what was generated is necessary to take a look at the efficiency of electrochemical adsorption process (figure 4.44). An overall decreasing trend with time is observed. The maximum efficiency corresponds to the shortest loading time (30 min) in which the adsorption efficiency reaches up to 1.8%. After 60 h of loading the efficiency decreases to its lowest value of 0.089%, suggesting that longer times may result in almost insignificant percentages. This makes sense from the point of view that the surface charge density related to evolved hydrogen can keep increasing with time only until the material has reached saturation or until the oxide layer formed due to the hydrogen sorption/desorption process (light brown colouration observed by microscopy in section 4.2.1) reduces the catalyst activity of the metal acting as WE in such a way that the electroadsorption efficiency goes to zero.

Additionally, figure 4.45 presents the 4th CV scan after H_2 loading to analyse the oxidation state of the sample after the hydrogen has been completely desorbed (hydrogen desorption peak disappeared after the 1st CV scan). It is interesting to look at the proportionality existing between the amount of hydrogen taken up and the degree of nickel oxidation (peak B1) detected after desorption.

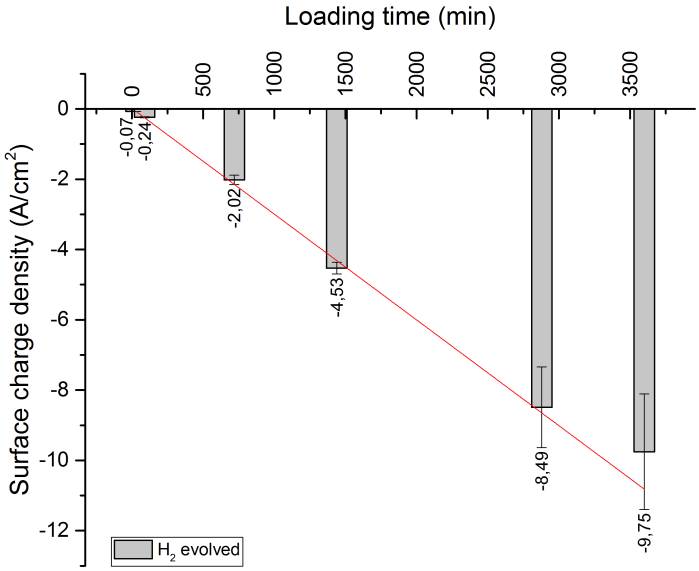

Figure 4.43: Quantification of surface charge density at different H_2 loading times for polished 304L samples, calculated from the chronoampometric step for H_2loading. The red line is a guide to visualise the curve trend.

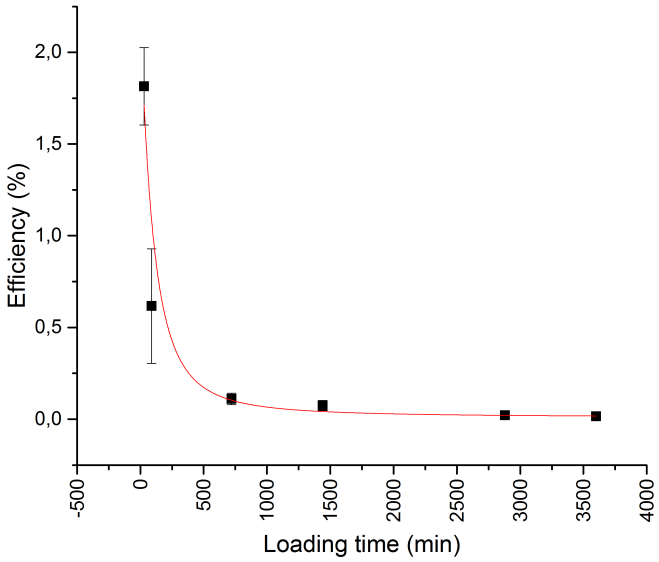

Figure 4.44: Electrochemical adsorption efficiency at different H_2 loading times for uncoated polished 304L samples. The red line is a guide to visualise the curve trend.

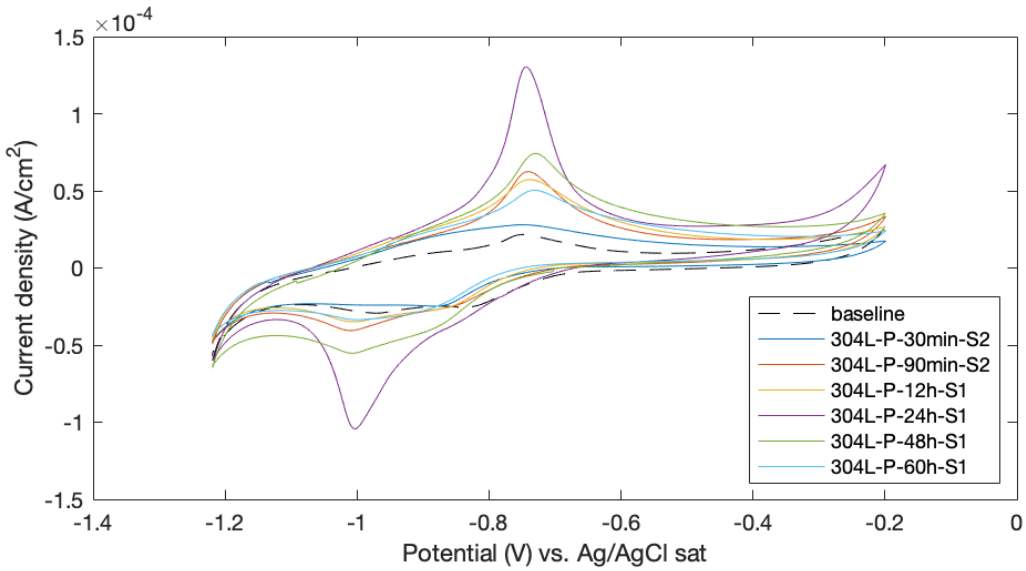

Figure 4.45: 4th CV scan after H_2 loading of uncoated polished 304L samples at different loading times

Coated 304 L (with TiO_2 layer on top)

Figure 4.46 shows the evolution of the hydrogen desorption peak with loading time. In this particular case, we observe that there is an important increment in the H_2 desorption peak from 30 min to 60 min. However, the difference at longer loading times with respect to 60 min is almost negligible. This behaviour is easier to observe looking at figure 4.47, where the surface charge density associated with desorption reaches a quasi-stable state after 60min. The difference in the trend between the coated and uncoated 304L is easy to understand from the point of view that the TiO_2 layer is chemically very stable. On the other hand, the uncoated 304L is susceptible to oxidation. The fact that the uncoated 304L is prone to form an oxide layer implies that the electrical double layer (during the HER) is not steady as explained in the previous section. A changing EDL influences the hydrogen adsorption; this is the reason why the uncoated 304L exhibited a shape bell (as presented in section 4.42).

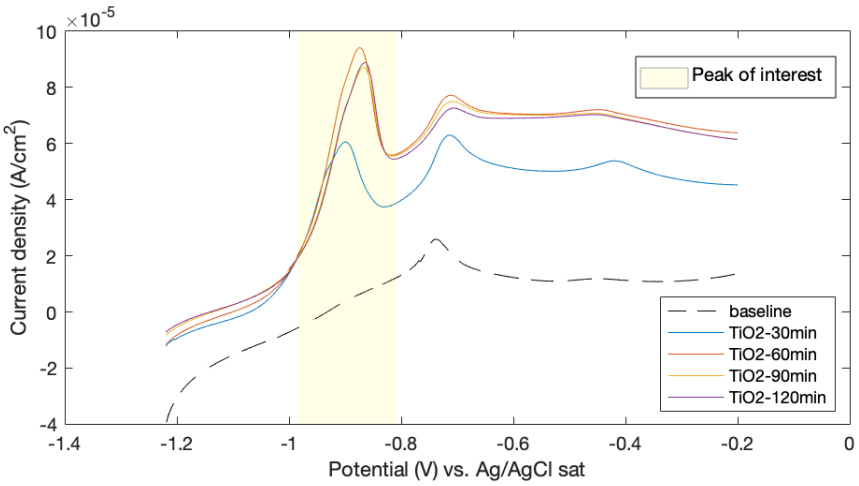

Figure 4.46: 1st CV scan after different H_2 loading times for coated 304L, meaning that that the TiO2 layer in is direct contact with H_2

Next, figure 4.48 presents the surface charge density associated with the chronoamperometric step. In comparison with the uncoated 304L the trend of increment is not so pronounced, meaning that the evolution of hydrogen is more controlled (not huge increments). Looking more in detail, one observes that the amount of hydrogen evolved is considerably less than in uncoated 304L. This observation implies that the TiO_2 is not the as good catalyst for HER as bare 304L is.

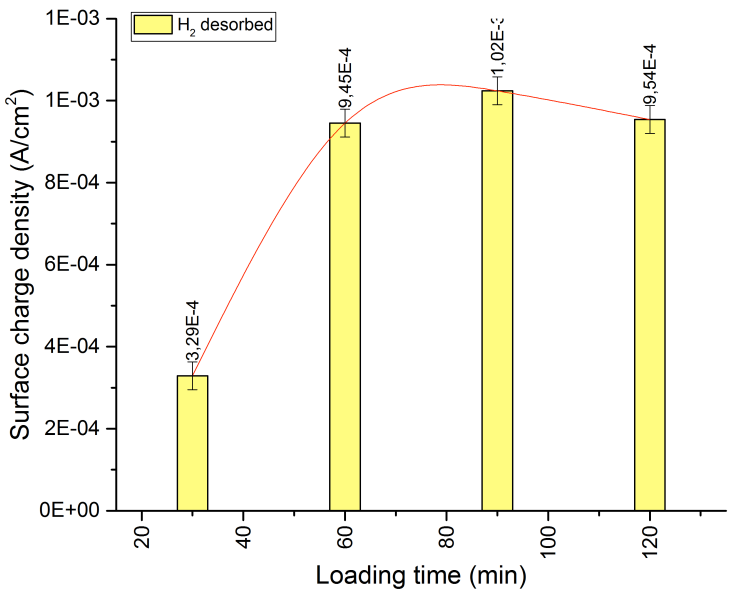

Figure 4.47: Quantification of surface charge density at different H_2 loading times for polished 304L samples, calculated from the H_2 desorption peak in the 1st CV after loading. The red line is a guide to visualise the curve trend.

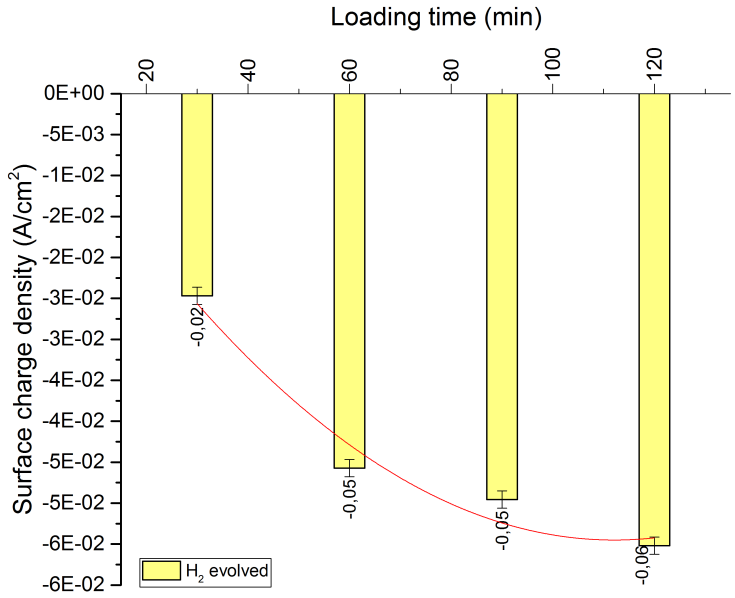

Figure 4.48: Quantification of surface charge density at different H_2 loading times for polished 304L samples, calculated from the chronoampometric step for H_2loading. The red line is a guide to visualise the curve trend.

Finally, the electrochemical adsorption efficiency is presented in figure 4.49. The trend presented differs from the one corresponding to uncoated 304L. In this case, since the amount of evolved hydrogen does not increase abruptly, it can still be comparable with the amount of hydrogen desorbed so that an initial increment of efficient is observed.

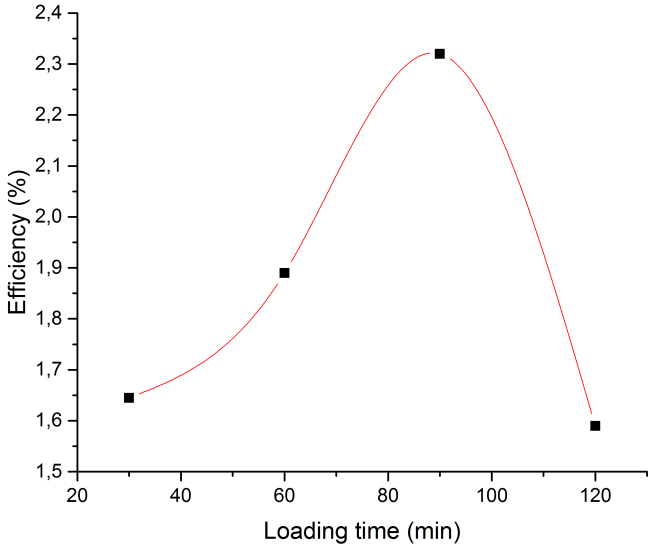

Figure 4.49: Electrochemical adsorption efficiency at different H_2 loading times for coated 304L samples (with TiO_2). The red line is a guide to visualise the curve trend.

Polished Invar

Figure 4.50 displays the evolution of the hydrogen desorption peak for the invar samples at different H_2 loading times. In this case, the peak of interest (peak E1 from figure 4.36) is located in the shaded region and the trend is not so clear to analyse simply from the graph. However, some remarks can be made like, for example, that the peak at 30 min loading is highly influenced by the peak preceding it (peak A1 from figure 4.36). As the times passes by, peaks A1 and E1 seem to get separated. To get a better understanding of the peaks' areas relation we refer to figure 4.51.

Figure 4.51 shows the trend of the hydrogen desorption peak area as function of loading time. Once again, a bell shape is depicted. At 2 h of loading time, the highest surface charge density was registered. After 12 h loading, the charge decreases significantly, almost reaching the same value that at 60 min loading. The electrochemical adsorption efficiency is depicted on figure 4.53.

Figure 4.54 shows the oxidation state of the polished Invar after the 4^{th} CV scan after H_2 loading. The highest couple of peaks correspond to 2 h of loading time, which coincides with the highest desorption peak in the 1^{st} CV scan (figure 4.50). It is also remarkable that only iron oxide is formed (according to the enlargement of the Fe peak) even though the amount of Ni is considerably high in this alloy. In addition, it is possible to conclude that the chemical composition of the surface has been severely modified after the induced hydrogen exposure, which is consistent with the observations by microscopy (section 4.2.4).

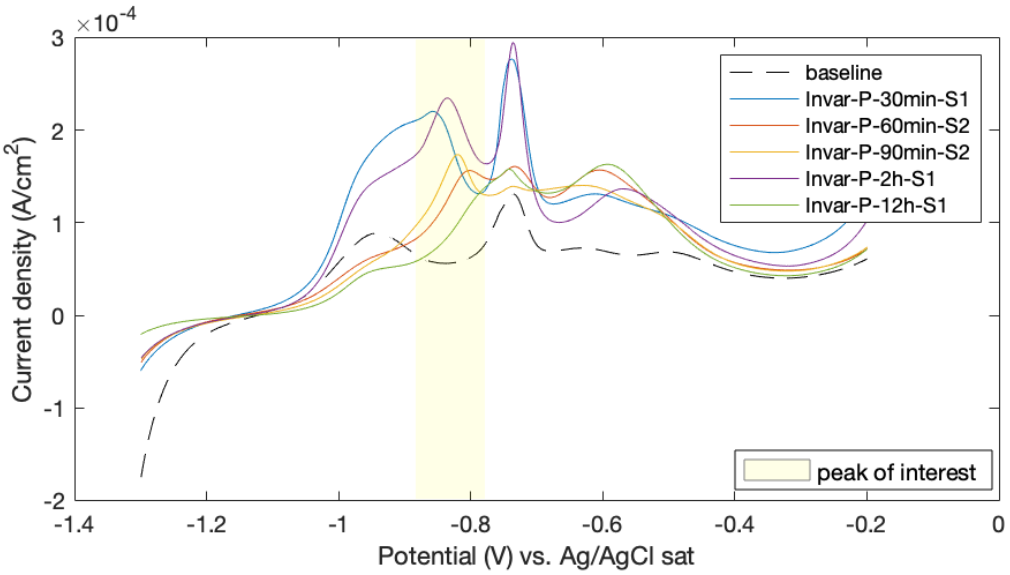

Figure 4.50: 1st CV scan after different H_2 loading times for polished Invar samples

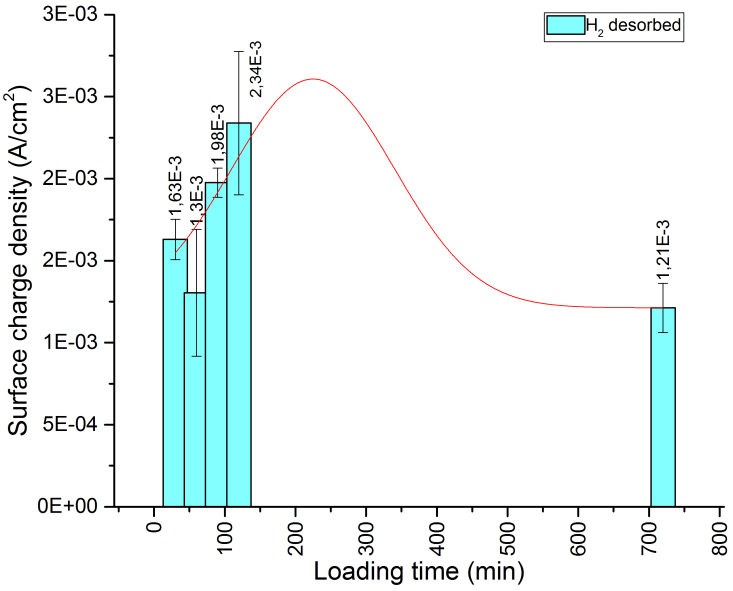

Figure 4.51: Quantification of surface charge density at different H_2 loading times for polished Invar samples, calculated from the H_2 desorption peak in the 1st CV after loading. The red line is a guide to visualise the curve trend.

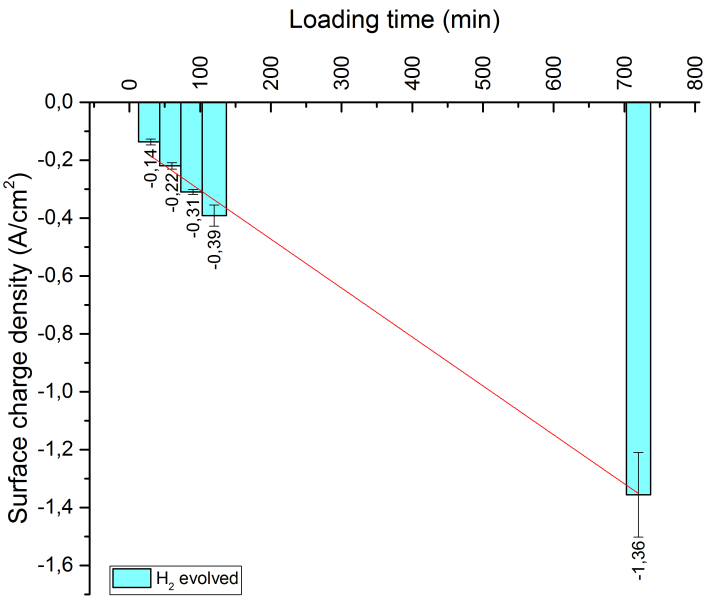

Figure 4.52: Quantification of surface charge density at different H_2 loading times for polished Invar samples, calculated from the chronoampometric step for H_2loading. The red line is a guide to visualise the curve trend.

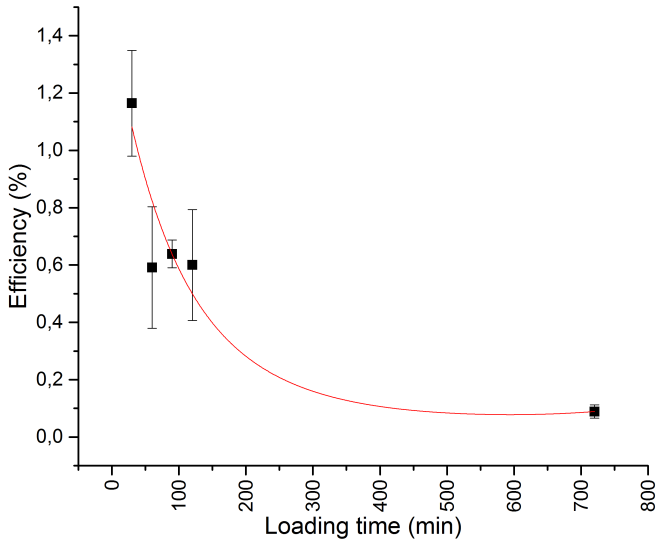

Figure 4.53: Electrochemical adsorption efficiency at different H_2 loading times for polished Invar. The red line is a guide to visualise the curve trend.

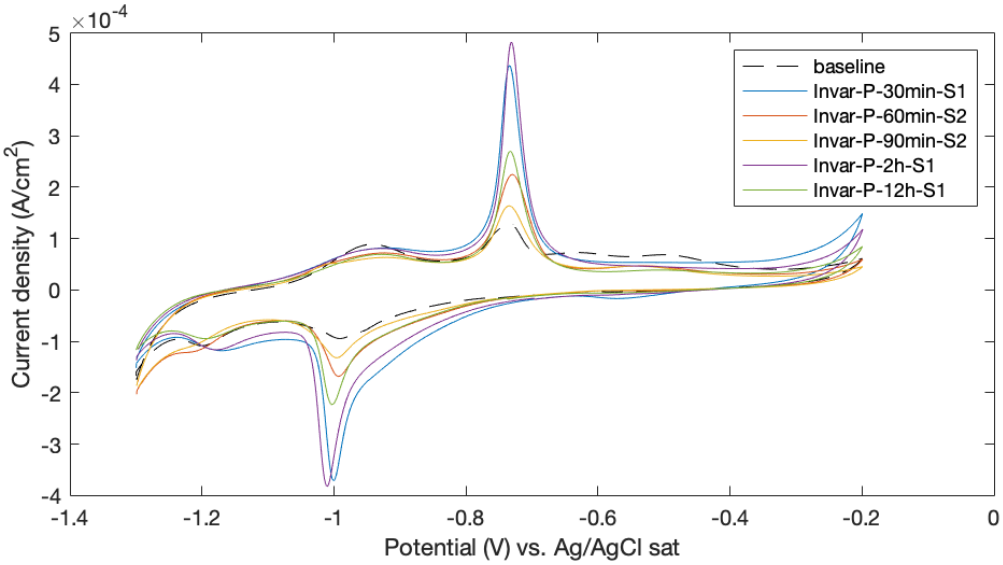

Figure 4.54: 4th CV scan after H_2 loading of polished Invar samples at different loading times

4.4.5. Saturation time and comparison of the different regions

Figure 4.55 presents a comparison between coated and uncoated 304L stainless steel, and Invar in terms of desorption surface charge density up to 12h. Within this period of time, the trend shows that the uncoated 304L continues desorbing hydrogen. The coated 304L (labelled as TiO_2) reaches a quasi-steady state whereas the Invar sample already reached saturation so that the desorption decreased.

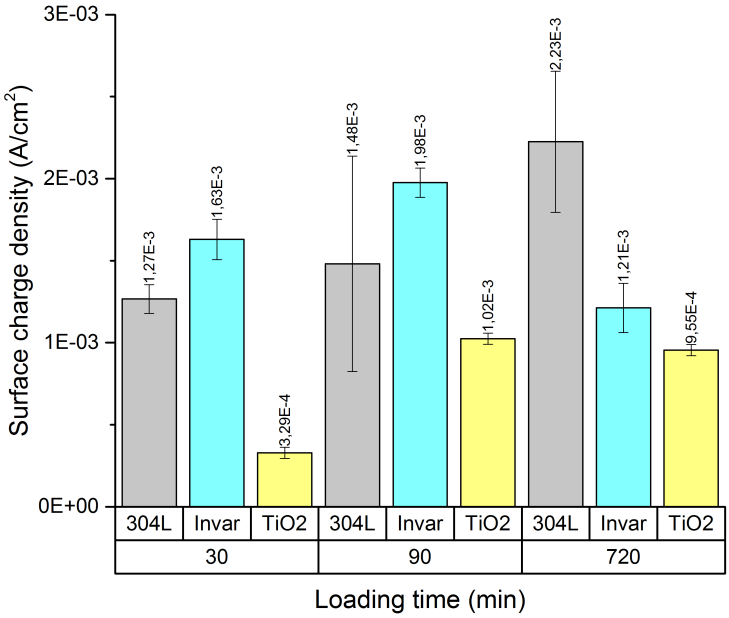

Figure 4.55: Surface charge density as a function of time for the different flat iron-based alloys regions

Figure 4.56 compares the surface charge density (which is proportional to hydrogen electrochemical desorption) at the saturation time of each material depicting the following trend: coated 304L (with TiO_2)< Invar < uncoated 304L. Therefore, the results showed that uncoated 304L is the most prone material to electrochemical hydrogen adsorption. This also means that the TiO_2 coating is protecting the bare 304L against hydrogen intake, which is desirable for the cargo transport application. Perfect oxide surfaces are essentially inert to hydrogen dissociative adsorption because oxygen prevents the H_2 dissociative step [50] which explains the considerable reduction in the amount of hydrogen desorption peak in comparison with the bare 304L. Nonetheless, during wearing and maintenance operations, it is possible that the coating can get damaged and the protective effect gets diminished. On the other hand, if comparing the Invar and uncoated 304L, the Invar adsorbed less hydrogen than 304L.

Next figure 4.57 shows the comparison among the different sections (flat regions and welds) within the same ship's container. It is shown that at the welds, the surface charge density associated with hydrogen desorption is consistently higher for both welds 304L and Invar. This implies that the welds are the most vulnerable section of the tanks. Nonetheless, the welded regions exhibited a rough surface, as shown in section 4.2.4, which means that active surface for the HER region is larger than the geometrical area. Therefore, there is an error associated with the in the quantification of the surface charge density. The true value is probably smaller than the one reported, considering that the same current should be divided into a larger effective area. The effective area[7] was not calculated in the present project. However, even if the difference with respect to the geometrical area is 50%, the amount of the surface charge associated with the hydrogen desorption peak will still be significantly higher than any other region tested. Therefore, no change in the present trends

[7]The effective area can be calculated with the roughness factor

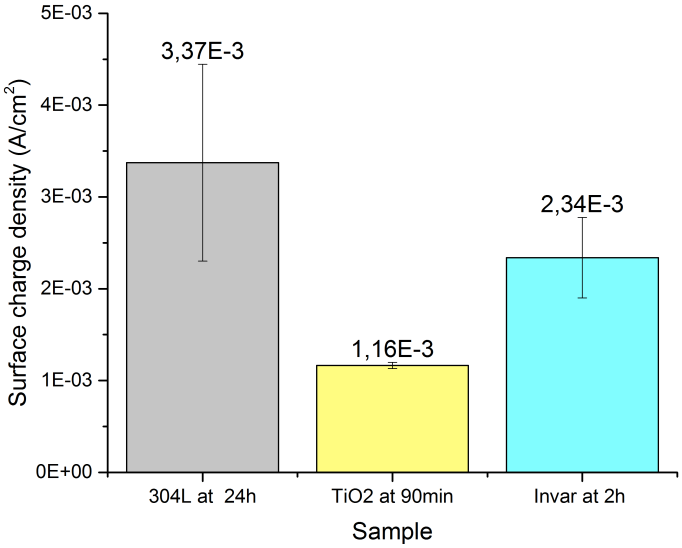

Figure 4.56: Comparison of the surface charge density associated with the desorption peak at the saturation time for the different iron-based alloys

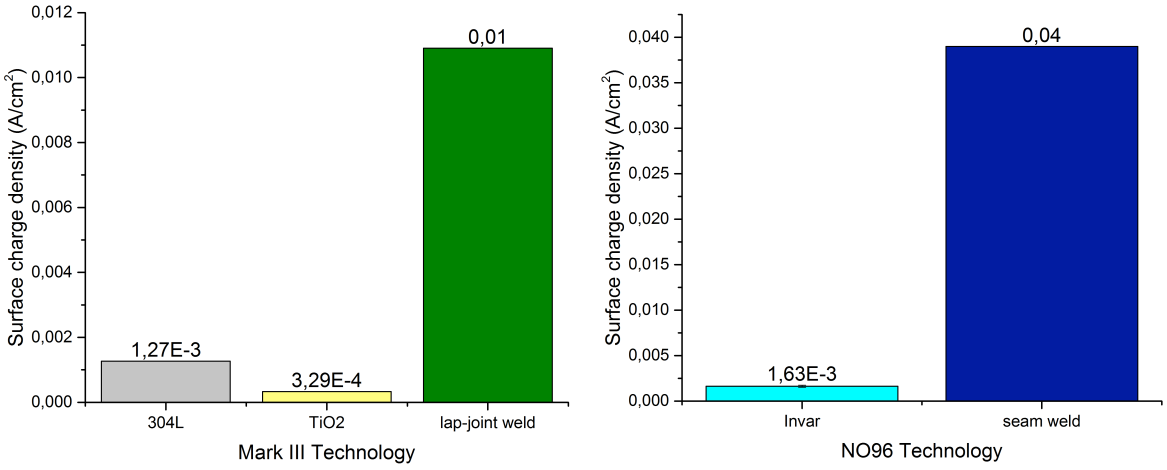

(a) Mark III **(b)** NO96

Figure 4.57: Comparison of surface charge density associated to hydrogen desorption of the different components of each GTT's technologies for a loading time of 30 min.

4.4.6. Influence of surface finishing

In this section each material was tested when the surface finishing was far from smooth as in the polished surface (ideal condition). To make the surface rough, the samples were sanded with sanding paper grit #320 for 30 seconds. The surface finishing comparison was made only for a 30 min H_2 loading time.

Uncoated 304L

Figure 4.58 compares the CV scans of the rough and polished surfaces before (dashed line) and after (solid-line) 30 min of H_2 loading. The most remarkable difference is that the peak B corresponding to Ni oxidation (pointed with an arrow), is enlarged when the surface is rough, both in the baseline and after H_2 loading. This makes sense from the point of view that a rough surface implies that the geometrical area to which the current density is referred to, is not equal than the true area like in the polished surface. All the peaks and valleys that the rough surface has, increase the true area exposed to hydrogen. Consequently, more oxide formation is expected after hydrogen exposure. However, to explain the increment in the peak before the loading, we simply need to refer to the pre-processing of the sample. When polishing the sample, the intention is to guarantee that all the oxides (passivation layers) have been removed what is not necessarily the case for the rough sample. On the other hand, the hydrogen desorption peak showed for both cases is almost the same in height.

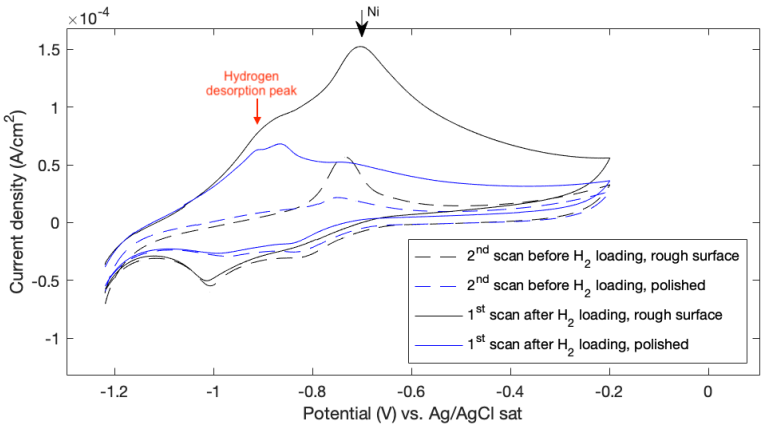

Figure 4.58: 2nd CV scans after H_2 loading times for ground 304L (sanding paper grit 1200)

Invar

The same analysis was conducted for the case of Invar. In this case three different surface finishing were compared: polished sample, the as-recieved sample (that was not smooth) and the sanded sample.

Figures 4.59 and shows the cyclic voltammogram before H_2 loading for the different surface finishes of Invar. The cyclic voltammograms of the different surface finishes before H_2 loading present the same peaks previously identified with a slight variation on the amount of oxidation of iron for each case. The polished surface is the one having higher peaks corresponding to Fe oxidation (peaks A and B).

On the other hand, 4.60 shows the 1st CV scan after 30 min of H_2 loading, the hydrogen desorption peak corresponding to the as-received surface was almost the same height as the polished one but slightly shifted to the left. The as-received surface corresponds to the less homogeneous surface that could also have been contaminated with oxides or other substances present from even before the exposure. On the other hand, the sanded sample presented the lower hydrogen desorption peak. Even though the true area exposed was bigger, it is possible that the active sites for the HER to take place were not available due to contamination of the surface. It was empirically observed during sample preparation that the Invar material, in particular, required to be polished and electrochemically measured right away; otherwise, the CV showed different behaviour. From this observation, it is easier to

understand that the polished surface (ideal condition) gave the highest hydrogen desorption peak in comparison to the other surface finishes.

Overall, it was shown that the increment of the roughness on the sample surface might result in a slight variation of the hydrogen ingress amount due to the presence of oxides or contamination in the surface, more than due to the increment in the true area.

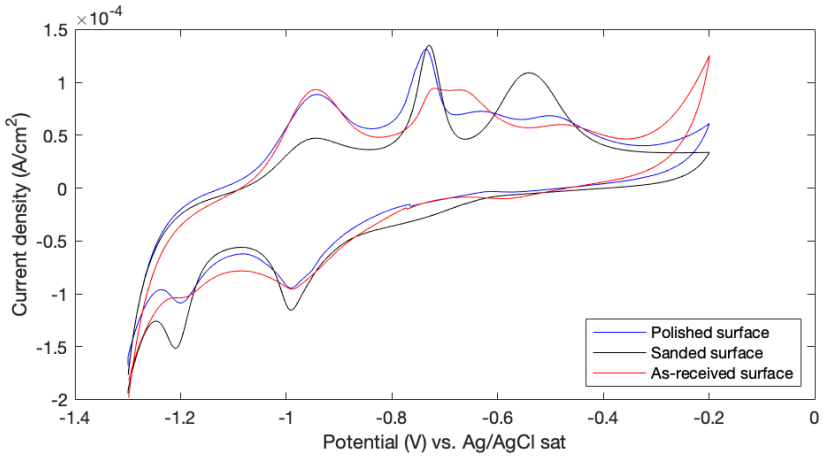

Figure 4.59: 2nd CV scans before H_2 loading for different surface finishes of Invar alloy

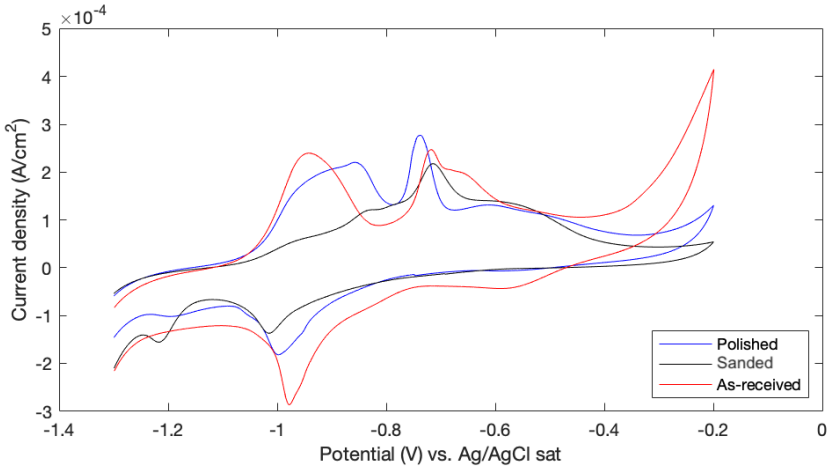

Figure 4.60: 1st CV scans after H_2 30 min loading time for different surface finishes of Invar alloy

5

Conclusions

The conclusions are presented as answers to the proposed research questions in section 1.0.1.

1. The electrochemical approached, composed by the cyclic voltammetry and the chronoamperometric techniques, demonstrated to be a powerful tool that allows evaluating hydrogen sorption on metal surfaces at laboratory scale. This methodology showed great advantages like,

   - Safety handling conditions of hydrogen in comparison with its liquid (cryogenic temperature) or gas (flammable substance) states.
   - Small sampling area (20 mm x 16 mm) required for the electrochemical test.
   - Good reproducibility is attainable once the conditions and parameters of the electrochemical experiment are well defined such as, an adequate selection of the potential range for the CV (mainly the selection of Ei), a stable reference electrode (RE) at the working pH, and consistency in both the electrolytic set up configuration (constant distance between the electrodes) and same sample surface preparation every time.
   - The electrochemical approach allowed to obtain a trend of the susceptibility to hydrogen intake of different materials. The cyclic voltammetry technique generates accelerated conditions in comparison with real-life hydrogen gas-metal interaction at atmospheric pressure.

   However, the electrochemical approach showed certain limitations as well,

   - Due to the mechanism reaction of the HER and the nature of the catalyst, the following aspects need to be considered,
     (a) If a non-adequate potential range (mainly Ei) is selected, the HER generates significant hydrogen gas bubbling. This hinders accurate reading of the current during the hydrogen loading step and prevents the hydrogen ingress into the sample.
     (b) Some hydrogen is being desorbed by the Tafel mechanism that cannot be measured by the electrochemical technique because this reaction does not involve electrons.
   - The proximity of the oxidation potential of hydrogen (desorption peak) with the iron oxidation peak results in a peak overlapping that hinders a straightforward quantification of the amount of hydrogen desorbed.
   - The occurrence of dissociative chemisorption on the metal surface in the gas or liquid environment (absence of an induced electrochemical process) cannot be asses by this method.

2. The electrochemical techniques successfully allowed to detect and quantified the amount of adsorbed hydrogen. Nonetheless, the values obtained from the quantification of the desorption peak depend on the setting of the experiments (selection of potential range) and the amount of hydrogen evolved in the sample. Despite this, the method allows comparing the different materials tested and provide a measure of hydrogen susceptibility under hydrogen exposure.

The CV results showed that the hydrogen ingress, in the flat regions of the tested materials, increases in the following order: coated 304L (with TiO_2 coating)< Invar < uncoated 304L. It can be concluded that the TiO2 coating on 304L reduces the tendency to hydrogen sorption.

Hydrogen ingress in the welds was significantly higher than in the corresponding flat regions. Therefore, the welded regions are consistently more vulnerable than any of the other tested regions for both of the GTT technologies (Mark III and NO96).

The saturation time for hydrogen ingress is also material dependent and increases in the following order for the flat regions: coated 304L (with TiO_2 coating)< Invar < uncoated 304L. Uncoated 304L is the most prone material to electrochemical hydrogen sorption.

Preliminary permeability tests (Appendix C) showed that some hydrogen generated by the HER is being absorbed into the bulk material.

The increment in the surface roughness did not influence the hydrogen intake significantly, but it changes the initial oxidation state of the sample surface.

3. After the hydrogen exposure, the chemistry of surface is irreversibly changed due to the formation of oxides. The origin of the oxidative process of the metal surfaces is not fully clear, but it is presumably a consequence of the cyclic voltammetry technique itself.

   For 304L stainless steel, also an increase of the relative amount of austenite was observed after hydrogen absorption. This hints to a phase transformation from BCC to FCC (austenite to ferrite) that is suggested to be caused by the increase of compressive stress upon hydrogen loading. In addition, the lattice parameter of 304L appears to be slightly increased presumably due to the formation of iron-hydride. No such changes were observed for the Invar austenitic phase.

6

Recommendations and Outlook

A deeper understanding of the mechanism behind the surface and microstructural changes, resulting by the hydrogen-metal interaction, can be achieved by the following recommendations,

- To characterise the oxide layer formed on the bare metals (304L and Invar), e.g. by X-ray photo-electron spectroscopy (XPS).
- To investigate the role of the oxide layer during the hydrogen loading step.
- To test the behaviour of all the components that are going to be exposed to hydrogen to identify regions of vulnerability. There are other section of the containment, not yet included in the present study, that need to be tested: corrugated parts of 304L and lap-joint weld for Invar alloy.
- To study the effect of deformation (defects) and stresses on hydrogen absorption. In particular, the corrugations corresponding to GTT Mark III technology, presumably present induced martensite formation due to deformation. The evaluation of martensite is important because it can act as a highway for hydrogen transport.
- To conduct a detailed study of permeability, absorption, and diffusivity for the different materials as a next step of the investigation.
- To study the type and amounts of traps present in the bulk material by thermal desorption spectroscopy (TDS). Also, TDS can be explored as an alternative method for quantification of adsorbed hydrogen.
- It would be necessary to test the behaviour of the iron-based alloys, 304L stainless steel and Invar, under the actual conditions in a storage tank. This implies in a hydrogen gas environment, P=1atm and -240°C < T < 25°C, to evaluate the probability of dissociative chemisorption and absorption of hydrogen.

The current electrochemical experiment can be improved according to the following guidelines,

- To use a reference electrode designed explicitly for alkaline conditions. The best would be to have the same solution acting as the electrolyte and the filling solution to avoid ions leakage (contamination).
- To conduct electrochemical polishing instead of mechanical polishing to prevent induced stresses on the metal surface during sample preparation.

A

Cyclic Voltammetry Results

A.1. Polished 304L

A.1.1. 30 min of H_2 loading

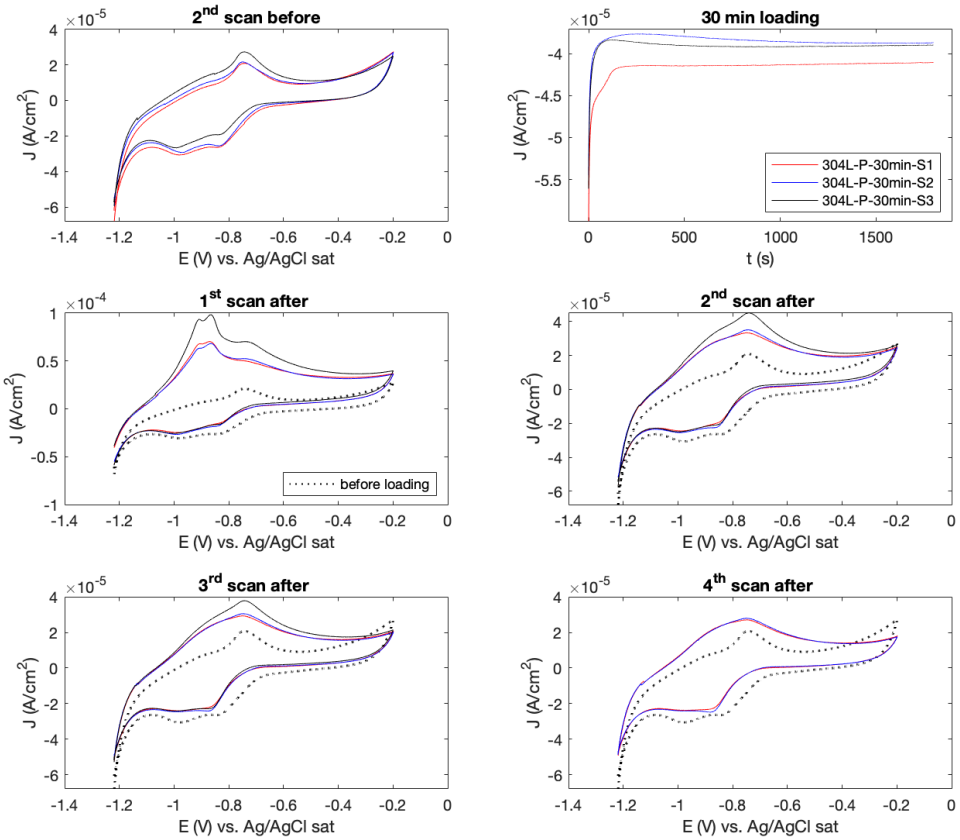

Figure A.1: CV scans corresponding to the replicas of polished-uncoated 304L, before and after 30 min of H_2 loading

A.1.2. 90 min of H_2 loading

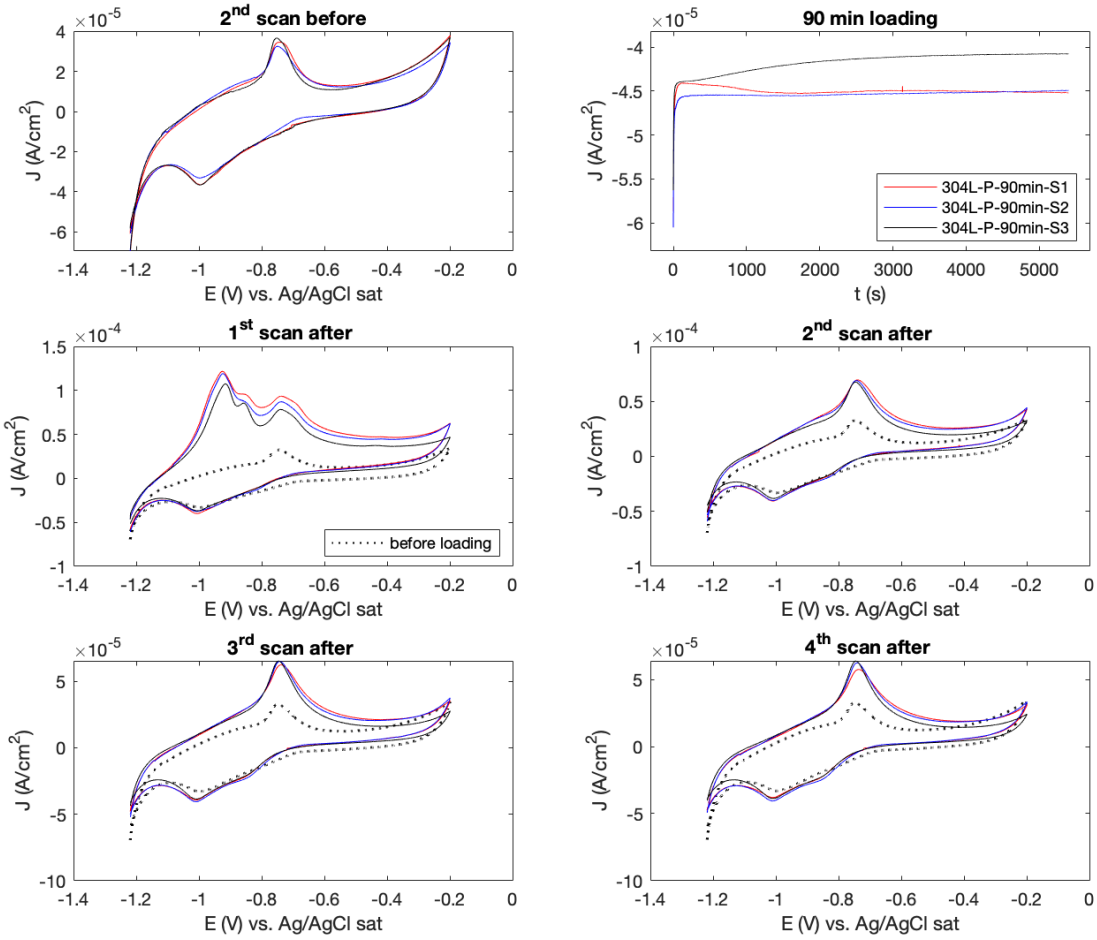

Figure A.2: CV scans corresponding to the replicas of polished-uncoated 304L, before and after 90 min of H_2 loading

A.1.3. 12 h of H_2 loading

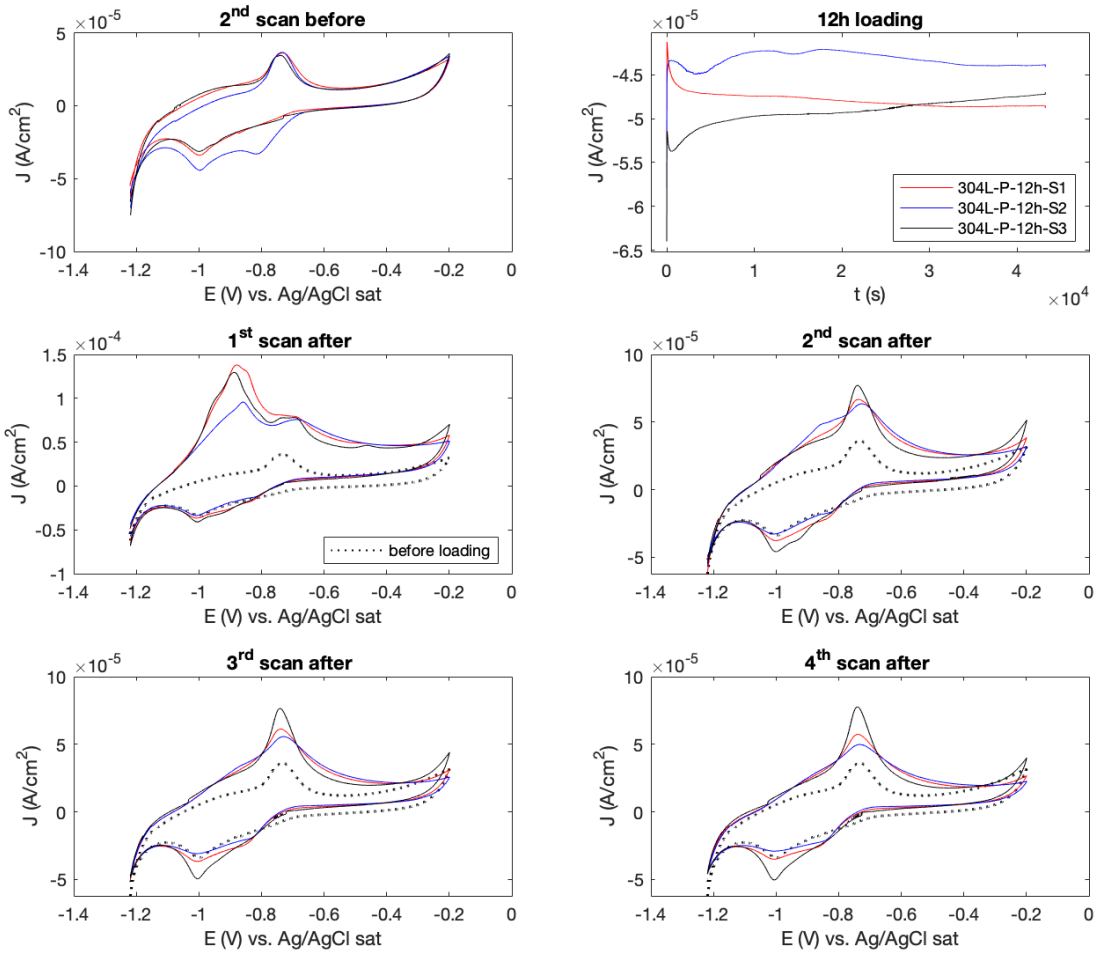

Figure A.3: CV scans corresponding to the replicas of polished-uncoated 304L, before and after 12 h of H_2 loading

A.1.4. 24 h of H_2 loading

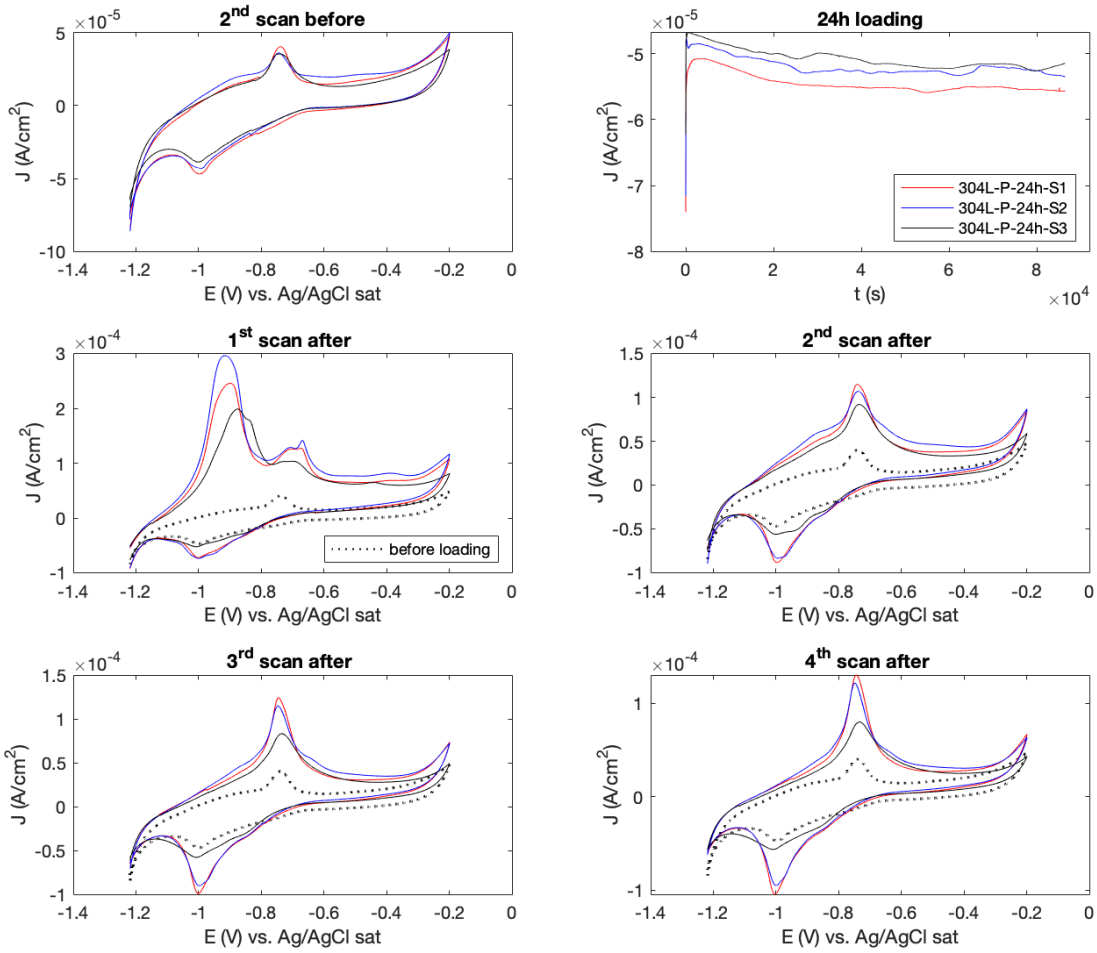

Figure A.4: CV scans corresponding to the replicas of polished-uncoated 304L, before and after 24 h of H_2 loading

A.1.5. 48 h of H_2 loading

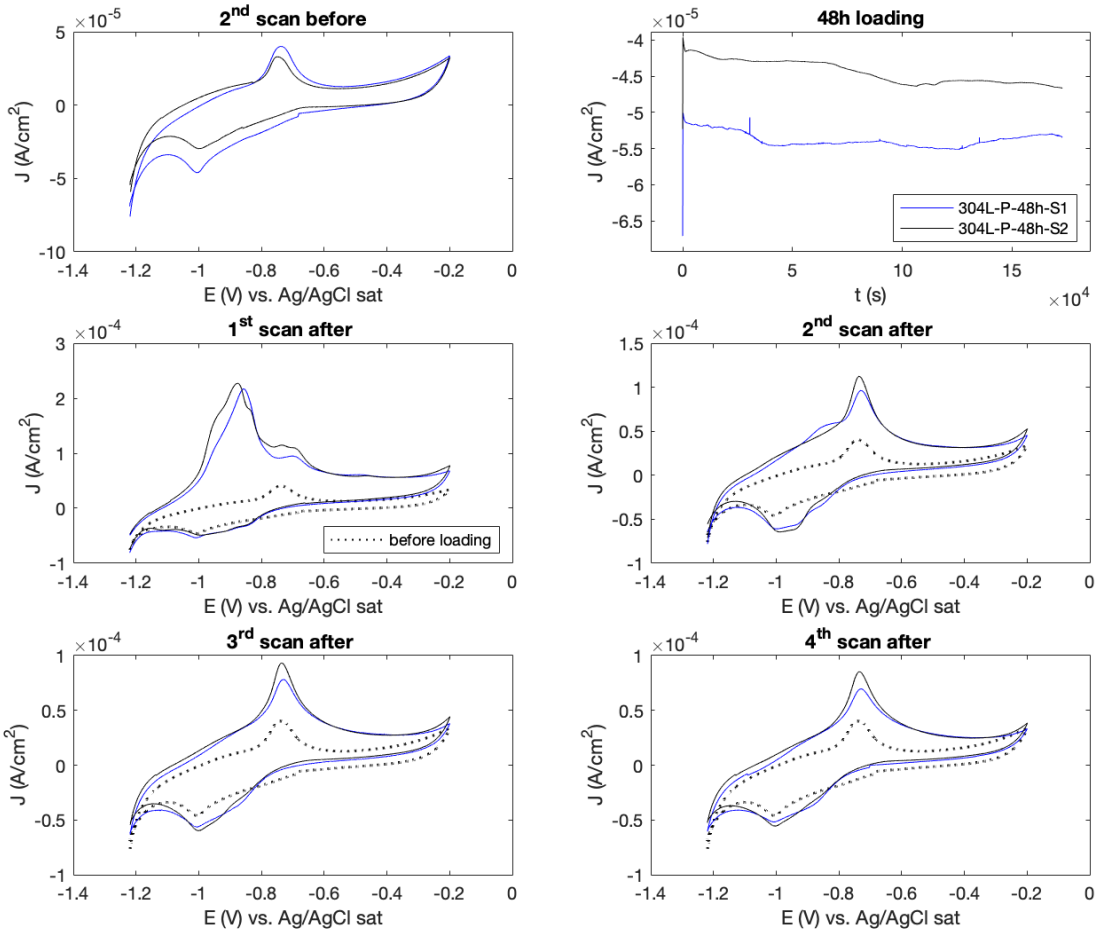

Figure A.5: CV scans corresponding to the replicas of polished 304L, before and after 48 h of H_2 loading

A.1.6. 60 h of H_2 loading

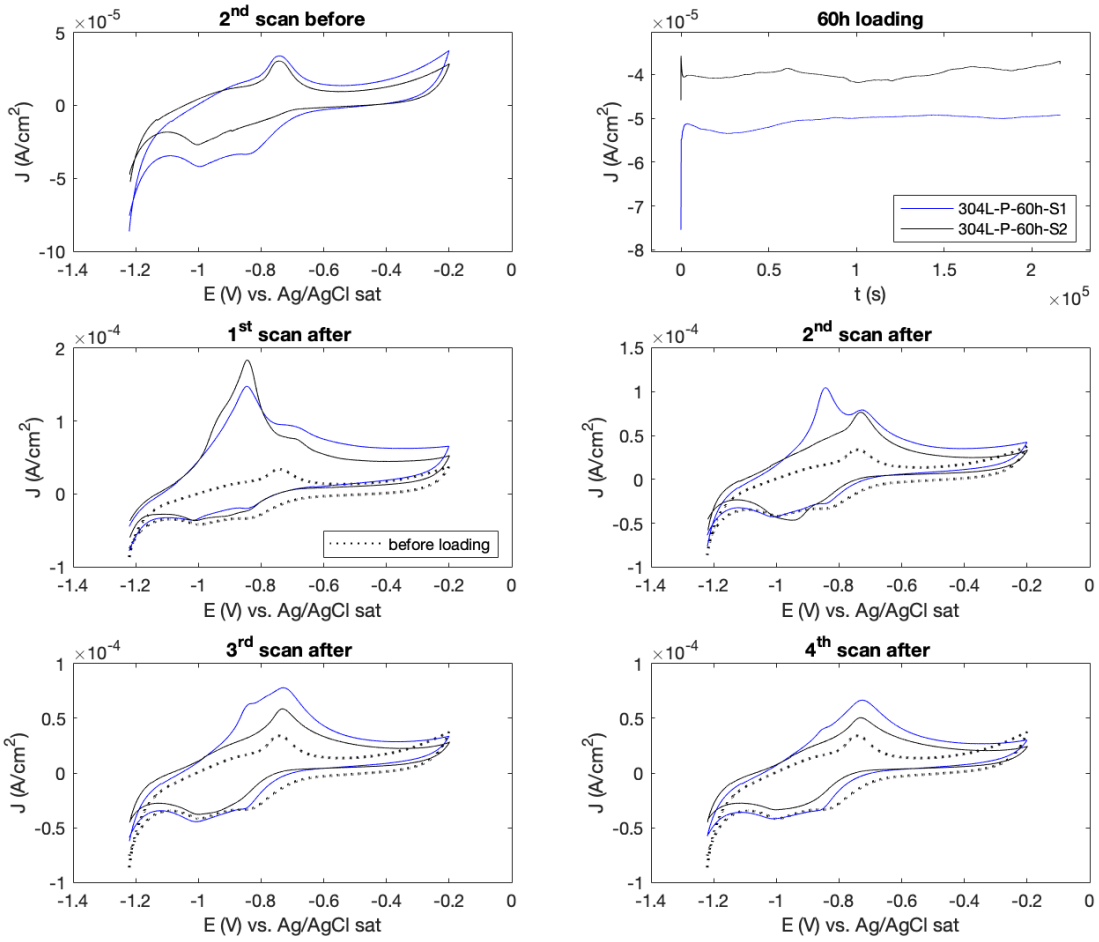

Figure A.6: CV scans corresponding to the replicas of polished-uncoated 304L, before and after 60 h of H_2 loading

A.2. As received 304L -with TiO2 coating

A.2.1. 30 min of H_2 loading

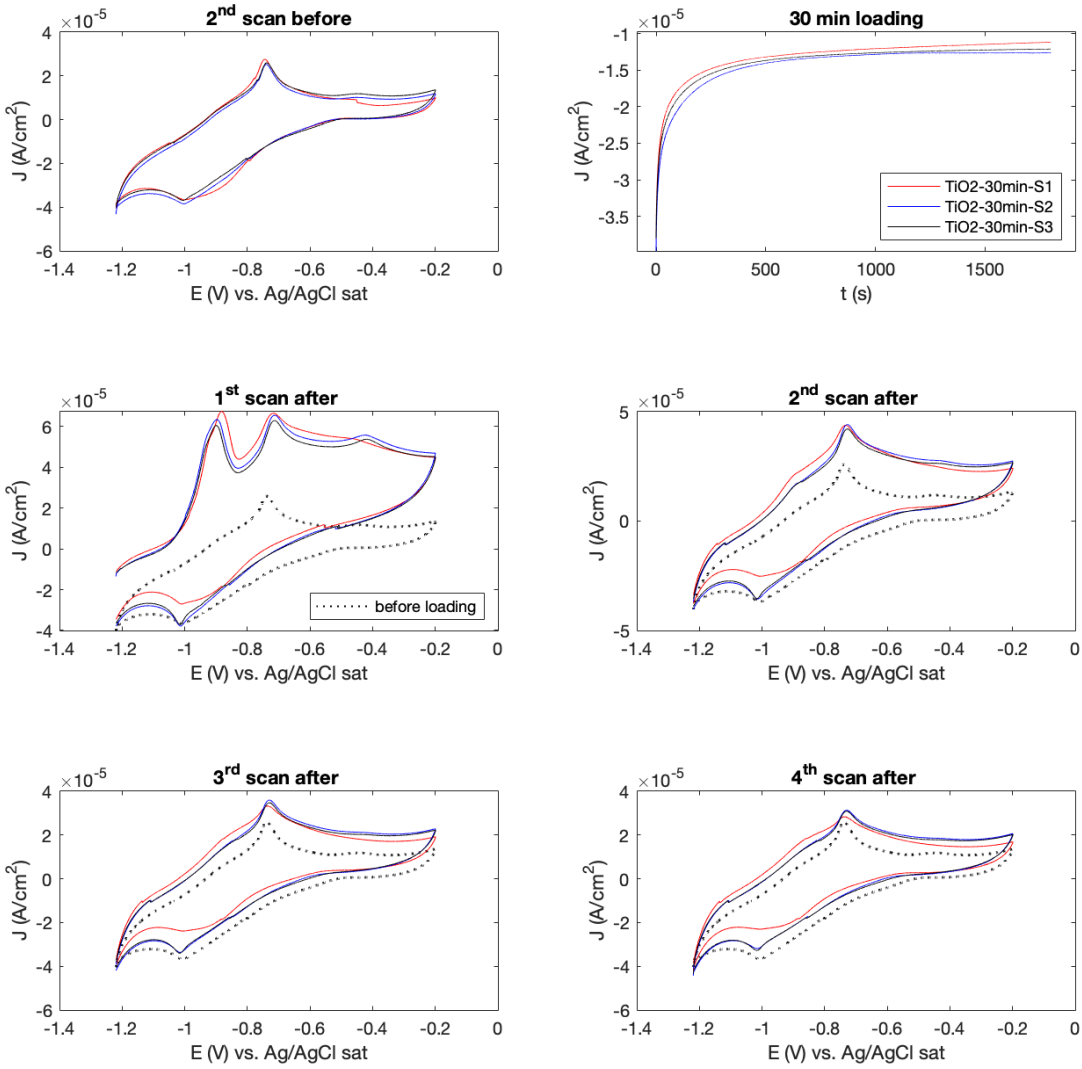

Figure A.7: CV scans corresponding to the replicas of TiO2 (coated 304L), before and after 30 min of H_2 loading

A.3. Polished Invar

A.3.1. 30 min of H_2 loading

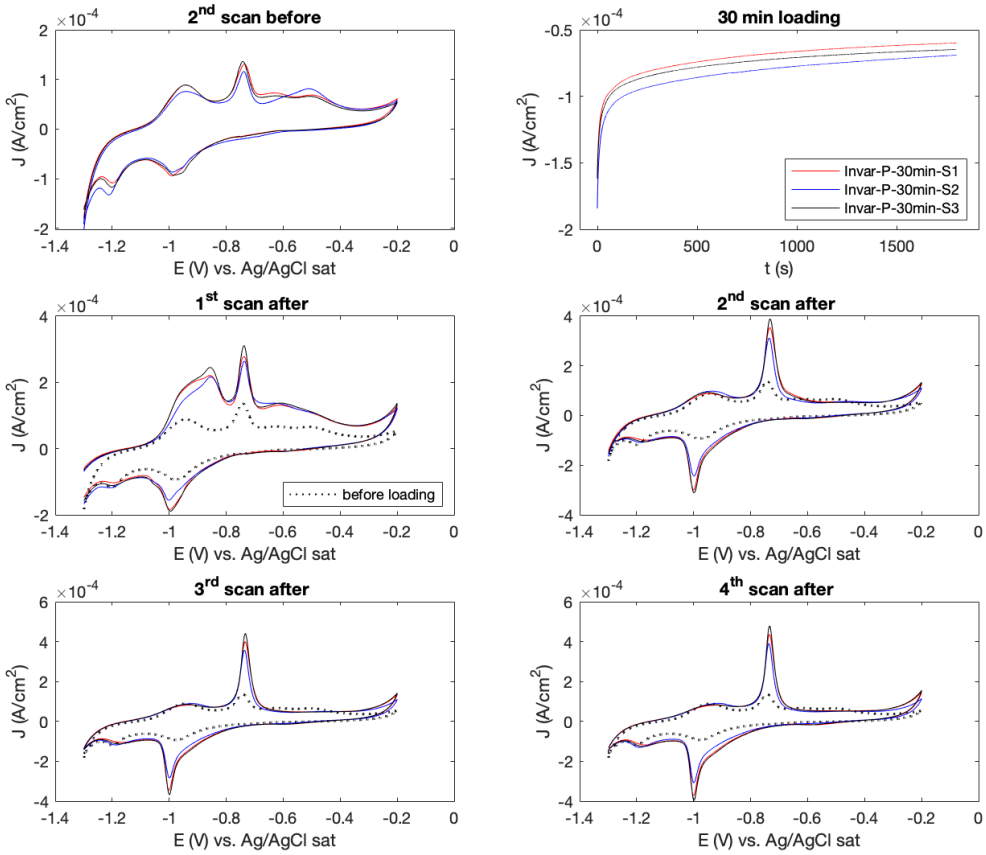

Figure A.8: CV scans corresponding to the replicas of polished Invar, before and after 30 min of H_2 loading

A.3.2. 60 min of H_2 loading

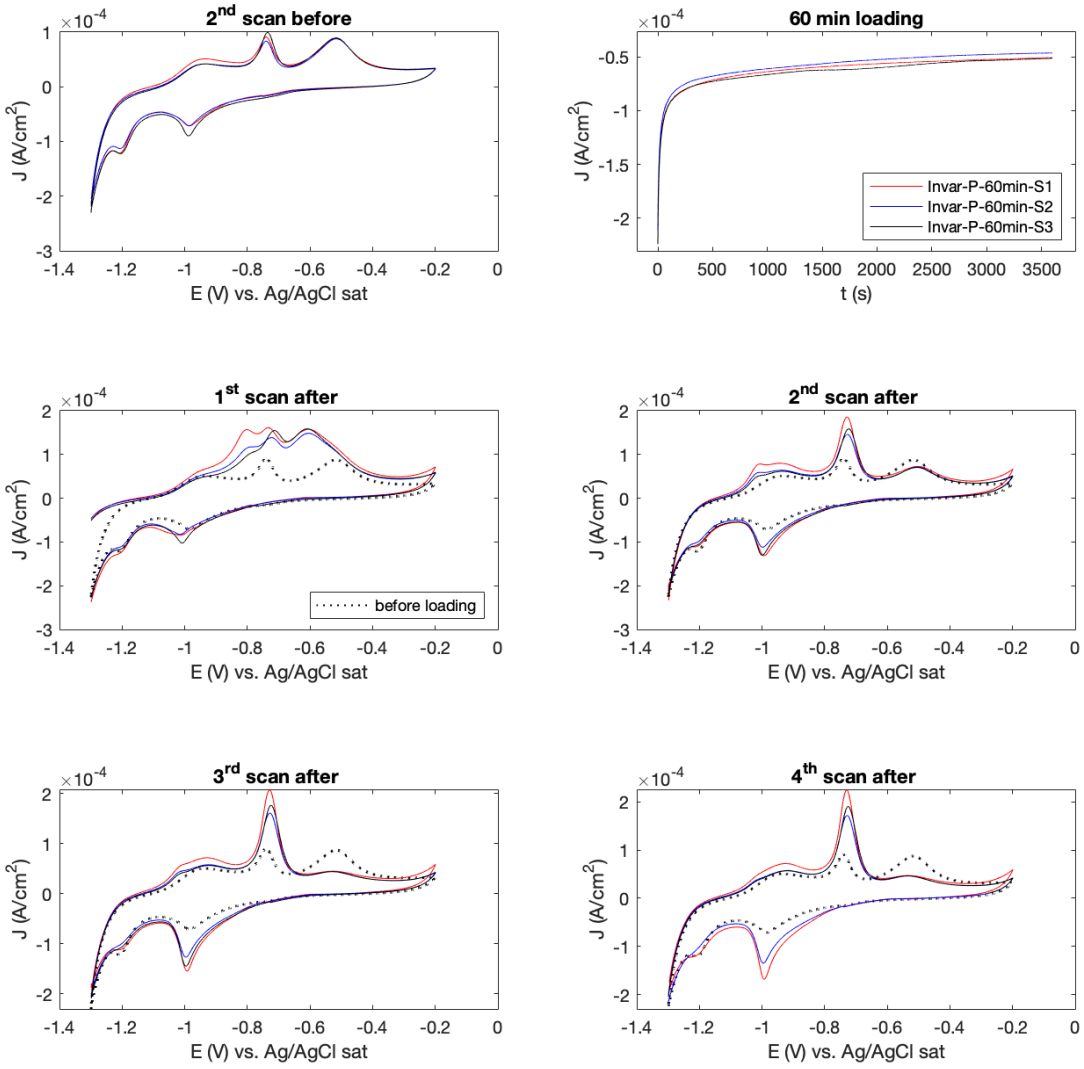

Figure A.9: CV scans corresponding to the replicas of polished Invar, before and after 60 min of H_2 loading

A.3.3. 90 min of H_2 loading

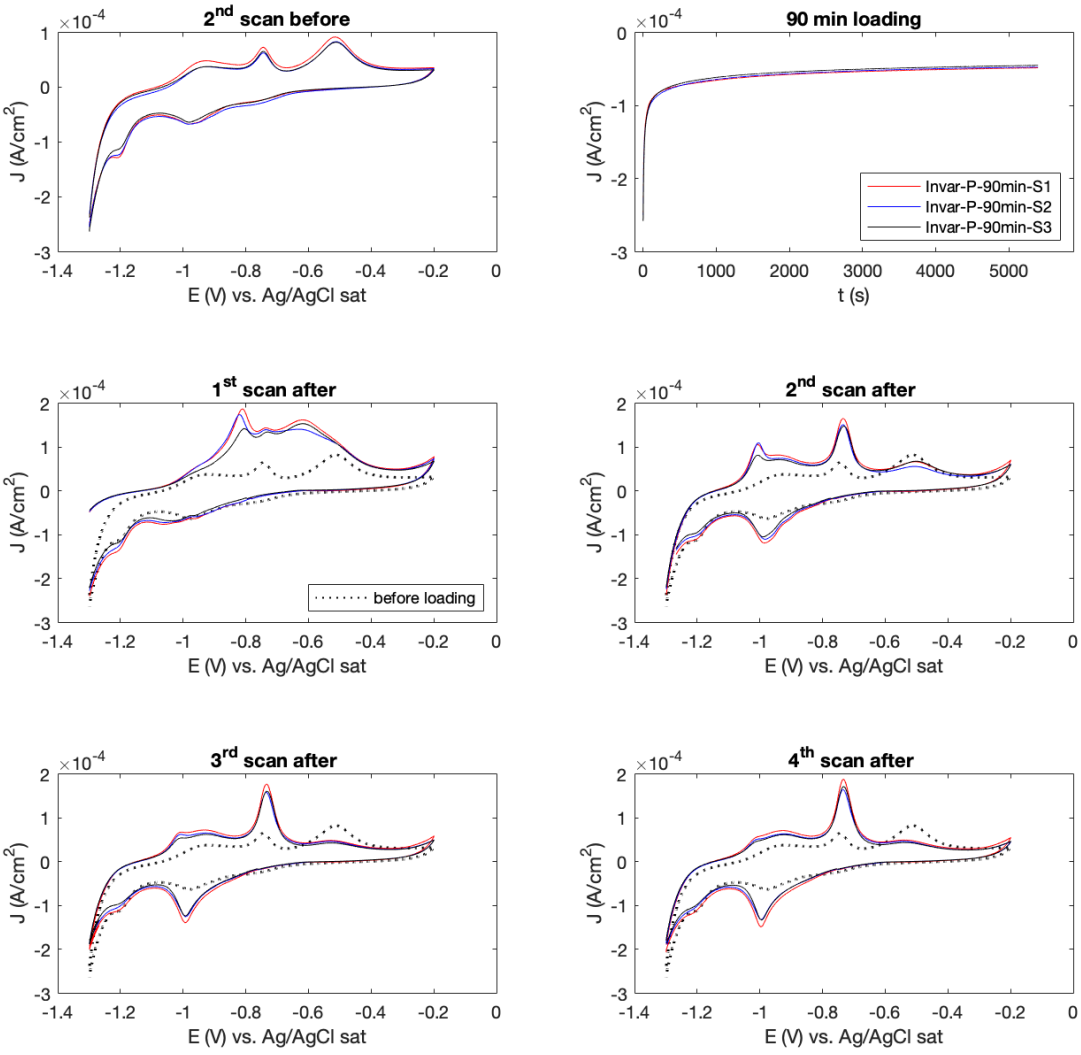

Figure A.10: CV scans corresponding to the replicas of polished Invar before and after 90 min of H_2 loading

A.3.4. 2 h of H_2 loading

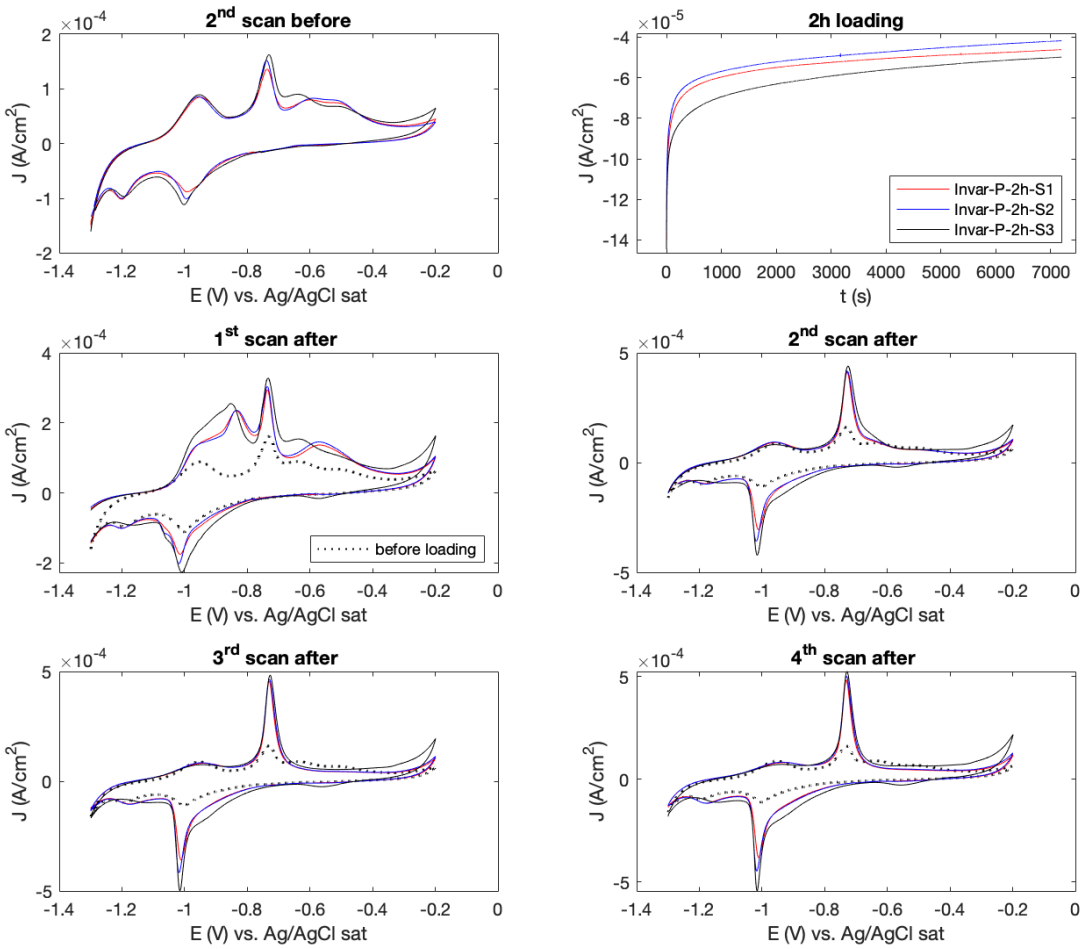

Figure A.11: CV scans corresponding to the replicas of polished Invar before and after 2 h of H_2 loading

A.3.5. 12 h of H_2 loading

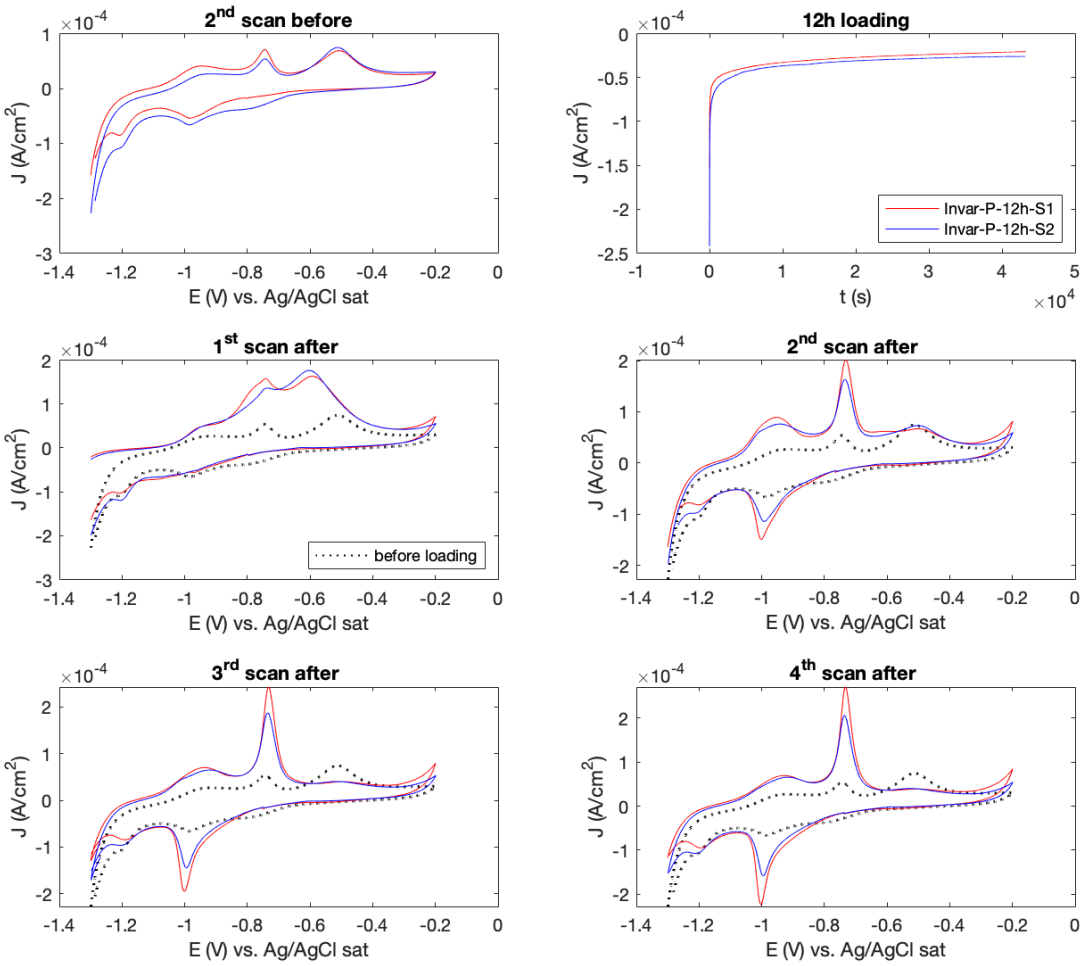

Figure A.12: CV scans corresponding to the replicas of polished Invar before and after 12 h of H_2 loading

B

XRD Results

B.0.1. Invar XRD patterns after H_2 exposure

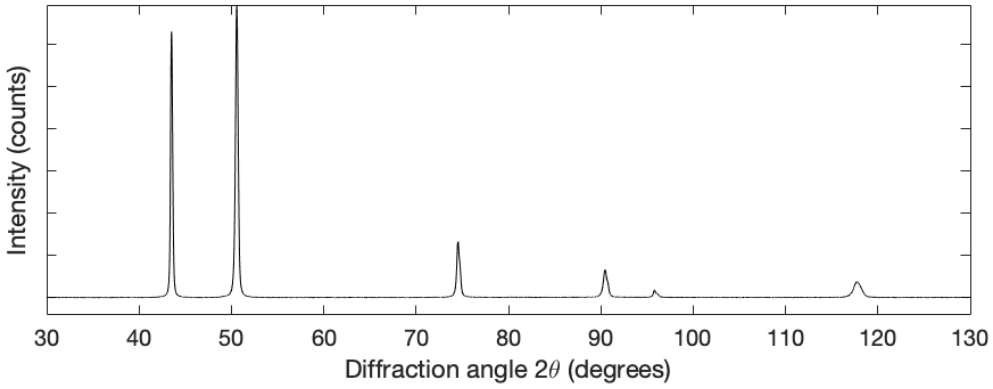

Figure B.1: XRD pattern of polished Invar after sorption for 90 min of H_2 loading

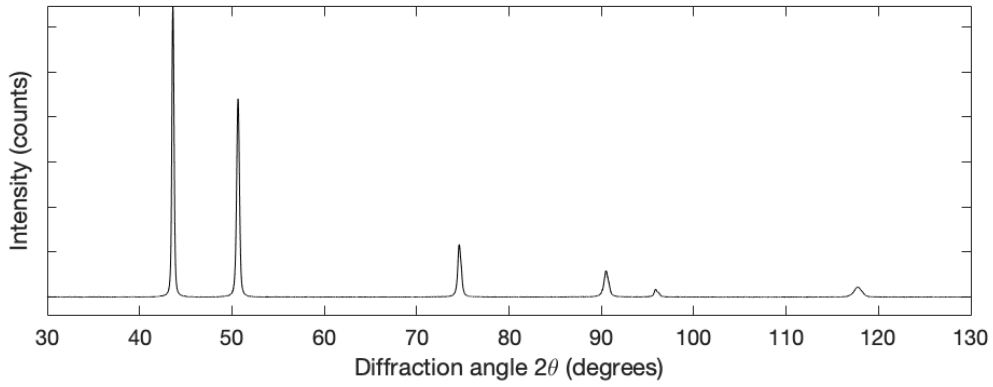

Figure B.2: XRD pattern of polished Invar after desorption for 90 min of H_2 loading

C

Permeability Results

An explorative test of permeability was conducted on uncoated 304L and Invar to obtain preliminary results about the permeation[1] .

The experimental set-up consisted of two chambers, one is the H-loading chamber (entry side), and the other is the H-oxidation chamber (exit side) [16]. At the exit side, a thin protective coating (20 nm) was added by sputtering Pd to avoid oxidation of the iron (steel). The H-permeation is detected by the number of electrons (current density) involved in the oxidation.

In addition, based on the experience on other steels, the expected hydrogen permeation was small (less than 10 μA). Therefore, the thickness of the samples was reduced up to 0.33 mm to reduce the time that hydrogen might take to reach the other side.

C.0.1. Bare 304L

The bare 304L showed a small permeation of 250 nA/cm^2 for the first 4 h, reduced to about 150 nA/cm^2 in the remaining 6 h. The charging current was ON between 500 s and 35500 s. The background current was approximately 10 nA (±20nA).

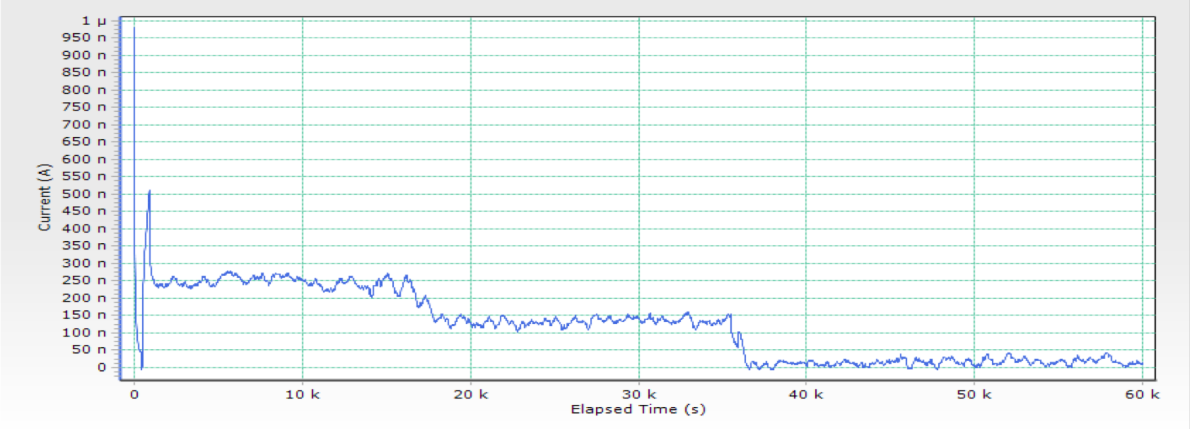

Figure C.1: Response of 304L without TiO_2 layer at the exit side of the permeability chamber

C.0.2. Invar

Figure C.2 shows the response of the Invar sample at the exit side of the permeability chamber. A small permeation of 100 nA/cm^2 constant throughout the experiment was detected. Also, in this case,

[1] PhD Candidate Davide Ripepi from the Material for Energy Conversion and Storage (MECS) research group, Faculty of Applied Science - Chemical Engineering of Delft University of Technology is acknowledged for the permeability experiments (D.Ripepi@tudelft.nl)

the charging current was ON between 500 s and 35500 s.

In the case of Invar, the background current was higher than for the bare 304L stainless steel and equal to 200nA/cm^2 (±30 nA). Invar also showed higher initial passivation current, which is the reason for the higher current level (about 400 nA/cm^2) just prior the beginning of the electrochemical hydrogen loading. This also explains the slight decrease in permeation current recorded during the first hour.

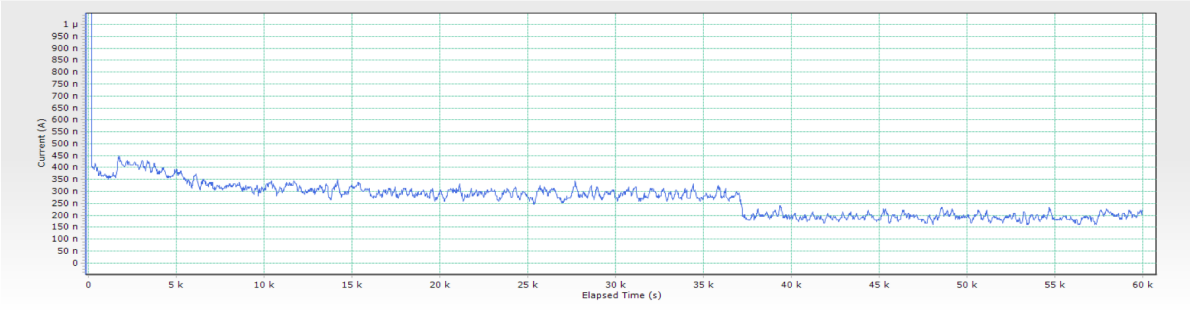

Figure C.2: Response of Invar at the exit side of the permeability chamber

Bibliography

[1] *Chemisorption and reactions of hydrogen*, book section 3, pages 93–152. Springer, Boston, MA, 2005. ISBN 978-0-387-26111-9. URL https://doi.org/10.1007/0-387-26111-7_3.

[2] *Hydrogen Storage Technology: Materials and Applications*. CRC Press Taylor & Francis Group, 2013.

[3] C. Acar and I. Dincer. *1.13 Hydrogen Energy*, volume 1, pages 568–605. 2018. ISBN 9780128149256. doi: 10.1016/b978-0-12-809597-3.00113-9.

[4] Olivier Aleveque and Eric Levillain. A generalized lateral interactions function to fit voltammetric peaks of self-assembled monolayers. *Electrochemistry Communications*, 67:73–79, 2016. ISSN 13882481. doi: 10.1016/j.elecom.2016.04.003. URL http://dx.doi.org/10.1016/j.elecom.2016.04.003.

[5] Bard Allen and Faulkner Larry. *Electrochemical Methods: Fundamentals and Applications*. John Wiley & Sons, Inc., 2nd edition, 2001. ISBN 0-471-04372-9.

[6] O. Barrera, D. Bombac, Y. Chen, T. D. Daff, E. Galindo-Nava, P. Gong, D. Haley, R. Horton, I. Katzarov, J. R. Kermode, C. Liverani, M. Stopher, and F. Sweeney. Understanding and mitigating hydrogen embrittlement of steels: a review of experimental, modelling and design progress from atomistic to continuum. *J Mater Sci*, 53(9):6251–6290, 2018. ISSN 0022-2461 (Print) 0022-2461 (Linking). doi: 10.1007/s10853-017-1978-5. URL https://www.ncbi.nlm.nih.gov/pubmed/31258179.

[7] H. Barthelemy. Hydrogen storage – industrial prospectives. *International Journal of Hydrogen Energy*, 37(22):17364–17372, 2012. ISSN 03603199. doi: 10.1016/j.ijhydene.2012.04.121.

[8] B. J. Berkowltz, J. J. Burton, C. R. Helms, and R. S. Polizzotti. Hydrogen dissociation poinsons and hydrogen embrittlement. *Scripta Metallurgica*, 10(10):871–873, 1976. URL https://doi.org/10.1016/0036-9748(76)90203-9.

[9] R. Bliesner. *Parahydrogen-Orthohydrogen Conversion for Boil-Off Reduction from Space Stage Fuel Systems*. Thesis, 2013.

[10] M. W. Breiter. *Reaction mechanisms of the H2 oxidation/evolution reaction*. John Wiley & Sons, 2003. ISBN 0-471-49926-9. doi: https://doi.org/10.1002/9780470974001.f204027.

[11] Y. F. Cheng and L. Niu. Mechanism for hydrogen evolution reaction on pipeline steel in near-neutral ph solution. *Electrochemistry Communications*, 9(4):558–562, 2007. ISSN 13882481. doi: 10.1016/j.elecom.2006.10.035. URL https://doi.org/10.1016/j.elecom.2006.10.035.

[12] U.K. Chohan, E. Jimenez-Melero, and S.P.K. Koehler. Magnetocrystalline effects on the subsurface hydrogen diffusion in gamma-fe t (001). *Computational Materials Science*, 153:57–63, 2018. doi: 10.1016/j.commatsci.2018.06.025.

[13] G. Cios, T. Tokarski, A. Zywczak, R. Dziurka, M. Stepien, L Gondek, M. Marciszko, B. Pawlowski, K. Wieczerzak, and P. Bala. The investigation of strain-induced martensite reverse transformation in aisi 304 austenitic stainless steel. *Metallurgical and Materials Transactions A*, 48(10):4999–5008, 2017. ISSN 1073-5623 1543-1940. doi: 10.1007/s11661-017-4228-1.

[14] Christophe Coutanceau, Steve Baranton, and Thomas Audichon. *Hydrogen Production From Water Electrolysis*, book section 3, pages 17–62. 2018. ISBN 9780128112502. doi: 10.1016/b978-0-12-811250-2.00003-0.

[15] E. Dabah, V. Lisitsyn, and D. Eliezer. Performance of hydrogen trapping and phase transformation in hydrogenated duplex stainless steels. *Materials Science and Engineering: A*, 527(18-19):4851–4857, 2010. ISSN 09215093. doi: 10.1016/j.msea.2010.04.016.

[16] M. A. V. Devanathan and Z. Stachurski. The adsorption and diffusion of electrolytic hydrogen in palladium. *Proceedings of the Royal Society of London. Series A, Mathematical and Physical Sciences*, 270(1340):90–102, 1962. doi: 10.1016/j.scriptamat.2012.09.001. URL http://www.jstor.org/stable/2416199.

[17] Noemie Elgrishi, Kelley J. Rountree, Brian D. McCarthy, Eric S. Rountree, Thomas T. Eisenhart, and Jillian L. Dempsey. A practical beginner's guide to cyclic voltammetry. *Journal of Chemical Education*, 95(2):197–206, 2017. ISSN 0021-9584 1938-1328. doi: 10.1021/acs.jchemed.7b00361.

[18] Masato Enomoto, Lin Cheng, Hiroyuki Mizuno, Yoshinori Watanabe, Tomohiko Omura, Junichi Sakai, Kenichi Yokoyama, Hiroshi Suzuki, and Ryuji Okuma. Hydrogen absorption into austenitic stainless steels under high-pressure gaseous hydrogen and cathodic charge in aqueous solution. *Metallurgical and Materials Transactions E*, 1(4):331–340, 2014. ISSN 2196-2936 2196-2944. doi: 10.1007/s40553-014-0034-5.

[19] M.E. Fitzpatrick, A.T. Fry, P. Holdway, F.A. Kandil, J. Shackleton, and L. Suominen. Determination of residual stresses by x-ray diffraction. Report ISSN 1744-3911, National Physical Laboratory, 2005. URL https://pdfs.semanticscholar.org/ecba/ba17e7e95806ab701cefab1fd50781adc2b6.pdf.

[20] L. Freire, M. A. Catarino, M. I. Godinho, M. J. Ferreira, M. G. S. Ferreira, A. M. P. Simoes, and M. F. Montemor. Electrochemical and analytical investigation of passive films formed on stainless steels in alkaline media. *Cement and Concrete Composites*, 34(9):1075–1081, 2012. ISSN 09589465. doi: 10.1016/j.cemconcomp.2012.06.002.

[21] R.P. Gangloff and B. Somerday. *Gaseous hydrogen embrittlement of materials in energy technologies: Mechanisms, modelling and future developments*, volume 2. Woodhead Publishing, 2012.

[22] A. Godula-Jopek, W. Jehle, and J Wellnitz. *Hydrogen Storage Technologies: New Materials, Transport, and Infrastructure*. WILEY-VCH Verlag GmbH and Co. KGaA, Weinheim, Germany, 2012. ISBN 978-3-527-64995-2.

[23] Ming Gong, Di-Yan Wang, Chia-Chun Chen, Bing-Joe Hwang, and Hongjie Dai. A mini review on nickel-based electrocatalysts for alkaline hydrogen evolution reaction. *Nano Research*, 9(1):28–46, 2015. ISSN 1998-0124 1998-0000. doi: 10.1007/s12274-015-0965-x.

[24] R.B. Gupta. *Hydrogen Fuel:Production,Transport and Storage*. CRC Press Taylor & Francis Group, 2009. ISBN 978-1-4200-4575-8.

[25] M. Hoelzel, S. A. Danilkin, H. Ehrenberg, D. M. Toebbens, T. J. Udovic, H. Fuess, and H. Wipf. Effects of high-pressure hydrogen charging on the structure of austenitic stainless steels. *Materials Science and Engineering: A*, 384(1-2):255–261, 2004. ISSN 09215093. doi: 10.1016/j.msea.2004.06.017.

[26] Anubhav Jain, Shyue Ping Ong, Geoffroy Hautier, Wei Chen, William Davidson Richards, Stephen Dacek, Shreyas Cholia, Dan Gunter, David Skinner, Gerbrand Ceder, and Kristin a. Persson. The Materials Project: A materials genome approach to accelerating materials innovation. *APL Materials*, 1(1):011002, 2013. ISSN 2166532X. doi: 10.1063/1.4812323. URL http://link.aip.org/link/AMPADS/v1/i1/p011002/s1&Agg=doi.

[27] Gregory Jerkiewicz and Alireza Zollfaghari. Comparison of hydrogen electroadsoption from the electrolytre with hydrogen adsoption from the gas phase. *The Electrochemical Society*, 143(4):1240–1248, 1996. doi: 10.1149/1.1836623. URL http://jes.ecsdl.org/content/143/4/1240.

[28] J.H. Kim, W.S. Park, M.S. Chun, J.J. Kim, J.H. Bae, M.H. Kim, and J.M. Lee. Effect of pre-straining on low-temperature mechanical behavior of aisi 304l. *Materials Science and Engineering*, 543:50–57, 2012. doi: 10.1016/j.msea.2012.02.044. URL https://doi.org/10.1016/j.msea.2012.02.044.

[29] Matthias Kleespies. Lenr - anomalous heat, 2019. URL https://chavascience.com/en/hydrogen/lenr-anomalous-heat.

[30] Yoshitsugu Kojima, Hiroki Miyaoka, and Takayuki Ichikawa. *Hydrogen Storage Materials*, pages 99–136. 2013. ISBN 9780444538802. doi: 10.1016/b978-0-444-53880-2.00006-5.

[31] Motomichi Koyama, Michael Rohwerder, Cemal Cem Tasan, Asif Bashir, Eiji Akiyama, Kenichi Takai, Dierk Raabe, and Kaneaki Tsuzaki. Recent progress in microstructural hydrogen mapping in steels: quantification, kinetic analysis, and multi-scale characterisation. *Materials Science and Technology*, 33(13):1481–1496, 2017. ISSN 0267-0836 1743-2847. doi: 10.1080/02670836.2017.1299276.

[32] Geert-Jan Kroes, Axel Gross, Evert-Jan Baerends, Matthias Scheffler, and Drew A. McCormack. Quantum theory of dissociative chemisorption on metal surfaces. *Accounts of Chemical Research*, 35(3):193–200, 2012. URL https://doi.org/10.1021/ar010104u.

[33] A. Lasia. *Hydrogen evolution reaction*, volume 2, pages 416–440. John Wiley & Sons, 2003. ISBN 0-471-49926-9. doi: 10.1002/9780470974001.f204033.

[34] J. W. Leachman, R. T. Jacobsen, S. G. Penoncello, and E. W. Lemmon. Fundamental equations of state for parahydrogen, normal hydrogen, and orthohydrogen. *Journal of Physical and Chemical Reference Data*, 38(3):721–748, 2009. ISSN 0047-2689 1529-7845. doi: 10.1063/1.3160306.

[35] Junqiao Lee. *Electrochemical Sensing of Oxygen Gas in Ionic Liquids*. Thesis, 2014. URL https://www.researchgate.net/publication/301647753_Electrochemical_Sensing_of_Oxygen_Gas_in_Ionic_Liquids_on_Screen_Printed_Electrodes.

[36] Katherine J. Lee, Noemie Elgrishi, Banu Kandemir, and Jillian L. Dempsey. Electrochemical and spectroscopic methods for evaluating molecular electrocatalysts. *Nature Reviews Chemistry*, 1 (5), 2017. ISSN 2397-3358. doi: 10.1038/s41570-017-0039.

[37] X. Li, B. Gong, C. Denga, and Y. Lia. Failure mechanism transition of hydrogen embrittlement in aisi 304 k-tig weld metal under tensile loading. *Corrosion Science*, 130:241–251, 2018. doi: 10.1016/j.corsci.2017.10.032. URL https://doi.org/10.1016/j.corsci.2017.10.032.

[38] Dong-zhu Lu and Min-jie Wu. Observation of etch pits in fe-36wt%ni invar alloy. *International Journal of Minerals, Metallurgy, and Materials*, 21(7):682–686, 2014. ISSN 1674-4799 1869-103X. doi: 10.1007/s12613-014-0958-x.

[39] S. P. Lynch. *Hydrogen embrittlement (HE) phenomena and mechanisms*, pages 90–130. 2011. ISBN 9781845696733. doi: 10.1533/9780857093769.1.90.

[40] N. Mahmood, Y. Yao, J. W. Zhang, L. Pan, X. Zhang, and J. J. Zou. Electrocatalysts for hydrogen evolution in alkaline electrolytes: Mechanisms, challenges, and prospective solutions. *Adv Sci (Weinh)*, 5(2):1700464, 2018. ISSN 2198-3844 (Print) 2198-3844 (Linking). doi: 10.1002/advs.201700464. URL https://www.ncbi.nlm.nih.gov/pubmed/29610722.

[41] Sofoklis S. Makridis. *Hydrogen storage and compression*, book section 1. 2016. doi: 10.1049/PBPO101E_ch1.

[42] Kasper T. Moller, Torben R. Jensen, Etsuo Akiba, and Hai-wen Li. Hydrogen - a sustainable energy carrier. *Progress in Natural Science: Materials International*, 27(1):34–40, 2017. ISSN 10020071. doi: 10.1016/j.pnsc.2016.12.014.

[43] Michael J. Morgan, Poh-Sang Lam, and Dean A. Wheeler. *Hydrogen Effects On Strain-Induced Martensite Formation in Type 304L Stainless Steel*, pages 171–178. ASM International, 2008. ISBN 1-61503-003-4.

[44] Berk Ozdirik, Kitty Baert, Tom Depover, Jean Vereecken, Kim Verbeken, Herman Terryn, and Iris De Graeve. Development of an electrochemical procedure for monitoring hydrogen sorption/desorption in steel. *Journal of The Electrochemical Society*, 164(13):C747–C757, 2017. ISSN 0013-4651 1945-7111. doi: 10.1149/2.0521713jes.

[45] N. Padhy, Subhash Kamal, Ramesh Chandra, U. Kamachi Mudali, and Baldev Raj. Corrosion performance of tio2 coated type 304l stainless steel in nitric acid medium. *Surface and Coatings Technology*, 204(16-17):2782–2788, 2010. ISSN 02578972. doi: 10.1016/j.surfcoat.2010.02.047.

[46] W.S. Park, M.S. Chun, M.S. Han, M.H. Kim, and J.M. Lee. Comparative study on mechanical behavior of low temperature application materials for ships and offshore structures: Part i—experimental investigations. *Materials Science and Engineering*, 528(18), 2011. doi: 10.1016/j.msea.2011.04.032. URL https://doi.org/10.1016/j.msea.2011.04.032.

[47] Y.I. Park and J.H. Lee. Buckling strength of gtt no96 lng carrier cargo containment system. *Ocean Engineering*, 154(15):43–58, 2018. doi: 10.1016/j.oceaneng.2018.02.017. URL https://doi.org/10.1016/j.oceaneng.2010.12.013.

[48] Roger Parsons. The kinetics of electrone reactions and the electrode material. *Surface Science*, 2:418–435, 1964.

[49] Kristin A. Persson, Bryn Waldwick, Predrag Lazic, and Gerbrand Ceder. Prediction of solid-aqueous equilibria: Scheme to combine first-principles calculations of solids with experimental aqueous states. *Phys. Rev. B*, 85:235438, 06 2012. doi: 10.1103/PhysRevB.85.235438. URL https://materialsproject.org/#apps/pourbaixdiagram.

[50] Elie Protopopoff and Philippe Marcus. *Surface Effects on Hydrogen Entry into Metals*, book section 2, pages 105–148. CRC Press, third edition, 2012. ISBN 978-1-4200-9462-6. URL https://doi.org/10.1201/b11020.

[51] P. Quaino, F. Juarez, E. Santos, and W. Schmickler. Volcano plots in hydrogen electrocatalysis - uses and abuses. *Beilstein J Nanotechnol*, 5:846–54, 2014. ISSN 2190-4286 (Print) 2190-4286 (Linking). doi: 10.3762/bjnano.5.96. URL https://www.ncbi.nlm.nih.gov/pubmed/24991521.

[52] J. Ren, N.M. Musyoka, H.W. Langmi, M. Mathe, and S. Liao. Current research trends and perspectives on materials-based hydrogen storage solutions: A critical review. *International Journal of Hydrogen Energy*, 42(1):289–311, 2017. ISSN 03603199. doi: 10.1016/j.ijhydene.2016.11.195.

[53] P. Rozenak. Stress induce martensitic transformations in hydrogen embrittlement of austenitic stainless steels. *Metallurgical and Materials Transactions A*, 45(1):162–178, 2013. ISSN 1073-5623 1543-1940. doi: 10.1007/s11661-013-1734-7.

[54] P. Rozenak and R. Bergman. X-ray phase analysis of martensitic transformations in austenitic stainless steels electrochemically charged with hydrogen. *Materials Science and Engineering: A*, 437(2):366–378, 2006. ISSN 09215093. doi: 10.1016/j.msea.2006.07.140.

[55] R. Rusli. Hydrogen absorption induced slow crack growth in austenitic stainless steels for petrochemical pressure vessel industries. *Makara Journal of Technology*, 14(2):111–115, 2010. doi: 10.7454/mst.v14i2.702.

[56] C. San Marchi. *Hydrogen embrittlement of stainless steels and their welds*, pages 592–623. 2012. ISBN 9781845696771. doi: 10.1533/9780857093899.3.592. URL https://doi.org/10.1533/9780857093899.3.592.

[57] Buddha R. Shrestha, Theodoros Baimpos, Sangeetha Raman, and Markus Valtiner. Angstrom-resolved real-time dissection of electrochemically active noble metal interfaces. *ACS Nano*, 8(6):5979–5987, 2014. doi: 10.1021/nn501127n. URL https://doi.org/10.1021/nn501127n.

[58] V. Shyvaniuk, Y. Mineb, and S. Teusa. Phase transformation and grain refinement in hydrogenated metastable austenitic steel. *Scripta Materialia*, 67(12):979–982, 2012. doi: 10.1016/j.scriptamat.2012.09.001. URL https://doi.org/10.1016/j.scriptamat.2012.09.001.

[59] Z. Sidhoum, R. Ferhoum, M. Almansba, R. Bensaada, M. Habak, and M. Aberkane. Experimental and numerical study of the mechanical behavior and kinetics of the martensitic transformation in 304l trip steel applied to folding. *The International Journal of Advanced Manufacturing Technology*, 97(5-8):2757–2765, 2018. doi: 10.1007/s00170-018-2154-z. URL https://doi.org/10.1007/s00170-018-2154-z.

[60] Katharine B. Small, David A. Englehart, and Todd A. Christman. Guide to etching specialty alloys. *ADVANCED MATERIALS & PROCESSES*, 2008.

[61] Timothy J. Smith and Keith J Stevenson. *Reference electrodes*, pages 73–110. 2007. ISBN 9780444519580. doi: 10.1016/B978-044451958-0.50005-7. URL 10.1016/B978-044451958-0.50005-7.

[62] Hans-Henning Strehblow, Vincent Maurice, and Philippe Marcus. *Passivity of Metals*, book section 5, pages 235–326. CRC Press, third edition, 2012. ISBN 978-1-4200-9462-6. doi: 10.1201/b11020-6. URL https://doi.org/10.1201/b11020.

[63] V. S. Sumi, M. Ameen Sha, S. R. Arunima, and S. M. A. Shibli. Development of a novel method of nicop alloy coating for electrocatalytic hydrogen evolution reaction in alkaline media. *Electrochimica Acta*, 303:67–77, 2019. ISSN 00134686. doi: 10.1016/j.electacta.2019.02.063.

[64] Gaztransport & Technigaz. Cutting edge technologies and unparalleled know-how, 2019. URL https://www.gtt.fr/en/technologies-services/our-technologies.

[65] Sergio Trasatti. Work function, electronegativity, and electrochemical behaviour of metals. *Electroanalytical Chemistry and Interfacial Electrochemistry*, 39:163–184, 1972. doi: 10.1016/S0022-0728(72)80485-6.

[66] Quang-Dao Trinh. Cyclic voltammetry: Characteristic points, 2011. URL https://demonstrations.wolfram.com/CyclicVoltammetryCharacteristicPoints/.

[67] A. V. Uluc, J. M. C. Mol, H. Terryn, and A. J. Böttger. Hydrogen sorption and desorption related properties of pd-alloys determined by cyclic voltammetry. *Journal of Electroanalytical Chemistry*, 734:53–60, 2014. ISSN 15726657. doi: 10.1016/j.jelechem.2014.09.021.

[68] G. Valenti. *Hydrogen liquefaction and liquid hydrogen storage*, pages 27–51. 2016. ISBN 9781782423621. doi: 10.1016/b978-1-78242-362-1.00002-x.

[69] I. V. Vernyhora, V. A. Tatarenko, and S. M. Bokoch. Thermodynamics of fcc ni-fe alloys in a static applied magnetic field. *ISRN Thermodynamics*, 2012:1–11, 2012. ISSN 2090-5211. doi: 10.5402/2012/917836. URL http://dx.doi.org/10.5402/2012/917836.

[70] Y. Wang, X. Wu, and W. Wu. Effect of α' martensite content induced by tensile plastic prestrain on hydrogen transport and hydrogen embrittlement of 304l austenitic stainless steel. *Metals*, 8(9), 2018. ISSN 2075-4701. doi: 10.3390/met8090660.

[71] J. Wei, M. Zhou, A. Long, Y. Xue, H. Liao, C. Wei, and Z. J. Xu. Heterostructured electrocatalysts for hydrogen evolution reaction under alkaline conditions. *Nanomicro Lett*, 10(4):75, 2018. ISSN 2150-5551 (Electronic) 2150-5551 (Linking). doi: 10.1007/s40820-018-0229-x. URL https://www.ncbi.nlm.nih.gov/pubmed/30464940.

[72] Mark Wijzenbroek. *Hydrogen dissociation on metal surfaces*. Thesis, 2016. URL http://hdl.handle.net/1887/39935.

[73] Q. Yang and J.L. Luo. Effects of hydrogen and tensile stress on the breakdown of passive films on type 304 stainless steel. *Electrochimica Acta*, 46:851–859, 2001. URL https://doi.org/10.1016/S0013-4686(00)00661-7.

[74] Q. Yang, L.J. Qiao, S. Chiovelli, and J.L. Luo. Critical hydrogen charging conditions for martensite transformation and surface cracking in type 304 stainless steel. *Scripta Materialia*, 40(11):1209–1214, 1999.

[75] Y.Nishino, M.Obata, and S.Asano. Hydrogen-induced phase transformations in fe50ni(50-x)mnx alloys. *Scripta Metallurgica et Materialia*, 24(4):703–708, 1990. URL https://doi.org/10.1016/0956-716X(90)90227-8.

[76] John X. J. Zhang and Kazunori Hoshino. *Electrical transducers: Electrochemical sensors and semiconductor molecular sensors*, pages 181–230. 2019. ISBN 9780128148624. doi: 10.1016/b978-0-12-814862-4.00004-1.

[77] L Zhang, Z. Li, J. Zheng, Y. Zhao, P. Xu, C. Zhou, C. Zhou, and Chen X. Dependence of hydrogen embrittlement on hydrogen in the surface layer in type 304 stainless steel. *International Journal of Hydrogen Energy*, I(7), 2014. doi: 10.1016/j.ijhydene.2014.03.254. URL http://dx.doi.org/10.1016/j.ijhydene.2014.03.254.